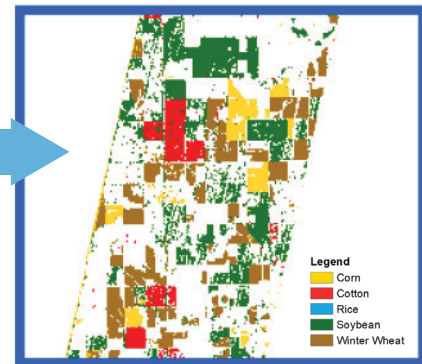
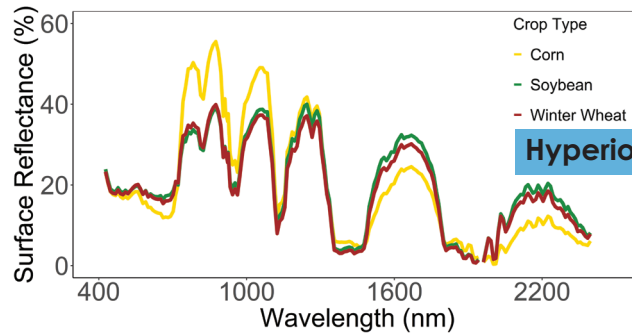
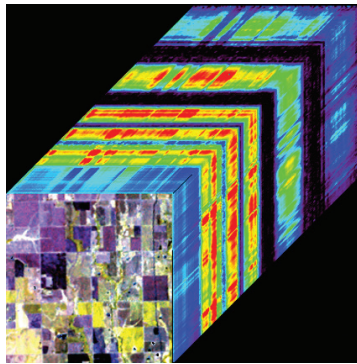
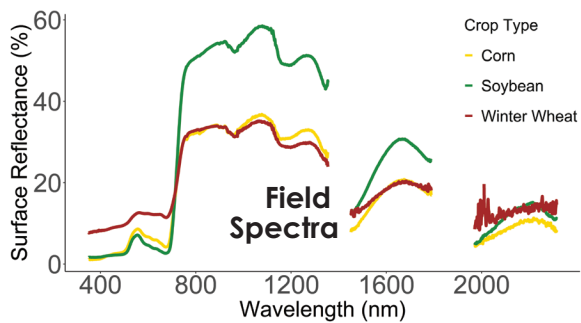


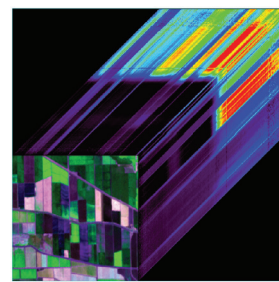
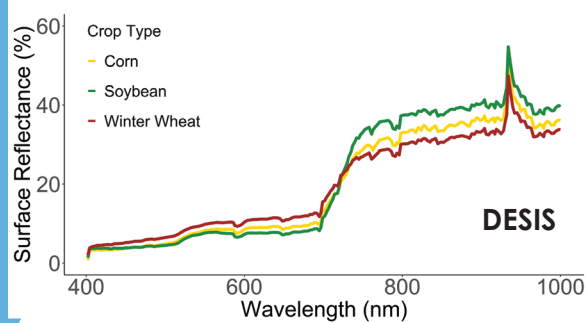
Crop Type Mapping with NASA's EO-1 Hyperion Hyperspectral Data



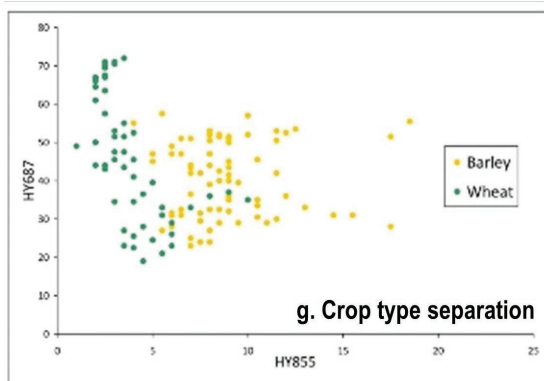
Hyperspectral from Spectroradiometer



Crop Type Mapping with German DLR's DESIS Hyperspectral Data



Training and validation for machine learning classification



NEW
AWARDS UP TO
\$500K



INNOVATE

TRANSFORM OUR FUTURE

R&D FUNDING PROGRAM

The National Reconnaissance Office Director's Innovation Initiative (DII) Program funds cutting-edge scientific research in a high-risk, high-payoff environment to discover innovative concepts and creative ideas that transform overhead intelligence capabilities and systems for future national security intelligence needs. The program seeks the brightest minds and breakthrough technologies from industry, academia, national laboratories, and U.S. government agencies.

Visit the website for Broad Agency Announcement and Government Sources Sought Announcement requirements.

703.808.2769



www.nro.gov/Business-Innovation-Opportunities

ANNOUNCEMENTS

CATALYST, a PCI Geomatics brand, has delivered an automated workflow for the South African National Space Agency's (SANSA) Earth Observation Department to convert decades of SPOT satellite imagery to CARD4L Analysis Ready Data (ARD). The scalable workflow enables SANSA to prepare its entire SPOT archive for immediate analysis using the Open Data Cube, machine learning, and AI models.

CATALYST's ARD workflow automatically converts optical satellite imagery into ARD measurements by performing a series of image preprocessing operations. The output product is a geometrically precise image with \bar{n} surface reflectance measurements based on the rigor and specifications of CARD4L.

SANSA is the government agency responsible for South Africa's space programs and research. The SANSA Earth Observation department collects, processes, archives, and disseminates satellite imagery to support policy and decision making, economic growth, and sustainable development. Imagery in the enormous SANSA SPOT archive is used by multiple government departments for programs related to agriculture, water resource management, and responsible development.

SANSA plans to make their ARD SPOT imagery, which they have been collecting since the early 90s, available to all South African government agencies using the Open Data Cube geospatial data management and analysis platform.

Scientists from various government departments and industries will find that ARD eliminates the significant time and complexities of preparing satellite imagery for analysis, making it more accessible and easier to use. Furthermore, analytical outputs will be more accurate because the ARD process produces geometrically and radiometrically consistent data sets – even if they were collected with different sensors at varying spatial resolutions.

The ARD workflow developed by CATALYST helps to future-proof the investment SANSA has made in acquiring and storing SPOT imagery over the last 30 years. By converting their SPOT archive into CARD4L compliant ARD imagery, SANSA is producing a new commodity that meets the quality and data packaging standards set by the international Committee on Earth Observation Satellites (CEOS). This ensures interoperability among CARD4L image products and a long useful life.

CATALYST is now offering the ARD Workflow within CATALYST Enterprise and CATALYST Microservices for public and commercial satellite optical sensors. The CATALYST Enterprise solution enables users to build scalable production systems for repeatable Earth observation image processing workflows of any size. CATALYST Microservices leverage the infrastructures and business models of public cloud providers to cost effectively process Earth imagery in the cloud at unprecedented scales.

UP42 is proud to announce the UP42 Airbus Challenge in the 2021 Copernicus Masters Competition. With EUR 100,000 in awards at stake, including commercial satellite data from the

Airbus OneAtlas Living Library, UP42 seeks researchers, companies, and students to submit algorithm development ideas to provide new ways of performing EO analytics.

Copernicus Masters is an international competition held annually to foster innovative applications of EO data that address the world's most compelling environmental, social, and business problems. In 2021, UP42 joins other leading geospatial organizations such as the European Space Agency (ESA), European Commission, and German Aerospace Center (DLR) in devising 10 Challenges spanning the full spectrum of EO applications.

"We are excited to be part of a global innovation competition in Earth observation along with other key industry players," said Sean Wiid, CEO at UP42. "This is a unique opportunity for ground-breaking ideas to be brought to life and have a tangible impact on our planet — a goal that perfectly aligns with UP42's core mission."

The UP42 Challenge calls on participants to propose algorithms that advance EO analytics by using Generative Adversarial Networks (GANs) to augment satellite imagery. GANs are an advancement in deep learning technology to generate realistic synthetic data to supplement existing data sets.

The Challenge seeks GAN solutions addressing common EO problems, including:

- Unregistered objects in unsupervised change detection – Use GANs to generate better co-registered images that enable better change detection between images.
- Cloud cover and shadow filling – Leverage GANs to create new pixels that fill in areas of images hidden by clouds or shadows.
- Improved super-resolution – Apply GANs to increase the resolution of Sentinel-2 optical images for enhanced object detection.

The deadline for idea submissions is July 19, 2021. UP42 and Airbus experts will select five finalists to move on to the evaluation and live pitch phase based on scientific merit, business value, quality of implementation, and ecological impact. One Challenge winner will be chosen from the five finalists.

UP42 will announce the winner in October 2021. The winner will receive the following prizes:

- EUR 20,000 voucher to access all geospatial data and algorithms on the UP42 developer platform and marketplace,
- EUR 80,000 voucher for commercial satellite data from the Airbus OneAtlas Living Library,
- Eligibility to win the EUR 10,000 Copernicus Masters Grand Prize.

To learn more about the UP42 Airbus Challenge and to submit your idea, visit <https://copernicus-masters.com/challenges/up42-challenge/>.

VeriDaaS today announced that it has completed test flights necessary to begin its statewide California mapping project by acquiring high-density lidar elevation data on multiple areas of interest (AOIs). This data will be used for evaluation purposes by various state, federal and commercial stakeholders.

In April 2021, VeriDaaS collected data at a minimum of 30 points per meter on a number of AOIs each with different terrain, vegetation and feature densities. These test flights will also be used to baseline sensor collection parameters to ensure the resulting data satisfies a wide range of use cases.

“We are confident that our data will meet and exceed the quality standards required by our targeted stakeholders,” said Christopher Payne, VeriDaaS CEO. “Our recent large area project work in Arizona demonstrated that our Geiger-mode lidar offering exceeds established accuracy specifications at unsurpassed speed and cost-efficiencies,” Payne added. “We look forward to collecting the remainder of California as part of our National Mapping Initiative VeriMAP™.”

The statewide California mapping project will support a wide range of use cases for both government and private enterprises. VeriDaaS continues to build out a coalition of private and public stakeholders to support funding of the project. This coalition will significantly lower the cost for all stakeholders while maximizing the return-on-investment and value of the data.

VeriDaaS is using its Geiger-mode lidar sensor systems and multiple fixed-wing aircraft for this project. The Geiger-mode sensors are optimized for efficient collection of high-density data from higher altitudes while maintaining precision and accuracy over wide geographic areas. The elevation data collected will then be processed and classified to generate derived products and analytical information to support decision-makers across multiple vertical markets. VeriDaaS and its partner network will generate the derived products to meet the specific needs of users in each targeted vertical market.

For more information, visit www.veridaas.com.

TECHNOLOGY

Golden Software, a developer of affordable 2D and 3D scientific modeling packages, has added new and enhanced 3D capabilities to the latest version of its Surfer gridding, contouring, and surface mapping software. New functionality available now, as well as capabilities in Beta development, are focused on making it easier for Surfer users to visualize, display, and analyze complex 3D data.

Surfer enables users to model data sets, apply an array of advanced analytics tools, and graphically communicate the results in ways anyone can understand. The software has been applied for more than 30 years by users in numerous disciplines to easily visualize and interpret complex data sets.

As is the tradition, Golden Software has released a Beta version of Surfer simultaneously with the new version to give customers a chance to try out new features while they are still in development. Users may find the Beta version by clicking File | Online from within Surfer.

For additional information, visit www.GoldenSoftware.com.

Calculating and reporting stockpile inventories are now easier and faster in the latest version of the Virtual Surveyor drone surveying software. Virtual Surveyor Version 8.2 allows users to accurately calculate stockpile volumes in drone imagery

with just a few mouse clicks and then generate a professional PDF report detailing material tonnage and value.

Virtual Surveyor is a powerful surveying software that bridges the gap between drone photogrammetric processing applications and engineering design packages, enabling surveyors to derive topographic information from drone data needed by engineers for construction, mining, and excavation projects. The software presents an interactive onscreen environment with drone orthophotos, digital surface models (DSMs), and/or lidar point clouds where users generate CAD models, create cut-and-fill maps, and calculate volume reports.

Efficient volume calculation has been a Virtual Surveyor feature for several years. To do this, the site operator collects drone imagery and then converts the data into a 3D surface model in the software. The user then simply delineates a pile of sand, gravel, lumber, or other material onscreen with the mouse. The software even allows the user to eliminate equipment from the scene – such as conveyors – to get a precise stockpile calculation.

The user can also set up a Project Template with a Materials Library and layer structure for repeated use. For the Library, the user enters the name of each material – such as Sand, Fine Gravel, Coarse Gravel, etc. – and a density for each. For instance, the typical weight of dry sand is 1.6 tons per cubic meter. Next, the user adds current pricing in euros or dollars for each ton of that material. This value can easily be changed in the Library as commodity prices vary.

As Virtual Surveyor performs stockpile volume calculations, the user simply specifies the material in each pile, and the software determines the weight and value based on the data in the Materials Library.

The new Stockpile Inventory functionality is included in the Virtual Surveyor Ridge and Peak editions. The Peak package gives users the added ability to update inventories for periodic reporting. Current subscribers to Virtual Surveyor will see their software being updated to Version 8.2 automatically. To start a free 14-day trial of Virtual Surveyor and to view details of the three pricing plans, visit www.virtual-surveyor.com.

CALENDAR

- 16-20 August, **URISA GIS Leadership Academy**. For more information, visit www.urisa.org/education-events/urisa-gis-leadership-academy/.
- 3-6 October, GIS-Pro 2021, Baltimore, Maryland. For more information, visit www.urisa.org/gis-pro.
- 8-12 November, **URISA GIS Leadership Academy**, St. Petersburg, Florida. For more information, visit www.urisa.org/education-events/urisa-gis-leadership-academy/.
- 14-18 December, **30th International Cartographic Conference & International Cartographic Exhibition**, Florence, Italy. For more information, visit <https://icaci.org/icc2021>.



461 Hyperspectral Narrowband Data Propel Gigantic Leap in the Earth Remote Sensing

By Prasad S. Thenkabail, Itiya Aneece, Pardhasaradhi Teluguntla, and Adam Oliphant

COLUMNS

- 468 Book Review—*Focus on Geodatabases in ArcGIS Pro*
- 469 GIS Tips & Tricks—Have you ever used the PLSS in your GIS?
- 472 Signatures
The Column of the Student Advisory Council
- 473 Grids and Datums Update
This month we look at the Republic of Bénin

ANNOUNCEMENTS

- 477 Headquarters News
- 478 New ASPRS Members
Join us in welcoming our newest members to ASPRS.
- 512 Call for Submissions—*PE&RS* Special Issue on Remote Sensing Monitoring for Urban Environment

DEPARTMENTS

- 457 Industry News
- 458 Calendar
- 476 Ad Index
- 502 In-Press *PE&RS* Articles
- 525 ASPRS Sustaining Members
- 526 Who's Who in ASPRS
- 527 ASPRS Media Kit

479 Three-Dimensional Reconstruction of Single Input Image Based on Point Cloud

Yu Hou, Ruifeng Zhai, Xueyan Li, Junfeng Song, Xuehan Ma, Shuzhao Hou, and Shuxu Guo

Three-dimensional reconstruction from a single image has excellent future prospects. The use of neural networks for three-dimensional reconstruction has achieved remarkable results. Most of the current point-cloud-based three-dimensional reconstruction networks are trained using nonreal data sets and do not have good generalizability. This article proposes a method for processing real data sets. The data set produced in this work can better train our network model and realize point cloud reconstruction based on a single picture of the real world.

485 A Unified Framework of Bundle Adjustment and Feature Matching for High-Resolution Satellite Images

Xiao Ling, Xu Huang, and Rongjun Qin

Bundle adjustment (BA) is a technique for refining sensor orientations of satellite images, while adjustment accuracy is correlated with feature matching results. Feature matching often contains high uncertainties in weak/repeat textures, while BA results are helpful in reducing these uncertainties. To compute more accurate orientations, this article incorporates BA and feature matching in a unified framework and formulates the union as the optimization of a global energy function so that the solutions of the BA and feature matching are constrained with each other.

491 The Spatiotemporal Evolution of Urban Impervious Surface for Chengdu, China

Mujie Li, Zezhong Zheng, Mingcang Zhu, Yue He, Jun Xia, Xueye Chen, Qingjun Peng, Yong He, Xiang Zhang, and Pengshan Li

The spatiotemporal evolution of an impervious surface (IS) is significant for urban planning. In this article, the IS was extracted and its spatiotemporal evolution for the Chengdu urban area was analyzed based on Landsat imagery.

503 Optimizing the Segmentation of a High-Resolution Image by Using a Local Scale Parameter

Lei Zhang, Hongchao Liu, Xiaosong Li, and Xinyu Qian

Image segmentation is a critical procedure in object-based identification and classification of remote sensing data. However, optimal scale-parameter selection presents a challenge, given the presence of complex landscapes and uncertain feature changes. This article proposes a local optimal segmentation approach that considers both inter-segment heterogeneity and intrasegment homogeneity, uses the standard deviation and local Moran's index to explore each optimal segment across different scale parameters, and combines the optimal segments into a single layer.

513 Review of Spectral Indices for Urban Remote Sensing

Akib Javed, Qimin Cheng, Hao Peng, Orhan Altan, Yan Li, Iffat Ara, Enamul Haq, Yeamin Ali, and Nayyer Saleem

Urban spectral indices have made promising improvements in the last two decades in urban land use land cover studies through mapping, estimation, change detection, time-series analyzing, urban dynamics, monitoring, modeling, and so on. Remote sensing spectral indices are unsupervised, unbiased, rapid, scalable, and quantitative in information extraction. Hence, we aimed to summarize the most relevant urban spectral indices by focusing on multispectral, thermal, and nighttime lights indices.

See the Cover Description on Page 460

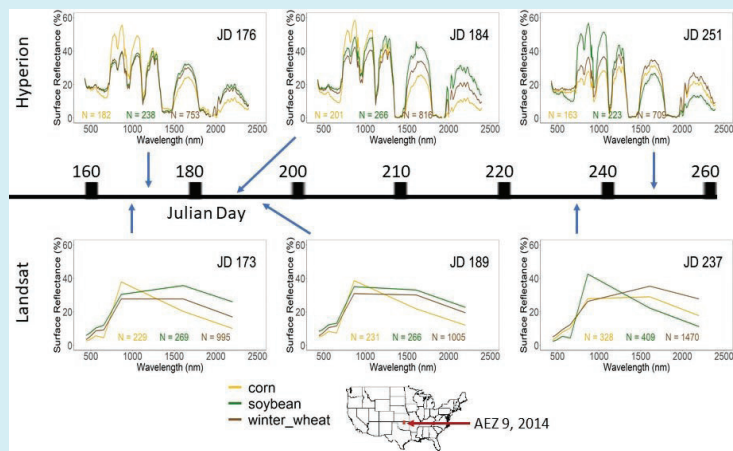
COVER DESCRIPTION

Hyperspectral narrowband (HNB) data or hyperspectral imaging spectroscopy data will play a pivotal role in twenty-first century remote sensing. HNBS provide data as “spectral signatures” in stark contrast to “a few data points along the spectrum” provided by multispectral broadbands (MBBs) as depicted for three leading agricultural crops (corn, soybeans, and winter wheat) of the United States (US). Distribution of agricultural crops in conterminous US (CONUS) is shown in green in the US map as derived from the global croplands work (www.croplands.org; Thenkabail et al., 2021 reference in Highlight article of this issue). HNB “spectral signatures” of the 3 crops are shown using three hyperspectral systems:

- NASA’s Earth Observing (EO-1) Hyperion hyperspectral sensor gathering data from 400 to 2500 nm in 242 bands each 10 nm wide,
- German Deutsches Zentrum für Luft- und Raumfahrt e.V.’s (DLR’s) or The German Aerospace Center’s DESIS (DLR Earth Sensing Imaging Spectrometer) gathering data from 400 to 1000 nm in 235 bands each 2.55 nm wide, and
- Field spectroradiometer gathering data from 400 to 2500 nm in about 1500 bands each 1.43 nm wide.

MBB data are shown using 7 non-thermal bands of Landsat Operational Land Imager (OLI).

The stark contrast of hyperspectral data relative to multispectral data is illustrated below through time-series spectral profiles of three agricultural crops (corn, soybeans, and winter wheat) for the Agroecological Zone 9 for the year 2014. The spectral signatures are for three distinct Julian Days (JD) of JD 176, JD 184, and JD 251 using EO-1 Hyperion data (top images in the Figure below) and for the same or very close corresponding Julian Days of JD 173, JD 189, and JD 237 using multispectral Landsat-8 OLI data (bottom row images in the Figure below). Many subtleties of crop characteristics are averaged in MBB data whereas HNB data capture these variations throughout the electromagnetic spectrum.



There are many major differences in HNB versus MBB data. For example water absorption in 960 or 970 nm is absent in MBBs whereas it is prominent in HNBS. Also, MBBs average spectral data along the spectrum (e.g., 636-673 nm for the red band) whereas HNBS reveal narrow spectral features (e.g. absorption maxima with a 10 nm wide band centered at 680 nm). Numerous absorption features in the 1100 to 2500 nm range are absent in MBBs whereas they are clearly depicted in HNBS. These features help define specific plant characteristics such as:

1. Biophysical quantities (e.g., biomass, leaf area index, plant height);
2. Biochemical quantities (e.g., chlorophyll, nitrogen, pigments: anthocyanin, carotenoids);
3. Plant health quantities (e.g., stress, water deficiency)
4. Plant structural quantities (e.g., erectophile, planophile)

In a new era of remote sensing HNBS allow for gathering spectral libraries of crops that in turn have “signatures” on crop types, their growth stages, and their various quantitative characteristics mentioned above. The spectral libraries can then be fed into machine learning and artificial intelligence models to differentiate, map, and monitor crops, vegetation, and their quantities.

Credits for cover page

Dr. Prasad S. Thenkabail and Dr. Itiya Aneece, Western Geographic Science Center of the United States Geological Survey



PHOTOGRAMMETRIC ENGINEERING & REMOTE SENSING

JOURNAL STAFF

Publisher ASPRS

Editor-In-Chief Alper Yilmaz

Assistant Director — Publications Rae Kelley

Electronic Publications Manager/Graphic

Artist Matthew Austin

Photogrammetric Engineering & Remote Sensing is the official journal of the American Society for Photogrammetry and Remote Sensing. It is devoted to the exchange of ideas and information about the applications of photogrammetry, remote sensing, and geographic information systems. The technical activities of the Society are conducted through the following Technical Divisions: Geographic Information Systems, Photogrammetric Applications, Lidar, Primary Data Acquisition, Professional Practice, and Remote Sensing Applications. Additional information on the functioning of the Technical Divisions and the Society can be found in the Yearbook issue of *PE&RS*.

Correspondence relating to all business and editorial matters pertaining to this and other Society publications should be directed to the American Society for Photogrammetry and Remote Sensing, 425 Barlow Place, Suite 210, Bethesda, Maryland 20814-2144, including inquiries, memberships, subscriptions, changes in address, manuscripts for publication, advertising, back issues, and publications. The telephone number of the Society Headquarters is 301-493-0290; the fax number is 225-408-4422; web address is www.asprs.org.

PE&RS. *PE&RS* (ISSN0099-1112) is published monthly by the American Society for Photogrammetry and Remote Sensing, 425 Barlow Place, Suite 210, Bethesda, Maryland 20814-2144. Periodicals postage paid at Bethesda, Maryland and at additional mailing offices.

SUBSCRIPTION. For the 2021 subscription year, ASPRS is offering two options to our *PE&RS* subscribers — an e-Subscription and the print edition. E-subscribers can plus-up their subscriptions with printed copies for a small additional charge. Print and Electronic subscriptions are on a calendar-year basis that runs from January through December. We recommend that customers who choose both e-Subscription and print (e-Subscription + Print) renew on a calendar-year basis.

The rate of the e-Subscription (digital) Site License Only for USA and Non-USA is \$1000.00 USD. e-Subscription (digital) Site License Only for Canada* is \$1049.00 USD. e-Subscription (digital) Plus Print for USA is \$1365.00 USD. e-Subscription (digital) Plus Print for Canada* is \$1424.00 USD. e-Subscription (digital) Plus Print for Non-USA is \$1395.00 USD. Printed-Subscription Only for USA is \$1065.00 USD. Printed-Subscription Only for Canada* is \$1124.00 USD. Printed-Subscription Only for Non-USA is \$1195.00 USD. *Note: e-Subscription/Printed-Subscription Only/e-Subscription Plus Print for Canada include 5% of the total amount for Canada’s Goods and Services Tax (GST #135123065). **PLEASE NOTE: All Subscription Agencies receive a 20.00 USD discount.**

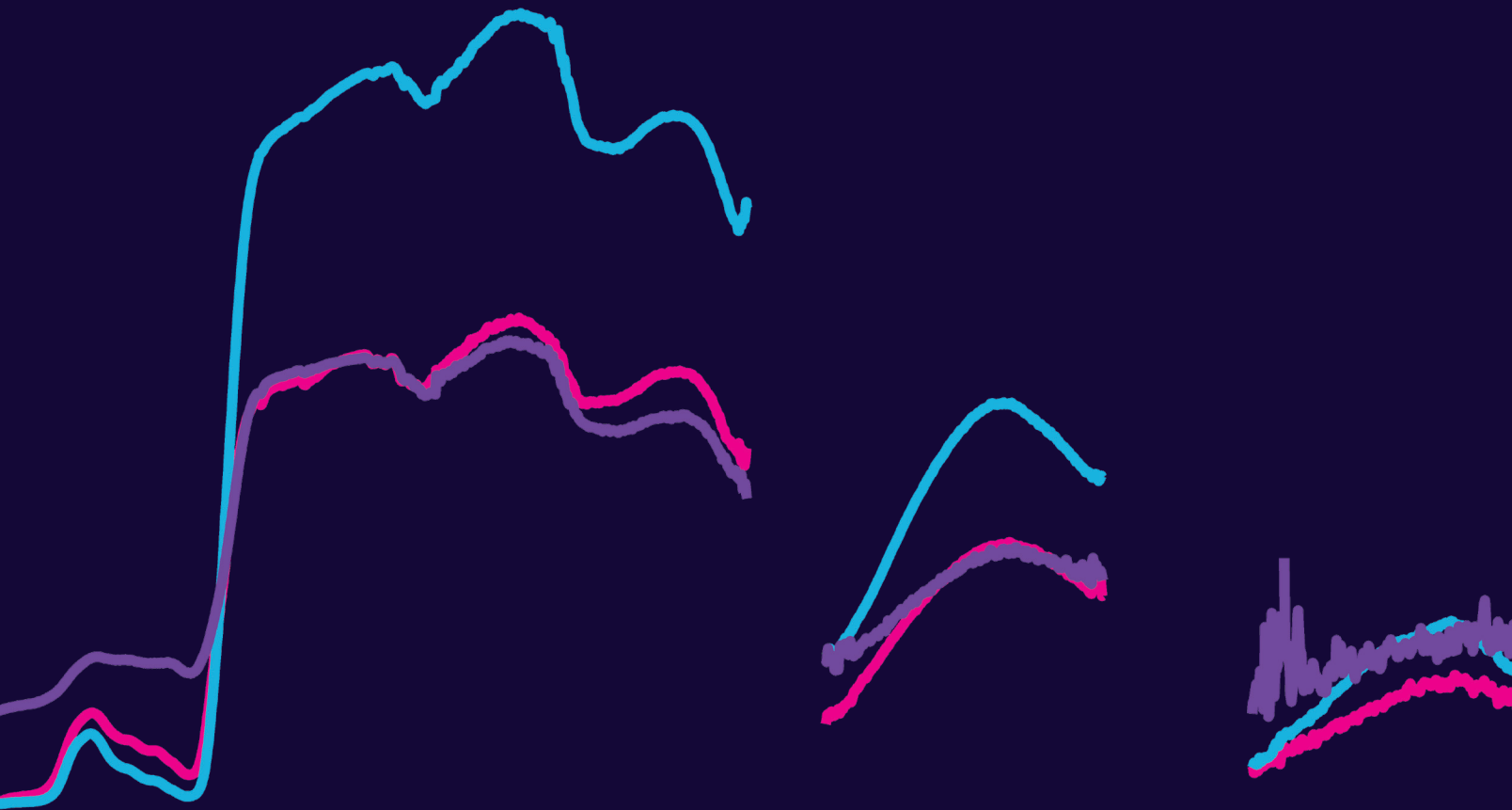
POSTMASTER. Send address changes to *PE&RS*, ASPRS Headquarters, 425 Barlow Place, Suite 210, Bethesda, Maryland 20814-2144. CDN CPM # (40020812)

MEMBERSHIP. Membership is open to any person actively engaged in the practice of photogrammetry, photointerpretation, remote sensing and geographic information systems; or who by means of education or profession is interested in the application or development of these arts and sciences. Membership is for one year, with renewal based on the anniversary date of the month joined. Membership Dues include a 12-month electronic subscription to *PE&RS*. Or you can receive the print copy of *PE&RS* Journal which is available to all member types for an additional fee of \$60.00 USD for shipping USA, \$65.00 USD for Canada, or \$75.00 USD for international shipping. Dues for ASPRS Members outside of the U.S. will now be the same as for members residing in the U.S. Annual dues for Regular members (Active Member) is \$150.00 USD; for Student members \$50.00 USD for USA and Canada \$53.00 USD; \$60.00 USD for Other Foreign members. A tax of 5% for Canada’s Goods and Service Tax (GST #135123065) is applied to all members residing in Canada.

COPYRIGHT 2021. Copyright by the American Society for Photogrammetry and Remote Sensing. Reproduction of this issue or any part thereof (except short quotations for use in preparing technical and scientific papers) may be made only after obtaining the specific approval of the Managing Editor. The Society is not responsible for any statements made or opinions expressed in technical papers, advertisements, or other portions of this publication. Printed in the United States of America.

Hyperspectral Narrowband Data Propel Gigantic Leap in the Earth Remote Sensing

Prasad S. Thenkabail, Iliya Aneece, Pardhasaradhi Teluguntla, and Adam Oliphant
Western Geographic Science Center, United States Geological Survey (USGS)



Photogrammetric Engineering & Remote Sensing
Vol. 87, No. 7, July 2021, pp. 461–467.
0099-1112/21/461–467

© 2021 American Society for Photogrammetry
and Remote Sensing

doi: 10.14358/PERS.87.7.461

Hyperspectral narrowbands (HNBs) capture data as nearly continuous “spectral signatures” rather than a “few spectral data points” along the electromagnetic spectrum as with multispectral broadbands (MBBs). Almost all of satellite remote sensing of the Earth in the twentieth century was conducted using MBB data from sensors such as the Landsat-series, Advanced Very High-Resolution Radiometer (AVHRR), SPOT (Système Pour l’Observation de la Terre), and the Indian Remote Sensing (IRS) satellites. These systems typically provide 4 to 9 broad spectral wavebands spread from 400 to 2500 nm, often with one or two additional bands in the thermal range. Significant advances in the study of the Earth have been made based on these data [Thenkabail et al., 2018a,b,c,d; Thenkabail et al., 2015a,b,c]. Possibilities of great advances that can be made using HNB data over MBB data are well established based on studies conducted using hyperspectral sensors such as the hand-held spectroradiometers, the Airborne Visible/Infrared Imaging Spectrometer (AVIRIS), and spaceborne Earth Observing -1 (EO-1) Hyperion [Thenkabail 2018a,b,c,d]. The twenty-first century is already seeing

the dawn of hyperspectral imaging data from sensors such as the German Aerospace Center’s (DLR’s) DESIS (DLR Earth Sensing Imaging Spectrometer) onboard the MUSES (Multi-User System for Earth Sensing) platform on the International Space Station (ISS), the polar-orbiting Italian Space Agency’s (ASI) PRISMA (PREcursore IperSpettrale della Missione Applicativa), and many other upcoming sensors such as the NASA Surface Biology and Geology (SBG) [Thenkabail et al., 2018a,b,c,d]. These satellites acquire data in hundreds of narrow spectral bands of 1 to 10 nm width, typically between 400 to 2500 nm; also future planned missions will be extending HNBs to the thermal (9,000 to 14,000 nm) electromagnetic spectrum. This expansion creates a quantum leap in new data, new information, and myriad possible new applications in the study of the Earth in addition to great advances in existing applications.

Given the above, the objective of this article is to provide insights on the gigantic leap in our understanding, modeling, mapping, and monitoring of the Earth that can be made using HNB relative to MBB by focusing on agricultural and vegetation applications. We will address this in four aspects:

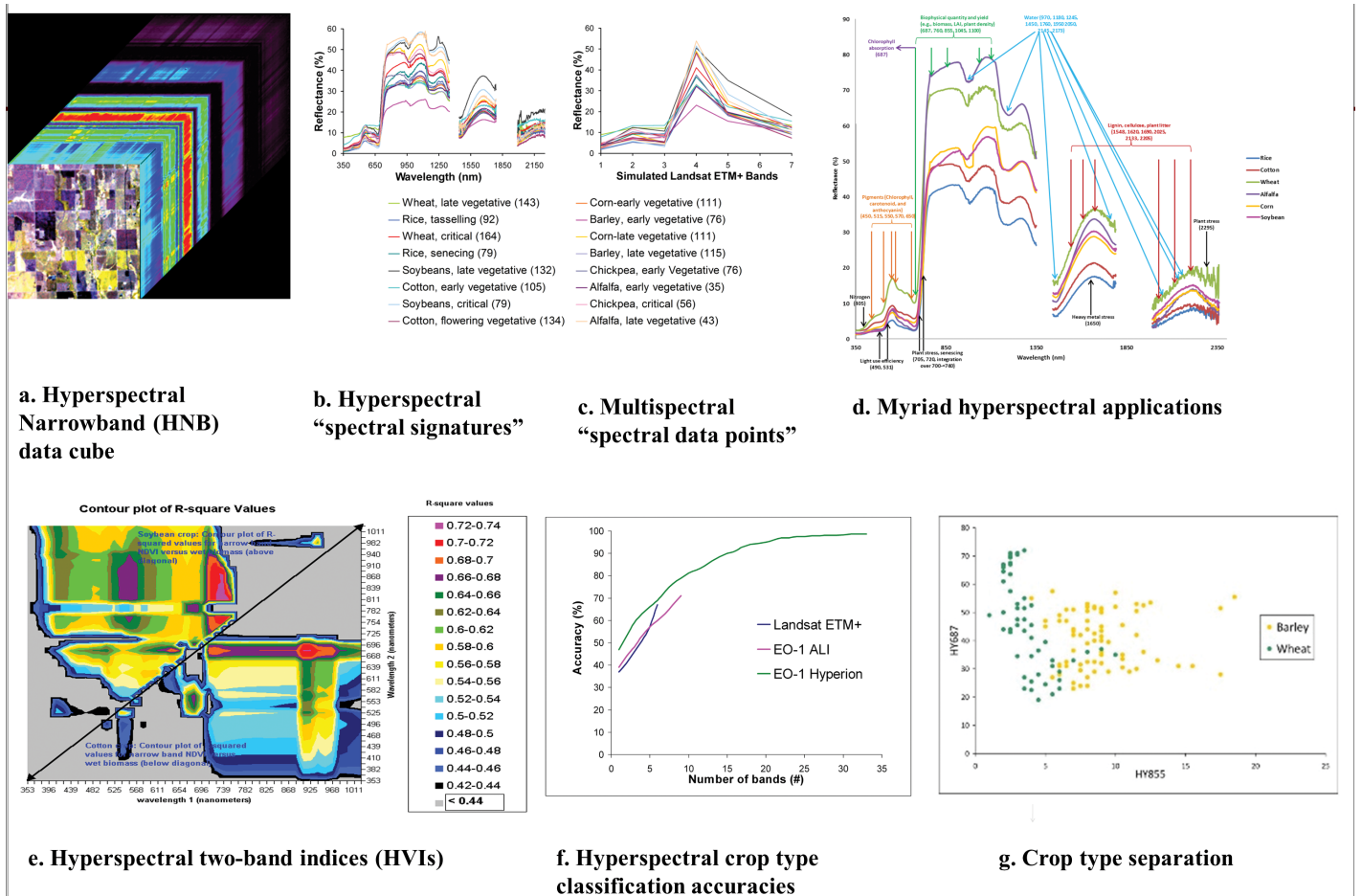


Figure 1. Hyperspectral narrowband (HNB) data advances. This figure shows many advances of hyperspectral data. Hyperspectral data come in 100s of narrowbands as seen in the data cube (Fig. 1a). It is possible to extract, for example, agricultural crops’ spectral signatures using HNBS (Fig. 1b) as opposed to a few data points along the spectrum as in multispectral broadbands (MBBs; Fig. 1c). A multitude of applications are possible using HNBS as illustrated in Fig. 1d. HNBS are used to compute thousands of two-band hyperspectral vegetation indices (HVIs) (Fig. 1e). The Fig. 1e top diagonal provides soybean biomass models and bottom diagonal provides cotton biomass models. Accuracies in crop type classification can be improved by as much as 30% compared to MBBs (Fig. 1f). HNBS offer greater possibilities of separating crop types by selecting unique wavebands along the spectrum (Fig. 1g). [Figure revised and adopted from several research papers of Thenkabail et al. [Thenkabail et al., 2018a,b,c,d].

1. Comparison between HNB and MBB data;
2. Spectral libraries of agricultural crops;
3. HNB data analysis in general; and
4. HNB analysis using machine learning (ML) and cloud computing.

Hyperspectral Narrowband (HNB) versus Multispectral Broadband (MBB) Data

Over the last 50 years, great advances in Earth observation (EO) and Earth studies were achieved, primarily using MBBs, as documented in the three volume Remote Sensing Handbook [Thenkabail et al., 2015a,b,c]. Nevertheless, HNBs allow for a gigantic leap in information-gathering of the planet Earth [Thenkabail et al., 2018a,b,c,d; Anece and Thenkabail, 2018; Marshall and Thenkabail, 2015; Mariotto et al., 2013; Middleton et al., 2009; Anece and Thenkabail, 2019]. Hyperspectral data come in hundreds or thousands of narrowbands (Figure 1a, 1b), each with 1-10 nm bandwidth, continuously along the spectrum (e.g., 400 to 2500 nm; 8000 to 14500 nm). They offer numerous possibilities for targeted applications such as species composition, vegetation or crop type separation, light-use efficiency estimation, and net primary productivity assessment. The quantum leap with HNB data compared to MBB can be visualized by comparing Figure 1b with 1c. HNBs (Figure 1d) along with HNB-derived two-band and multi-band HVIs (Figure 1e) are used to model, map, and monitor plant biophysical properties (e.g., LAI, biomass, yield, density), biochemical properties (e.g., anthocyanins, carotenoids, chlorophyll), plant health properties (e.g., disease and stress assessments, insect infestation, drought), structural properties (e.g., planophile versus erectophile), nutrient content (e.g., nitrogen), and moisture content (e.g., leaf moisture) studies and so on [Anece and Thenkabail, 2018; Marshall and Thenkabail, 2015; Mariotto et al., 2013; Middleton et al., 2009; Anece and Thenkabail, 2019].

The possibilities and advances are innumerable [Thenkabail et al., 2018a,b,c,d], (Figure 1). For example, using about 20 to 30 HNBs the classification accuracies of many agricultural crops or land cover/land use (LCLU) classes can be increased by about 30% relative to 6 to 11 MBBs of sensors such as Landsat Enhanced Thematic Mapper (ETM+) and Advanced Land Imager (ALI) (Figure 1f). HNBs also offer many distinct possibilities of separating crop types by choosing unique wavebands found in distinct portions of the spectrum (Figure 1g). They help derive thousands of hyperspectral vegetation indices (HVIs) to model vegetation quantities such as its biophysical and biochemical quantities (Figure 1e).

Spectral Libraries: Global Hyperspectral Imaging Spectral-Libraries of Agricultural Crops (GHISA)

Hyperspectral data can advance myriad applications for the Earth if there are adequate high-quality reference training and validation data [Anece and Thenkabail, 2019]. Ideally,

well-organized spectral libraries of features, such as minerals, soils, and vegetation are web-enabled and made available for rapid modeling, mapping, and monitoring a wide array of characteristics. A good example is a test of concept Global Hyperspectral Imaging Spectral-Libraries of Agricultural Crops (GHISA) [Anece and Thenkabail, 2019] developed for each agroecological zones (e.g., AEZs; Fig. 2a; see Thenkabail et al., 2021 for different AEZs) or even sub-AEZs when crop characteristics vary widely even within AEZs. A comprehensive GHISA needs to take into consideration a wide array of crop characteristics such as crop types, crop growth stages, cultivars, biophysical, biochemical, and plant structure and health parameters, management practices (e.g., tillage, drainage), inputs (e.g., nitrogen, fertilizers), and drought conditions. The spectral libraries can be developed using data from any type of satellite sensors such as a hyperspectral sensor (Fig. 2b, top row) or Landsat multispectral ones (Fig. 2b, bottom row). These spectral libraries are then deciphered using qualitative or quantitative spectral matching techniques (SMTs) (Fig. 2c) [Thenkabail et al., 2007]. These libraries [Anece and Thenkabail, 2019] are further

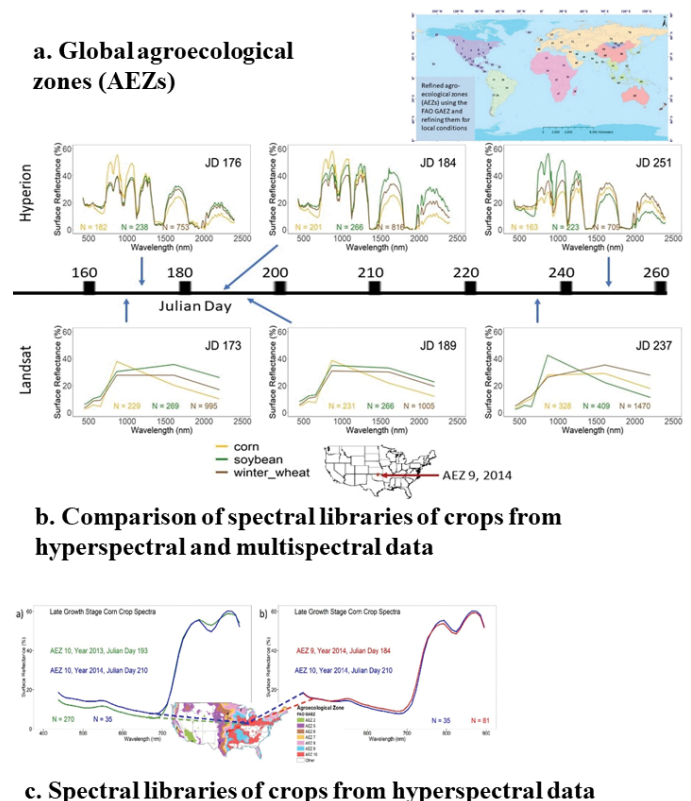


Figure 2. Global hyperspectral Imaging Spectral-libraries of Agricultural Crops (GHISA). The reference training and validation spectral libraries of agricultural crops are developed for each agroecological zone (AEZ) (Fig. 2a; different AEZs are described in [Thenkabail et al., 2014]) based on precise knowledge of the ground data from which spectral libraries are derived using any satellite sensor data. These spectral libraries are illustrated for three crops (corn, soybeans, and winter wheat) for one AEZ in USA using Hyperion hyperspectral data (Fig. 2b top row) and Landsat multispectral data (Fig. 2b bottom row) which can then be used in a wide array of analyses (e.g., spectral matching, Figure 2c).

fed into training and validation machine learning algorithms (MLAs) to model, map, and monitor agricultural features such as cropland extent in global, regional, national, and farm scales [Thenkabail et al., 2021]. Once these libraries are in place, the products can be repeatedly and accurately produced year after year to develop a multitude of agricultural cropland products.

Broad Philosophies of Hyperspectral Data Analysis

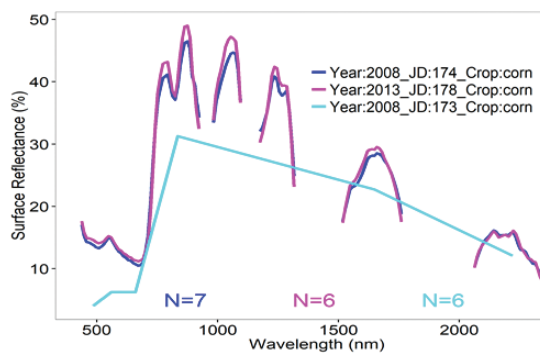
Hyperspectral data bring their own challenges, such as massive data volumes, data redundancy, Hughes phenomenon or curse of data dimensionality, complexities of data analysis, and need for highly trained experts [Thenkabail et al., 2018a,b,c,d]. Further, unlike the MBB data HNB data from different sources still need a mature Application Programming Interface (API). These challenges were largely addressed over the last two decades by an international community of experts and recent advances in machine learning, artificial intelligence, and cloud computing. Overall, there are three broad philosophies regarding hyperspectral data analysis [Thenkabail et al., 2018a,b,c,d] (Figure 3):

- A. Full spectral Analysis (FSA);
- B. Optimal hyperspectral narrowband analysis (OHNBs); and
- C. Transformations and normalizations such as Hyperspectral vegetation indices (HVI)

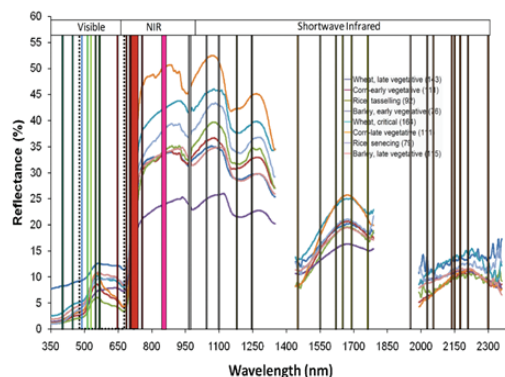
There are many other approaches of hyperspectral data analysis [Thenkabail et al., 2018a,b,c,d; Thenkabail et al., 2015a,b,c], which fall into one or more of the three philosophies listed above.

In the FSA all HNBs, as continuous-spectrum spectral signatures, are used in the analysis (Fig. 3a, 2c). FSA includes methods such as partial least squares regression (PLSR), wavelet analysis, continuum removal, spectral angle mapper (SAM), area under the spectra (integral), artificial neural networks (ANN's), and SMTs (Fig. 3a, 2d) [Thenkabail et al., 2018a,b,c,d; Thenkabail et al., 2015a,b,c; Aneece and Thenkabail, 2018; Marshall and Thenkabail, 2015; Mariotto et al., 2013; Middleton et al., 2009; Aneece and Thenkabail, 2019; Thenkabail et al., 2007].

FSA, for example, would involve creating an ideal spectral databank/libraries [Aneece and Thenkabail, 2019; Thenkabail et al., 2007; Thenkabail et al., 2021] of individual agricultural crops in each AEZ or sub-AEZ throughout the growing season with clear understanding and characterization of crop variables such as crop types, cultivar types, crop growth stages, crop growing conditions (e.g., irrigated or rainfed), and their biophysical, biochemical, structural, and plant health characteristics. A robust databank will involve crops grown during drought, normal, and wet years. Then the HNB data acquired over every growing season and every year will be matched with the ideal spectral databank using various SMT methods to develop models and maps of various



a. Spectral matching



c. Optimal HNBs on spectral profile

b. Optimal HNBs and features

- A. Blue bands (Three columns below: band number, waveband center in nanometer or nm, and application type)
 1. 375 fPAR, leaf water
 2. 466 Chlorophyll
 3. 490 Senescing browning, ripening
- B. Green bands
 4. 515 Nitrogen
 5. 520 Pigment, biomass changes
 6. 525 Vegetation vigor, pigment, nitrogen
 7. 550 Chlorophyll
 8. 575 Vegetation vigor, pigment, and nitrogen
- C. Red bands
 9. 675 Chlorophyll absorption maxima
 10. 682 Biophysical quantities and yield
- D. Red-edge bands
 11. 700 Stress and chlorophyll
 12. 720 Stress and chlorophyll
 13. 740 Nitrogen accumulation
- E. Near-infrared (NIR) bands
 14. 845 Biophysical quantities and yield
 15. 915 Moisture, biomass, and protein
 16. 975 Moisture and biomass
- F. Far NIR (FNIR) bands
 17. 845 Biophysical quantities
 18. 1215 Moisture and biomass
 19. 1245 Water sensitivity
- G. Short-wave infrared (SWIR) band
 20. 1316 Nitrogen
 21. 1445 Vegetation classification and discrimination
 22. 1518 Moisture and biomass
 23. 1725 Lignin, biomass, starch, moisture
 24. 2035 Moisture and biomass
 25. 2173 Protein, nitrogen
 26. 2260 Moisture and biomass
 27. 2295 Stress
 28. 2359 Cellulose, protein, nitrogen

Figure 3. Two of the three broad philosophies in hyperspectral data analysis: Full spectral analysis (FSA) (Figure 3a) through methods like spectral matching techniques (SMTs) (Fig. 3a, also see Fig. 2c); Optimal hyperspectral narrowbands (OHNBs) (Fig. 3b, 3c).

Table 1. Some key two-band hyperspectral vegetation indices (HVIs). The HNB bands in the indices show band centers. The bandwidth is typically 5 nm (optimal) to 10 nm (maximum) for each band except the 531 nm, which has 1 nm bandwidth [Thenkabail 2018a,b,c,d].

Crop Characteristics	Crop Variable	Two-band Hyperspectral Vegetation Index (HVI)
Biophysical quantities	Biomass, LAI, Plant height, Grain yield	$(855 - 682) / (855 + 682)$
Biochemical quantities	Carotenoids, Anthocyanin, Nitrogen, Chlorophyll	$(550 - 515) / (550 + 515)$
Plant health	Stress Conditions	$(855 - 720) / (855 + 720)$
Plant water	Moisture, Water content of plants	$(855 - 970) / (855 + 970)$
Net and gross primary productivity	Light-use efficiency	$(570 - 531) / (570 + 531)$
Biopolymer	Lignin, Cellulose	$(2205 - 2025) / (2205 + 2025)$

features of interest. Rational selection of optimal hyperspectral narrowbands (OHNBs) is an alternative approach to FSA required at times to [Thenkabail et al., 2018a,b,c,d; Thenkabail et al., 2015a,b,c]: A. avoid very large data volumes, B. overcome redundant data, and C. avoid issues of Hughes phenomenon. A third and very common approach that targets the complexity in FSA is the utilization of HVIs. The HVIs target wavelengths/bands which correspond with specific crop variables, referred to as OHNBs, to best quantify, model and map specific species of crops and natural vegetation. Table 1 shows a few selected two-band HVIs. For detailed descriptions of HVIs, one may refer to [Thenkabail et al., 2018a,b,c,d]. While there are some leading OHNBs, HVIs overcome the complexity of hyperplane data to study plant biophysical and biochemical quantities [Cohen and Alchanatis in Thenkabail et al., 2018c]. These approaches pose a different kind of challenge, i.e. investing time and effort in identifying the specific optimal set of bands or VIs for the specific property in a specific zone. Instead, it might be more useful to share the ground truth data collected through global spectral libraries like GHI-SA [Aneece and Thenkabail, 2019] and to use the FSA approach.

Machine Learning for Petabyte Scale Big Data on the Cloud

The massive volumes of hyperspectral data call for new methods and approaches in analyzing them to gather information. This challenge

* Any use of trade, firm, or product names is for descriptive purposes only and does not imply endorsement by the U.S. Government.

requires a gigantic leap or paradigm shift in how hyperspectral data are analyzed involving four steps (Figure 4):

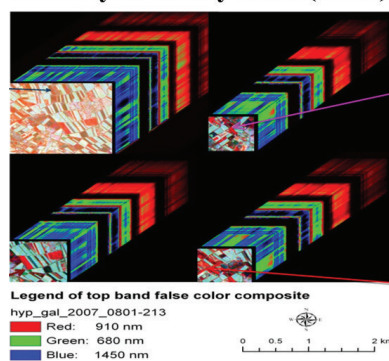
Analysis ready data cubes—The first step is acquiring data from multiple satellites (Fig. 4.1) and creating analysis ready data cubes (Fig. 4.2) that are in at least surface reflectance products that are harmonized and normalized seamlessly over any area of the Earth and stacked as data cubes [Thenkabail et al., 2021]. Already large volumes of Hyperion data are ingested into Google Earth Engine (GEE)* cloud.

Reference data hubs—Reference training and validation data for machine learning [Thenkabail et al., 2021] are acquired either from ground-based surveys or from sub-meter to 5 meters very high-resolution imagery (VHRI), or through national and other reliable sources. These data are properly catalogued and made accessible on the Web for easy access to anyone.

1. Multiple Satellite Image Acquisitions



2. Analysis Ready Data (ARD)



3. Machine Learning Algorithms

Pixel-based supervised MLAs along with Object-based hierarchical segmentation (HSEG)

- A. Random forest algorithms
- B. Support vector machines
- C. Automated cropland classification algorithms
- D. Spectral matching techniques
- E. Decision Tree algorithms
- F. Linear discriminant analysis
- G. Principal component analysis, change detection analysis
- H. kMeans, Isoclass clustering
- I. Classification and Regression Tree (CART)
- J. Tree-based regression algorithm
- K. Phenology based methods
- L. Fourier harmonic analysis
- M. Hierarchical segmentation

4. Automation and Artificial Intelligence

5. Cloud Computing (e.g., Google Earth Engine)

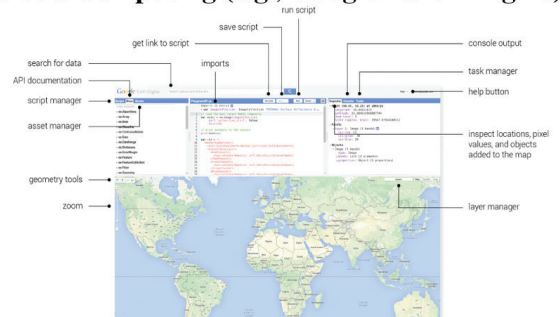


Figure 4. A gigantic leap paradigm shift in analyzing satellite sensor big data on the cloud using machine learning, deep learning, and artificial intelligence. The process is described in detail in [Thenkabail et al., 2021].

Machine learning, deep learning, and Artificial Intelligence (AI)—Selecting machine learning and deep learning algorithms (Fig. 4.3) such as the supervised pixel-based and unsupervised clustering algorithms over multi-dimensional space, object-oriented classifiers, and neural networks is the next step [Thenkabail et al., 2021]. AI is powered by neural networks [Paoletti et al., 2015] such as the: 1. Convolution neural networks (CNNs) for image recognition, image labeling by utilizing features extracted from data rather than reference independent sources, 2. Recurrent neural networks (RNNs) such as signal processing allowing previous outputs to be used as input and thus handling temporal data dependencies better than CNNs, 3. Multi-layer perceptron involving reference sample selection, training the model and classification of images, and 4. Transformers building relationships between pixels and images.

Cloud computing—The above process can be automated by training algorithms on cloud computing platforms such as Google Earth Engine (GEE) [Thenkabail et al., 2021], Amazon Web Services (AWS), Microsoft Azure, or other local and institutional clouds.

A detailed paradigm-shift approach to satellite sensor data based big data analytics is demonstrated by [Thenkabail et al., 2021] in global cropland extent mapping using Landsat, Sentinel, and other data. The same approach can be adopted here for hyperspectral data. However, the key to success in modeling, mapping, and monitoring with machine learning and artificial intelligence techniques with expert knowledge using hyperspectral data will be the generation of rich and systematic spectral libraries of agricultural crops as discussed in Section 2.0 above. There will be a need to define a standardization and to develop a simple protocol for end-users around the globe to share their reference training and validation data that will be further used by the ML/AI methods.

Summary

Hyperspectral imaging spectroscopy or hyperspectral remote sensing will play a significant role in the twenty-first century remote sensing science. The new technology offers many advances by providing “spectral signatures” as opposed to a “few data points along the spectrum”. First, this paper highlights the major advances offered by hyperspectral narrowband data. Second, the importance of building a powerful Global Hyperspectral Imaging Spectral-Libraries of Agricultural Crops (GHISA) to enable highly accurate models, maps, and monitoring tools of a wide array of biophysical, biochemical, plant health and plant structure parameters was discussed. Third, the three major philosophies of hyperspectral data analysis were described and established as full spectral analysis (FSA), optimal hyperspectral narrowbands (OHNBs) and use of transformations or normalizations such as hyperspectral vegetation indices (HVIs). FSA is preferred; however, both OHNBs and HVIs have their own utility and

value in a multitude of applications. For example, strengths of OHNBs and HVIs when avoiding data redundancy, storage issues, and in overcoming Hughes phenomenon (or “curse of high dimensionality of data”). Fourth, the requirement of a machine learning, deep learning, and artificial intelligence (ML/DL/AI) methods on the cloud-platform to best utilize the full power of petabyte-scale hyperspectral big data to propel a quantum-leap in myriad science applications was proposed and discussed. In all this, easily accessible web-enabled analysis ready hyperspectral data through cloud-enabled processing and APIs is a must.

References

- Thenkabail, P.S., Lyon, G.J., and Huete, A. 2018a. *Fundamentals, Sensor Systems, Spectral Libraries, and Data Mining for Vegetation*. CRC Press Boca Raton, Florida. 449 p.
- Thenkabail, P.S., Lyon, G.J., and Huete, A. 2018b. *Hyperspectral Indices and Image Classifications for Agriculture and Vegetation*. CRC Press Boca Raton, Florida. 296 p.
- Thenkabail, P.S., Lyon, G.J., and Huete, A. 2018c. *Biophysical and Biochemical Characterization and Plant Species Studies*. CRC Press Boca Raton, Florida. 348 p.
- Thenkabail, P.S., Lyon, G.J., and Huete, A. 2018d. *Advanced Applications in Remote Sensing of Agricultural Crops and Natural Vegetation*. CRC Press Boca Raton, Florida. 386 p.
- Thenkabail, P.S. 2015a. *Remotely Sensed Data Characterization, Classification, and Accuracies*. CRC Press Boca Raton, Florida. 678 p.
- Thenkabail, P.S. 2015b. *Land Resources Monitoring, Modeling, and Mapping with Remote Sensing*. CRC Press Boca Raton, Florida. 849 p.
- Thenkabail, P.S. 2015c. *Remote Sensing of Water Resources, Disasters, and Urban Studies*. CRC Press Boca Raton, Florida. 673 p.
- Aneece, I. and P. Thenkabail. 2018. Accuracies Achieved in Classifying Five Leading World Crop Types and their Growth Stages Using Optimal Earth Observing-1 Hyperion Hyperspectral Narrowbands on Google Earth Engine. *Remote Sensing*. 2018, 10, 2027. <https://doi.org/10.3390/rs10122027> IP-097093.
- Marshall M. T. and P. Thenkabail. 2015. Developing in situ Non-Destructive Estimates of Crop Biomass to Address Issues of Scale in Remote Sensing. *Remote Sensing*. 2015; 7(1):808-835. doi:10.3390/rs70100808. IP-060652.
- Mariotto, I., Thenkabail, P.S., Huete, H., Slonecker, T., Platonov, A., 2013. Hyperspectral versus Multispectral Crop- Biophysical Modeling and Type Discrimination for the HypIRI Mission. *Remote Sensing of Environment*. 139:291-305. IP-049224.

Middleton, E.M., Cheng, Y.B., Hilker, T., Black, T.A., Krishnan, P., Coops, N.C., & Huemmrich, K.F. 2009. Linking foliage spectral responses to canopy-level ecosystem photosynthetic light-use efficiency at a Douglas-fir forest in Canada. *Canadian Journal of Remote Sensing*, 35(2), 166-188.

Aneece, I. and P. Thenkabail. 2019. Global Hyperspectral Imaging Spectral-library of Agricultural crops (GHISA) for the Conterminous United States (CONUS). Algorithm Theoretical Basis Document (ATBD). NASA Land Processes Distributed Active Archive Center (LP DAAC). IP-110217.

<https://lpdaac.usgs.gov/news/release-global-hyperspectral-imaging-spectral-library-agricultural-crops-conterminous-united-states/>

<https://lpdaac.usgs.gov/products/ghisaconusv001/>

Thenkabail, P.S., GangadharaRao, P., Biggs, T., Krishna, M., and Turrall, H., 2007. Spectral Matching Techniques to Determine Historical Land use/Land cover (LULC) and Irrigated Areas using Time-series AVHRR Pathfinder Datasets in the Krishna River Basin, India. *Photogrammetric Engineering and Remote Sensing*. 73(9): 1029-1040.

Thenkabail, P.S., Teluguntla, P., Xiong, J., Oliphant, A., Congalton, R., Ozdogan, M., Gumma, M.K., Tilton, J., Giri, C., Milesi, C., Phalke, A., Massey, M., Yadav, K., Mile-si, C., Sankey, T., Zhong, Y., Aneece, Y., Foley, D. 2021. Global Cropland Extent Product at 30m (GCEP30) derived using Landsat Satellite Time-series Data for the Year 2015 through Multiple Machine Learning Algorithms on Google Earth Engine (GEE) Cloud. Research Paper #, United States Geological Survey (USGS). In press. IP-119164.

Paoletti, M.E., Haut, J.M., Plaza, J., and Plaza, A. 2019. Deep learning classifiers for hyperspectral imaging: A review Author links open overlay panel. *ISPRS Journal of Photogrammetry and Remote Sensing*. 158: 279-317.

Acknowledgements

Authors would like to thank Dr. Terrence Slonecker, Research Geographer at United States Geological Survey (USGS) and Dr. Yafit Cohen, Professor at the Institute of Agricultural Engineering, Agricultural Research Organization (A.R.O), Volcani Center, Israel for their insights in reviewing the manuscript. We also thank Prof. Jie Shan, Assistant Editor of *PE&RS* and Professor of Civil Engineering at the Purdue University for his valuable insights and edits. Also, very grateful for Dr. Lucia Lovison, Co-Editor of *PE&RS* for encouraging us to write this article after hearing Dr. Thenkabail give keynote talk at the spectral Sessions Conference. We are grateful for the funding provided by The National Land Imaging (NLI) Program, Land Change Science (LCS) program, and the Core Science Systems (CSS) of the USGS. The research is conducted in the science facilities of the Western Geographic Science Center (WGSC) of USGS.

About the Authors

Dr. Prasad S. Thenkabail is a Supervisory Research Geographer with the United States Geological Survey (USGS) based in Flagstaff, Arizona, USA and is among the top most impactful 1% of the world scientists across all fields as per a recent Stanford University publication.

Dr. Itiya Aneece is a Research Geographer with the United States Geological Survey (USGS) in Flagstaff, Arizona, USA, focusing on using hyperspectral data and machine learning on the Cloud to study agricultural crops.

Dr. Pardhasaradhi Teluguntla is a Senior Research Scientist with the Bay Area Environmental Research Institute (BAERI), working at the USGS center in Flagstaff, Arizona, USA. He is a lead contributor to global cropland mapping and irrigation mapping using machine learning on the Cloud.

Mr. Adam Oliphant is a Geographer with the United States Geological Survey (USGS) in Flagstaff, Arizona, USA, focusing on using multispectral data and machine learning on the Cloud to study agricultural crops.

ASPRS WORKSHOP SERIES



It's not too late to earn Professional Development Hours

Miss an ASPRS Workshop or GeoByte? Don't worry! Many ASPRS events are available through our online learning catalog.

<https://asprs.prolearn.io/catalog>

Image Priscilla Du Preez on Unsplash.

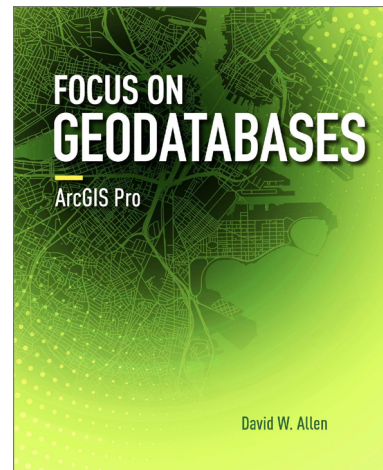
The goal of *Focus on Geodatabases in ArcGIS Pro* is to introduce the geodatabase file format and functionality in Esri's ArcGIS Pro software as tools for designing and managing features in operational spatial data. The book is designed as a manual for the higher education classroom or professional training, but those new to designing spatial databases or making the transition to creating and editing features in ArcGIS Pro will also benefit. *Focus on Geodatabases in ArcGIS Pro* uses realistic data and situations from local government to demonstrate concepts and exemplify the life course of data.

Focus on Geodatabase's seven chapters can be divided into four parts. Chapters one through three, comprise 41% of the book, discuss geodatabase design concepts, creating a geodatabase, and loading existing data into the new geodatabase. Chapter four extends the idea of geodatabases into ArcGIS Online and 3D maps. Chapters five and six, making up 32% of the book, guide users through ArcGIS Pro tools for creating and editing point, line, and polygon features. Chapter seven discusses ArcGIS Pro map topology and geodatabase topology.

Each chapter has a brief introduction, followed by two tutorials that guide the reader through the concepts or tools with realistic data. Each tutorial has a short introduction with learning objectives. More than half of the tutorials include a "your turn" section that allows readers to check their progress against the narrative text. Numerous screenshots help the reader follow along and ensure that those working through the tutorial stay on track. Each tutorial is followed by an exercise that allows the reader to practice the concepts or tools from the tutorial on their own. Each tutorial and exercise section concludes with recommendations for "what to turn in" if used in a classroom setting, a review of the section, study questions, and other topics to look up in the ArcGIS Pro help for further study.

Tutorials and exercises use realistic data for the fictional town of Oleander, Texas. Chapters one through three use examples related to property and wastewater for designing, building, and loading data. Chapters four through seven add examples related to stormwater, structures, surface mapping, and political and service boundaries. Of the seven chapters, all but one use property mapping concepts such as parcels, lot lines, or easements as part of the tutorial or exercise.

By the end of the book, readers will have a firm grasp of geodatabase and ArcGIS Pro functionality, tools, and vocabulary related to configuring geodatabases and creating and editing points, lines, and polygons for data commonly used in local government and services. Readers are also able to follow the life course of a dataset from requirements, design, and construction to daily use and quality control with topology. If users follow along and work through the tutorials and exercises, they will have experience in creating and editing realistic data configured in a geodatabase that encourages data quality and integrity. Chapter four may appear as an outlier in this purpose, but in actuality expands on the life



Focus on Geodatabases in ArcGIS Pro

David W. Allen

Esri Press, Redlands, CA. 2019. viii and 251 pp., images, index, data, software license key. Paperback. \$59.99. ISBN 978-1-58948-445-0.

Reviewed by Matthew J. Gerike, Research Scholar of Interdisciplinary Studies, William & Mary, Williamsburg, Virginia.

course concept by demonstrating how ArcGIS Pro easily publishes local data to ArcGIS Online feature services and maps to share information, increase access, and make operational workflows more efficient. Chapter four may fit better as the concluding chapter, but it serves as a good break between the geodatabase design of the early chapters and the ArcGIS Pro editing of the later chapters.

As a text, *Focus on Geodatabases* is effective in introducing readers to a plan, design, and build a model for creating spatial datasets and demonstrating real-world advantages that well-planned geodatabases have for enforcing data quality concepts and saving time with types of data commonly encountered in local government. Principles such as data design, valid values restrictions, domain pick-lists, and relationships relate to other spatial databases beyond Esri's geodatabase. As a technical manual, *Focus on Geodatabases* is effective in guiding users through specific ArcGIS Pro interfaces, menus, and tools related to creating and editing

continued on page 471

Photogrammetric Engineering & Remote Sensing
Vol. 87, No. 7, July 2021, pp. 468–471.
0099-1112/21/468–471

© 2021 American Society for Photogrammetry
and Remote Sensing

doi: 10.14358/PERS.87.7.468

GIS Tips & Tricks

By Al Karlin, Ph.D. CMS-L, GISP, and Brandon Gravett

Have you ever used the PLSS in your GIS?

If you are unfamiliar with the Public Land Survey System (PLSS) or have never used it in your GIS, here are a few tips and tricks, along with a little history.

The Public Land Survey System (PLSS), sometimes referred to as the “Rectangular Survey System”, or the BLM (Bureau of Land Management) System has been around since the post-Revolutionary War days. Originally created by the Land Ordinance of 1785 to survey the land ceded to the newly founded United States government by the Treaty of Paris in 1783, the system divides land into rectangular,

one-square mile “Sections”, and accumulates those sections into 36-square mile (6 mile x 6 mile) rectangular Townships north or south of a “Base Line”, and Ranges, east or west of a “Principal Meridian”. With some exceptions, most notably, territory under the jurisdiction of the original 13 colonies at the time of independence and select others, the PLSS is the “law of the land” in the United States regarding survey and conveyance of public lands.

The system was constructed based on an “Initial Point” from which a parallel of latitude, a Base Line, and a Principal Meridian, a true meridian running through the Initial Point, were surveyed. From these two lines, the hierarchical system of Townships (north or south of the Base Line) and Ranges (east or west of the Principal Meridian) were constructed. Within each Township/Range, 36 – one square mile sections were surveyed in a 6 x 6 square mile rectangle as shown below in Figure 1. The BLM Map (Figure 2) shows the Principal Meridians and Base Lines for those states surveyed with the PLSS. States not colored are the “exceptions” noted above.

It is important to understand that the PLSS is not a coordinate system. You will not find the PLSS in the Esri Spatial Reference List, the European Petroleum Survey Group (EPSG) Codes, or the Well Known Text (WKT) files. However, almost all historic and current topographic maps from the US Geological Survey (USGS) include PLSS tic marks or grids, and in recent years, surveyors have been recovering the historical PLSS marker-posts and assigning GPS-coordinates, usually in State Plane systems. As an example, the State of Florida maintains a set of PLSS Certified Corner Records (CCRs) referenced to Florida State Plane Coordinates. The state plane coordinates and survey data sheets can be easily retrieved from the Land Boundary Information System at <https://www.LABINS.org>. Many other states are likewise publishing CCRs to their

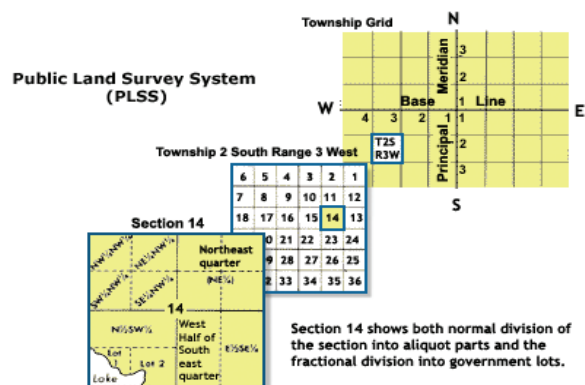


Figure 1. General layout for Sections (square miles), Townships, Ranges, Base Lines and Principal Meridians as described in the Public Land Survey System.

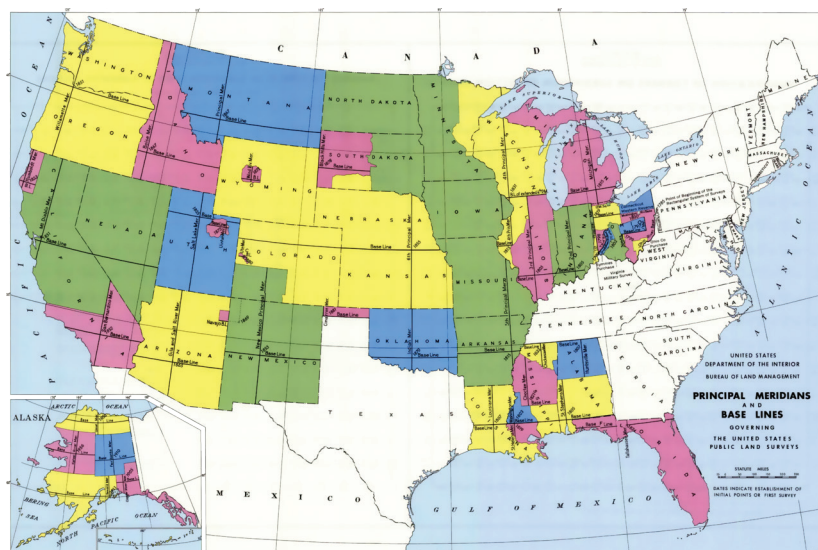


Figure 2. Bureau of Land Management map showing the Principal Meridians and Base Lines used in the Public Land Survey System.

Photogrammetric Engineering & Remote Sensing
Vol. 87, No. 7, July 2021, pp. 469–471.
0099-1112/21/469–471

© 2021 American Society for Photogrammetry and Remote Sensing

doi: 10.14358/PERS.87.7.469

websites, and entire PLSS data layers are available through REST services from the BLM at the following:

https://gis.blm.gov/arcgis/rest/services/Cadastral/BLM_Natl_PLSS_CadNSDI/MapServer

The PLSS also provides a system of subdivisions and number systems. Many large facilities have post office box addresses with no street address, but include a PLSS field for reference. This PLSS field can provide valuable information in verifying that a facility was damaged from the actual path of a storm or other natural disaster through the use of PLSS locator “add-ons”.

The technique described below uses the PLSS “add-ons” or descriptions in order to confirm addresses for large surface features such as quarries or other types of facilities that would be readily identifiable via on-line aerial photography.

FACILITY	PLSS DESCRIPTION	CITY, STATE
Auburndale WWTP	NWQ SEQ SEC 23 T25N R4E	Auburndale, WI US

The above is an example of a facility with only minimal information about its location available. The city (Auburndale) and state (Wisconsin) for the PLSS description is provided along with a, rather cryptic, PLSS Description. A more interpretable, natural-language, description for the highlighted PLSS record is “North-West Quarter of the South East Quarter of Section 23, Township 25 North, Range 4 East”. The diagram, in Figure 2, helps clarify the PLSS description where Township 25N, Range 4E, Section 23 is shown highlighted in the center, with further quarter and 16th subdivisions shown. In this case, they are further subdividing the facility location to the northwest quarter of the southeast quarter.

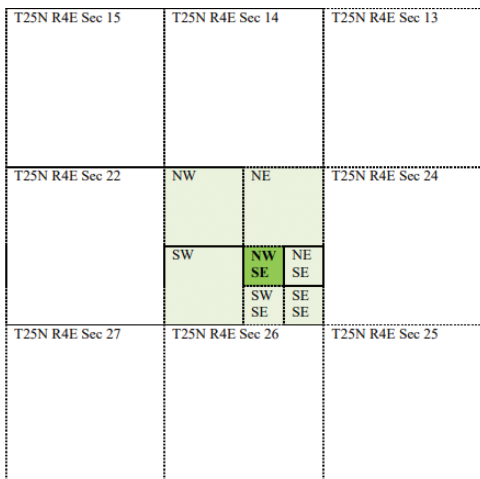


Figure 3. PLSS Grid showing Quarter-Quarter divisions for the Auburndale facility search example.

This PLSS description can be used as location input at websites like Earth Point which can then return real-world coordinates for the corners and centroid of the section:

<http://www.earthpoint.us/TownshipsSearchByDescription.aspx>

Figure 4. EarthPoint website PLSS Entry Form.

Entering the State and associated PLSS Township, Range, and Section data, and pressing the “View” button to confirm the coordinates returns the PLSS/BLM data and geographic coordinates for the Township (left) and the selected section (right) as shown below:

Township - BLM database		Section - BLM database	
Township	T25N R4E	Section	S23 T25N R4E
Meridian	Fourth	Meridian	Fourth
State	Wisconsin	State	Wisconsin
Source	USFS	Source	USFS
GLO	GLO Township Records	GLO	GLO Township Records
Calculated Values		Calculated Values	
Acres	21,985	Acres	637
Centroid	44.6414130, -90.0221990	Centroid	44.6340406, -89.9949882
Corners	NW 44.6851186, -90.0795334 NE 44.6849018, -89.9640453 SE 44.5983119, -89.9645633 SW 44.5972118, -90.0798333	Corners	NW 44.6411619, -90.0050434 NE 44.6413919, -89.9849134 SE 44.6269919, -89.9848034 SW 44.6266818, -90.0051534
For illustration only. User to verify all information. www.earthpoint.us		Quarters This section has 0 quarter/quarters plotted.	
For illustration only. User to verify all information. www.earthpoint.us		For illustration only. User to verify all information. www.earthpoint.us	

Figure 5. Geographic Coordinates for the Township and Section input.

Pressing the “Fly to on Google Earth” button (on Figure 4) will generate a GoogleEarth KML file and open a file browser to save the KML file on your computer. Opening the GoogleEarth KML you can visually confirm proximity to Auburndale, WI and as in many cases, the road grid also follows the PLSS sections and outlines section 23:

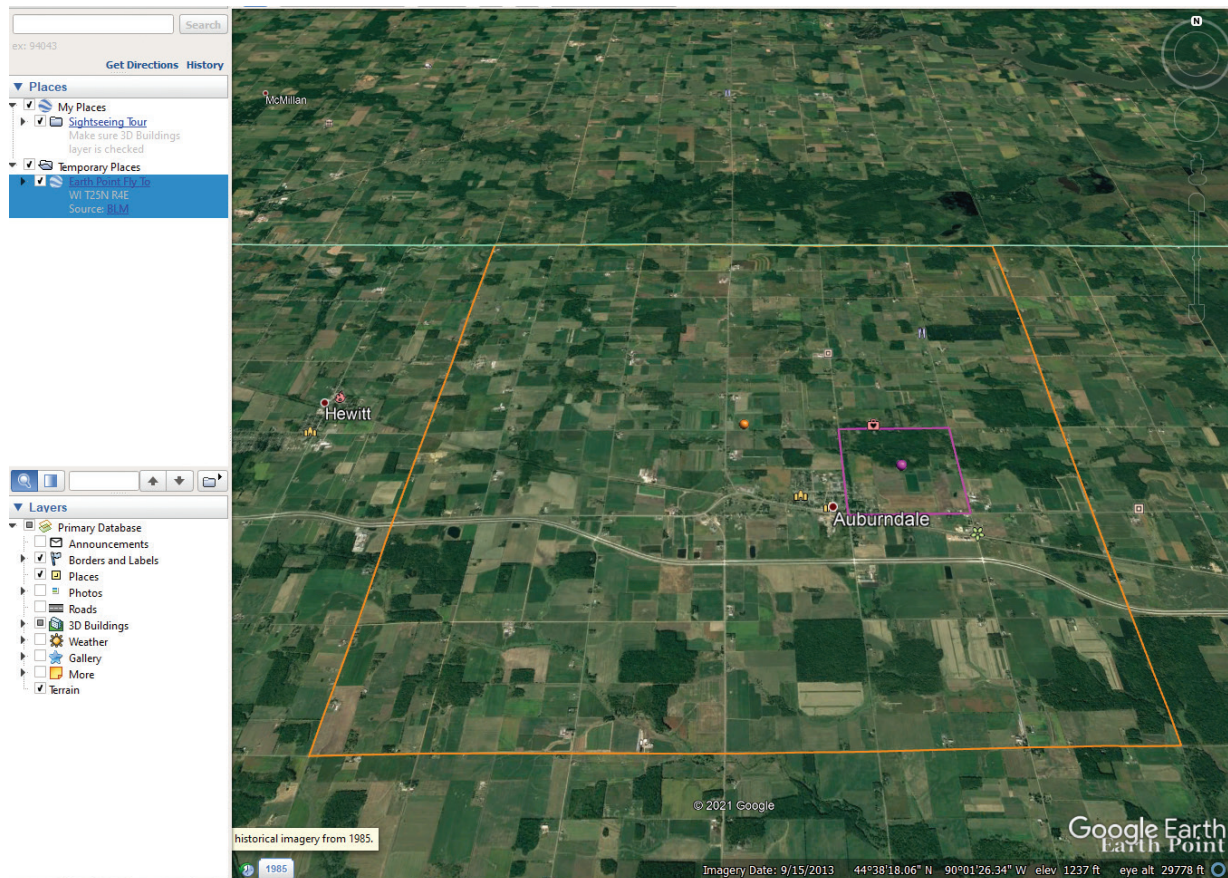


Figure 6. GoogleEarth view of the Auburndale facility showing the PLSS Township (in orange) and the Section (in purple).

In this specific example, you can zoom-in to the area of the plant and the sewage lagoon is visible in the Google Earth aerial photo, located exactly as described in the northwest quadrant of the southeast quarter-section.

Knowing the Public Land Survey System nomenclature and PLSS locators can add fast and reliable information to a GIS inquiry.

Send your questions, comments, and tips to GISTT@asprs.org.

Al Karlin, Ph.D., CMS-L, GISP, and Brandon Gravett are with Dewberry's Geospatial and Technology Services group in Tampa, FL. As a senior geospatial scientist, Al works with all aspects of Lidar, remote sensing, photogrammetry, and GIS-related projects. Brandon is a Geospatial Analyst who specializes in web-based GIS applications.

Book Review, continued from page 468

data and does not begin to cover everything that ArcGIS Pro can do. This knowledge is particular to ArcGIS Pro, although other software may have similar tools and functionality.

Despite its success in achieving its stated goals, the title *Focus on Geodatabases in ArcGIS Pro* is not very descriptive of the breadth or emphasis of the book. Data Integrity with Geodatabases in ArcGIS Pro or Focus on Data Quality and Maintenance with Geodatabases in ArcGIS Pro are more descriptive, if wordier, alternatives as one of its potential strengths is helping GIS professionals' transition from ArcGIS Desktop to ArcGIS Pro.

Focus on Geodatabases also lacks a conclusion, with a review of the geodatabase topology section being the final text. This is a missed opportunity to emphasize the attention to detail required over the life course of operational spatial data.

Users achieve quality spatial data by not only having sound data design and implementation but also careful use of appropriate data creation and editing techniques verified by quality assurance and topology checks.

Overall, *Focus on Geodatabases* achieves its goals and provides a solid introduction, textbook or GIS lab manual, or transition guide to both geodatabases and editing functionality in ArcGIS Pro. The real-world data scenarios are an asset to classroom use and relate to working professionals. As a textbook, *Focus on Geodatabases* is ideal for instructors that wish to emphasize planning before doing, creating and editing realistic local government property and utilities data, and maintaining data quality through structural geodatabase settings, good technique, and topology tools.

BECOME A MENTOR TO A GEOSPATIAL STUDENT!

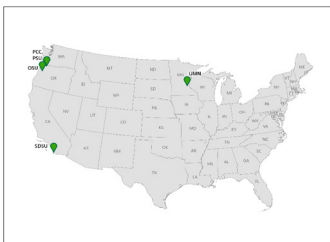
As we network within our ASPRS Chapter community, we are excited to highlight a new program that is seeking energized geospatial professionals to serve as mentors. Please consider volunteering a little bit of your time and expertise with student members!

As a mentor, you can help a student navigate job applications, understand the publishing process, and grow their confidence! This year has been hard, and many students are experiencing additional stresses as they find their next step in their academic and professional careers. Whether you are an established professional in your field or just breaking into a new career, your experience, support, and encouragement could make all the difference in a student's journey forward.

Please consider joining our mentor program by sending us a short statement of interest to sac@asprs.org.

Student Chapter Mixer Event!

This month, several student chapters met via zoom to exchange tips on how to be a successful student geospatial organization. The chapters were represented by their presidents:



- ◇ Liz Cave, Portland Community College
- ◇ Maria Krivova, Oregon State University
- ◇ Audrey Lothspeich, University of Minnesota
- ◇ Holly Romer, Portland State University
- ◇ Krista West, San Diego State University

These dedicated students spent an hour discussing what has worked well regarding group cohesion, event planning, and student engagement during such a difficult year. As zoom is now the norm for meetings, this selection of student chapters was able to meet despite being (in some cases many miles apart) to offer support to each other.

DO YOUR PART & MENTOR A STUDENT!



CALLING ALL GEOSPATIAL PROFESSIONALS!

BECOME AN ASPRS MENTOR AND ASSIST STUDENTS WITH...

- Navigating job applications, resumes, and interviews
- Publishing in PE&RS and other geospatial journals
- Growing their leadership skills!

INTERESTED? EMAIL YOUR RESUME TO ASPRS STUDENT ADVISORY COUNCIL sac@asprs.org

Ideas for student engagement

During this meeting, the student chapter shared some useful tips for engaging students and building community. Check out the list below to help engage students in your school!

Start a Slack or Discord for casual chatting and document sharing

As students cannot meet in person to socialize, these chat platforms allow for a digital social space that can be loosely structured.

Host small, manageable workshops and presentations put on by students to show off their work.

These events do not have to be big or require a lot of planning. Instead, some chapters found that it was most effective given time and bandwidth to ask students to do skill shares or present their research. This kept students involved in their own community and with their peers and gave them opportunities to practice presenting in a casual setting. These presentations don't need to be geospatial in content but can cover anything a student is interested in sharing!

The SAC will be hosting another Student Chapter Mixer this summer to discuss member recruitment and plans for this upcoming year! If you would like to attend, please email sac@asprs.org.

ASPRS STUDENT ADVISORY COUNCIL

EVAN VEGA
COUNCIL CHAIR
LAUREN MCKINNEY-WISE
DEPUTY COUNCIL CHAIR

OSCAR DURAN
EDUCATION & PROFESSIONAL NETWORKING CHAIR
RANDI BOLT
DEPUTY EDUCATION & PROFESSIONAL NETWORKING
TERRA MCKEE
COMMUNICATIONS COUNCILOR

RABIA MUNSAF KHAN
DEPUTY COMMUNICATIONS COUNCILOR
KENNETH EKPETERE
CHAPTERS COMMITTEE CHAIR



& GRIDS & DATUMS

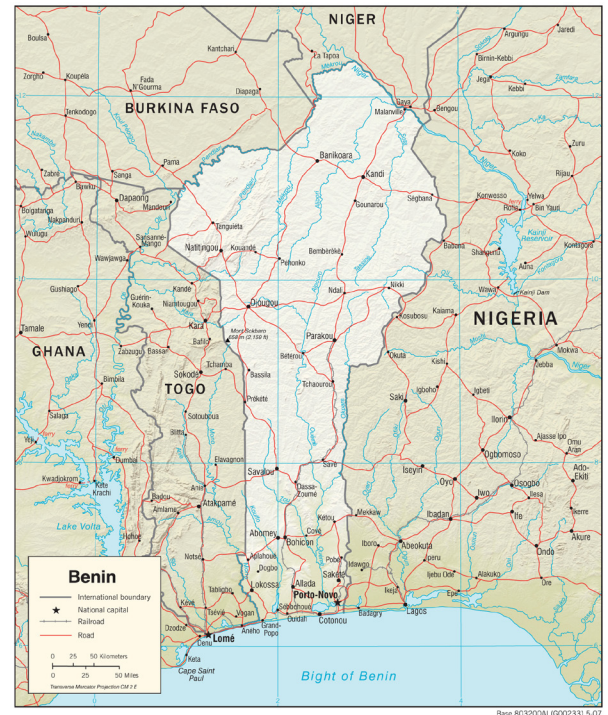
REPUBLIC OF BÉNIN

BY Clifford J. Mugnier, CP, CMS, FASPRS

The Grids & Datums column has completed an exploration of every country on the Earth. For those who did not get to enjoy this world tour the first time, *PE&RS* is reprinting prior articles from the column. This month's article on the Republic of Bénin was originally printed in 2003 but contains updates to their coordinate system since then.

In the 15th century, the site of the most organized kingdom of West Africa was at Abomey until the Portuguese came to the region in 1485. The kingdom of Great Bénin exerted great influence in the 17th century; the French established a trading presence in Cotonou (1851) with King Gezo. Temporarily suspended, the French reestablished former rights at Porto-Novo in 1863, and protection was extended to various other political entities along the coast and in the interior. Dahomey eventually was made an overseas territory of France in 1946, and it became independent in 1960. Dahomey's name was changed to Bénin in 1975. Bénin is bordered on the west by Togo (644 km), on the south by the Atlantic Ocean (121 km), on the east by Nigeria (773 km), and on the north both by Niger (266 km) and by Burkina Faso (306 km). The lowest point is the Atlantic Ocean, the highest point is Mount Tanekas (641 m), and Bénin is slightly smaller than the state of Pennsylvania. Although the country is mostly flat to undulating plains, there are some hills and low mountains.

When the federation of the eight territories constituting former French West Africa came into being in 1904, the *Annexe de l'Institut Géographique National à Dakar* (Senegal) became responsible for the official mapping. At the time, the IGN Annex, Dakar was known as *Service Géographique de l'Afrique Occidentale Française* – SGAOF (Geographic Service of the French West Africa). Topographic mapping of Bénin by SGAOF was largely at the scales of 1:200,000 and 1:500,000. The methods originally used were rapid ground mapping (using planetable and alidade with graphical triangulation). The Clarke 1880 was the ellipsoid of reference for



these series. In December 1945 the *Cabinet du Directeur, Institut Géographique National* in Paris issued an instruction concerning the systems of projection to be utilized in French West Africa. The instruction detailed that a Gauss (Gauss-Schreiber Transverse Mercator) system of projection was to be used for the group of regular map compilations and related works that included geodesy, topography, photogrammetry, and cartography for a range of scales that included 1:200,000. All of the map series were to be cast on the International Map of the World sheet system based on the graticule. In particular, *Fuseau Dahomey* was defined with a central meridian, $\lambda_0 = 0^\circ 30'$ East of Greenwich, a scale factor at origin, $m_0 = 0.999$, and both False Easting and False Northing equal to 1,000 km. The limits of the Dahomey Zone grid were defined between 3° West to 4° East. The ellipsoid of reference was defined as the Hayford 1909 (International) where $a = 6,378,388$

Photogrammetric Engineering & Remote Sensing
Vol. 87, No. 7, July 2021, pp. 473–476.
0099-1112/21/473–476

© 2021 American Society for Photogrammetry
and Remote Sensing
doi: 10.14358/PERS.87.7.473

m and $1/f = 297$. The detailed measures that were to be taken by the Colonial Inspector Generals in charge included training their staffs to use the new tables of projection.

Within five years, French coordinate systems changed to UTM throughout the world with the exceptions of Madagascar (*PE&RS*, February 2000) and Reunion. In terms of far-reaching developments in grid system usage, this was spectacular! D. R. Cockburn and W. L. Barry of Army Map Service translated the IGN Instruction dated 20 September 1950:

“1. The General Directorate has decided to abandon the projection systems now in use in the French Overseas Territories and Departments and to utilize henceforth, in all these territories, a new projection system called the Universal Transverse Mercator (*Mercator Transverse Universelle*), having a unique definition.

In-so-far as Madagascar is concerned, the use of the Laborde Projection will be continued without change. Similarly for Reunion, the Gauss system, in which the triangulation of the island has been computed, will be retained. With the exception of these two particular cases, the U.T.M. projection will from now on be the only official projection in the French Overseas Territories and Departments.

Consequently I.G.C. instruction No.1212, dated 12 December 1945, is rescinded.

2. The new projection is a Gauss conformal projection applied to zones of 6° of longitude in width. These zones, identical to those of the 1:1,000,000 International Map of the World, are indicated on the attached index map.
3. For a long time, views have been expressed in the international meetings of geodesists in favor of a universal projection system, which would be adopted by all the countries of the world. Inspector General Tardi proposed himself at the General Assembly of the International Association of Geodesy at Edinburgh (1936), a Gauss projection in 6° zones for the African continent, which is the same as the UTM projection. These views remained the dead issue for a long time. Before 1940, each country was quite satisfied with its own projection system and was reluctant to undertake the enormous task of converting coordinates into a universal system. They were especially reluctant to modify their quad printing plates. However, during the course of the last war, the extension of military operation to vast regions of the globe, the strategic deployments on a great diversity of war-fronts entailed the creation of a great number of projection systems (in 1945, over 100 of these systems were in use). As a result, a state of utter chaos ensued and considerable expense was entailed for the computation of the transformation and the adaptation operations. Consequently, the prospect of a universal projection system aroused much interest in the post war period.

The United States was very much in favor of the project and to facilitate its adoption by the various countries, Gauss projection tables (called a UTM projection) were computed and published. These tables were computed in the sexagesimal angular division system. The American agencies also computed the same tables on a centesimal system.

The Institut Géographique National, when asked to adopt the new projection in December of 1949, did not hesitate in agreeing to its use for French Colonial regions with certain exceptions which are explained below. In point of fact, it was entirely possible to adopt this new projection for the major part of the colonial possessions at a very small cost. However, a problem arose for its use in France proper and in North Africa. For France itself, a 6° belt UTM projection leads to very extreme scale changes, i.e., extreme from the point of view of civilian use.

4. Actually, it was not merely in a spirit of international cooperation that the Institut Géographique National agreed to the new projection but also because it offers incontestable practical advantages. In December 1949, the situation was as follows:

After long conferences in which various proposals were suggested, we finally adopted the solution proposed by General Laborde for our overseas possessions at the end of 1945. this solution was as follows: A Gauss system (double projection) on the international Ellipsoid with φ_0 equaling 0° in French East Africa and French West Africa. For the smaller regions (Guadeloupe, Martinique, Reunion, etc.) the value of φ_0 is equal to the mean latitude of the territory, φ_0 being the latitude of the central point. This procedure leads to the establishment of separate tables for each value φ_0 .

Tables for the conversion of geographic coordinates into rectangular and vice versa (tables which would produce the centimetric precision necessary for geodetic computations) had not been set up at the end of the year 1949 with the exception of tables covering a few small regions. Although this is a very pressing urgency, the Institut Géographique National, due to limit (sic) means, has neither the facilities for computing the tables rapidly nor for editing them without detriment to other equally urgent tasks.

Considering on one hand the small number of stations to be converted into the new system (for astro points the work involved is insignificant) and considering that the dimensional variations of the sheets already published would be less than the standard size, the Institut Géographique National has agreed to rapidly extend the UTM projection in these territories being aware of the following factors:

That the United States was in a position to immedi-

ately deliver to us as many copies as was necessary of the tables computed on the sexagesimal system and contracted to compute the same tables on the grad system; that the United States was able to undertake the conversion of coordinates into the system using data obtained from electronic computing machines.

5. In point of fact, the UTM projection as it has been already adopted (or in the course of being adopted) by a number of countries is not absolutely 'Universal.' This would have been the case if a uniform ellipsoid had been chosen for all the countries. However, the difficulties entailed in changing ellipsoids is common knowledge and because of this, the basics of the ellipsoids in use for the various continents have been retained. Accordingly, the Clarke 1866 ellipsoid has been kept in use for North America; the International Ellipsoid has been adopted for South America and the Pacific regions, and the Everest Ellipsoid has been chosen for the East Indies and the adjacent regions. So as to fulfill a request made by the British who have already computed vast geodetic nets on the Clarke 1880 Ellipsoid, the Institut Géographique National has adopted this ellipsoid for the entire African continent. In addition, this ellipsoid was used for French geodetic work previous to 1945.

6. The UTM projection may be defined as having the following intrinsic properties:

It is a Gauss conformal projection, a direct projection of the ellipsoid on the plane. Linear values are maintained on the prime meridian of the projection with the exception of a scale-reduction which is defined by the following coefficient: $k_0 = 0.9996$.

The zones have an overall width of 6° in longitude (3° on each side of the central meridian). The zones coincide with those of the 1:1,000,000 International Map. The Greenwich meridian is at the limit of two zones (zone numbers 30 and 31). These basics will suffice to define the projection for any given ellipsoid.

7. The new UTM projection differs from the Gauss projection adopted at the end of 1945 in the sense that it is a direct projection of the ellipsoid on the plane instead of being an indirect projection employing the intermediary of a sphere upon which the ellipsoid is first applied before projecting it on the plane.

The new projection retains the linear values on the central meridian of each zone to the approximate scale factor. The former projection did not retain linear values on this meridian.

In toto, the basics of the two projections are, at least within the limits of the proposed narrow zones, absolutely comparable and considered from the view point of practical application it is impossible to give prefer-

ence to either one or the other. The only advantage of the former projection is that of adapting itself more simply to the extension of latitudinal belts and that this predicament will not arise for overseas geographic services.

8. Covering memo No. 1 in reference to the implementation of the new projection program is to be effective immediately. Director, Institut Géographique National."

The instruction quoted above was accompanied with some specific procedures for all of the French colonies, territories, and departments. With respect to French West Africa (and Bénin), IGM explained that AMS agreed to compute the UTM coordinates of all astro points that were observed as control for the 1:200,000 scale topographic maps.

In January and February of 1952, Hydrographic Engineer Bourgoin of the French Navy directed a port survey of Cotonou in support of a new wharf. The survey included depth soundings, current measurements, measurement of the period, direction, and amplitude of the tide, observations of the characteristics of the local sea, soundings in the adjacent lagoon, and granularity determinations of the bottom. A local coordinate system was devised with the origin of $X = 10,000$ m and $Y = 1,000$ m at the church steeple. The Cotonou Lighthouse was calculated to have the coordinates $X=10,241.75$ m and $Y=508.01$ m. This local grid was oriented by tachéomètre (used at the time in Europe for cadastral surveying and distance measurement with subtense bar) to star observation, and scale was provided by a 50-meter triangulation baseline. No geodetic coordinates were given for the origin point.

A Franco-German protocol of 9 July 1897 delimited a boundary between German Togo and the French possessions of Dahomey and Soudan (presently Upper Volta). The affirmed convention boundary utilized the lagoon eastward from Île Bayol to the Mono river and then follows the river northward to the 7th North parallel, thence various jogs, thalwegs, and meridians to the tripoint with Upper Volta (now Burkina Faso). Straight lines were defined according to French topographic mapping and are therefore cast on the Gauss-Schreiber Transverse Mercator projection. Note that the thalweg is the "thread of the stream" and is not always equidistant between the two river banks.

The Bénin-Burkina Faso boundary is demarcated by the Mékrou and Pendjari rivers for about 85 percent of the distance. Between the rivers, the boundary follows the Chaîne de L'Atacora for about 25 miles to the tripoint with Niger. This boundary (and that with Niger), was determined most recently by a French statute of 27 October 1938 and re-established on 4 September 1947.

The Lagos area of Nigeria was ceded to the United Kingdom by a local monarch in 1861. With the expansion inland of both Bénin and Nigeria, the Anglo-French convention of 10 August 1889 delimited a boundary between the territories from the gulf of Guinea northward to the parallel of 9° N.

The Anglo-French agreement of 19 October 1906 and amendments made by the demarcation protocol of 20 July 1912 determined the final boundary between the two countries. Using numerous beacons (survey monuments), thalwegs of rivers, and straight lines on French 1:200,000-scale topographic maps, the boundary ends at the tripoint beacon with Niger.

In April 1959, the SGAOF name was changed to Service Géographique, Dakar –SG, Dakar (Geographic Service, Dakar) and in January 1961, to its present name. Topographic mapping of Bénin by IGN has been largely at the scale of 1:50,000. In the late 1940s and early 1950s, IGN compiled a small amount of topographic mapping at 1:20,000 scale and in the early through mid-1950s produced a small amount of mapping at 1:100,000 scale. After World War II the French adopted aerial photogrammetry controlled by astronomical points as the means for surveying at the scales of 1:50,000 and 1:200,000. The reader is reminded that when comparing mapping technology of the 1950s to the present, a shirt-pocket consumer grade GPS receiver is about five times more accurate than a classical “astro point.”

The closest major classical datum to the Republic of Bénin is the Minna Datum of 1927. The origin is at station L40, which is the north end of Minna Base in the town of Minna, Nigeria where $\Phi_0 = 09^\circ 39' 08.87''$ N, $\Lambda_0 = 06^\circ 30' 58.76''$ East of Greenwich, and the ellipsoid of reference is the Clarke 1880 where $a = 6,378,249.145$ m and $1/f = 293.145$. In 1987, NIMA published the transformation parameters from the Minna Datum of 1927 to WGS84 Datum as $\Delta a = -112.145$ m, $\Delta f \times 104 = -0.54750714$, $\Delta X = -92$ m ± 3 m, $\Delta Y = -93$ m ± 6 m, and $\Delta Z = +122$ m ± 5 m, and this was a mean solution of six stations. In 1990, C.U. Ezeigbo published his solution of 11 stations for a Bursa-Wolf seven-parameter transformation as $\Delta X = -92.9$ m ± 1.6 m, $\Delta Y = -116.0$ m ± 2.3 m, and $\Delta Z = +116.4$ m ± 2.4 m, $R_x = -0.3'' \pm 1.1''$, $R_y = +3.0'' \pm 1.7''$, $R_z = +2.2'' \pm 1.5''$, and scale = $+1.00002 \pm 0.6 \times 10^{-5}$. This solution is intriguing because one station appeared to be between Lagos and Cotonou, according to the small-scale survey sketch by Prof. Ezeigbo.

Bénin Update

Seven CORS station were established in October 2008 through Millennium Challenge Account, Benin(MCAB) and National Geodetic Service, USA. Trimble NetR5 GNSS systems are being used in all the stations. The stations are being operated by Millennium Challenge Account, Benin (MCAB) and the 1'' GNSS data and other stations information is available at NGS website <http://www.ngs.noaa.gov/cors>. Their ITRF00 (1997.0 Epoch) positions were computed in August 2008 using 13-69 days of data. Source: National Geodetic Service USA, website., *AFREF News Letter No.11*, afref@rcmrd.org, May 2010.

Problem of the Use of Dual-Frequency Gns Receivers in Benin, Degbegnon, L., Koumolou, A., *Global Journal of Engineering Science and Research Management*, 5(11): November, 2018, ISSN 2349-4506. <http://www.gjesrm.com/Issues%20PDF/Archive-2018/November-2018/6.pdf>

According to Degbegnon & Aizo, the current local datum for Bénin is “Datum 58” with its origin at Point 58 southeast of the town of Dosso in the country of Niger and near the border with Nigeria where: $\Phi_0 = 12^\circ 52' 44.045''$ N, $\Lambda_0 = 3^\circ 58' 37.040''$ E of Greenwich. Thanks to John W. Hager, “Azimuth is $97^\circ 30' 04.237''$ to C. F. L. 1 from north. Elevation = 266.71 meters. Astro observed by IGN in 1968. This was used as a temporary datum pending the adjustment of the 12th Parallel to Adindan. It was for the section of the 12th Parallel in Niger and Upper Volta. Reference is Final Report of the 12th Parallel Survey in the Republic of Niger.” Surveyed in 1969 by the French IGN, the ellipsoid of reference is the Clarke 1880 where: $a = 6,378,249.145$ m., $1/f = 293.465$. This was used as the basis for computation of the 12th Parallel traverse conducted 1966–70 from Senegal to Chad and connecting to the Adindan triangulation in Sudan. The country is now moving to the WGS84 Datum (realization undefined), and the paper by Degbegnon & Aizo (below) discusses a Bursa-Wolf transformation between the WGS84 Datum and the local Datum 58.

Comparative study and determination of transformation parameters between: the permanent station system, the datum (58) and the Bénin geodetic System, Degbegnon, L., Aizo,P., *Research Journal of Recent Sciences*, Vol. 8(4), 1-8, October (2019) ISSN 2277=2502. <http://www.isca.in/rjrs/archive/v8/i4/1.ISCA-RJRS-2018-067.pdf>.

The contents of this column reflect the views of the author, who is responsible for the facts and accuracy of the data presented herein. The contents do not necessarily reflect the official views or policies of the American Society for Photogrammetry and Remote Sensing and/or the Louisiana State University Center for GeoInformatics (C⁴G).

This column was previously published in *PE&RS*.

Ad Index

National Reconnaissance Office

www.nro.gov/Business-Innovation-Opportunities/

Cover 2

JOURNAL STAFF

Editor-In-Chief

Alper Yilmaz, Ph.D., PERSeditor@asprs.org

Associate Editors

Rongjun Qin, Ph.D., qin.324@osu.edu

Michael Yang, Ph.D., michael.yang@utwente.nl

Petra Helmholz, Ph.D., Petra.Helmholz@curtin.edu.au

Bo Wu, Ph.D., bo.wu@polyu.edu.hk

Clement Mallet, Ph.D., clemallet@gmail.com

Jose M. Pena, Ph.D., jmpena@ica.csic.es

Prasad Thenkabail, Ph.D., pthenkabail@usgs.gov

Ruisheng Wang, Ph.D., ruiswang@ucalgary.ca

Desheng Liu, Ph.D., liu.738@osu.edu

Valérie Gouet-Brunet, Ph.D., valerie.gouet@ign.fr

Dorota Iwaszczuk, Ph.D., dorota.iwaszczuk@tum.de

Qunming Wang, Ph.D., wqm11111@126.com

Filiz Sunar, Ph.D., fsunar@itu.edu.tr

Norbert Pfeifer, np@ipf.tuwien.ac.at

Jan Dirk Wegner, jan.wegner@geod.baug.ethz.ch

Hongyan Zhang, zhanghongyan@whu.edu.cn

Dongdong Wang, Ph.D., ddwang@umd.edu

Zhenfeng Shao, Ph.D., shaozhenfeng@whu.edu.cn

Ribana Roscher, Ph.D., ribana.roscher@uni-bonn.de

Sidike Paheding, Ph.D., spahedin@mtu.edu

Contributing Editors

Highlight Editor

Jie Shan, Ph.D., jshan@ecn.purdue.edu

Feature Articles

Michael Joos, CP, GISP, featureeditor@asprs.org

Grids & Datums Column

Clifford J. Mugnier, C.P., C.M.S., cjmce@lsu.edu

Book Reviews

Sagar Deshpande, Ph.D., bookreview@asprs.org

Mapping Matters Column

Qassim Abdullah, Ph.D., Mapping_Matters@asprs.org

Sector Insight

Lucia Lovison-Golob, Ph.D., lucia.lovison@sat-drones.com

Bob Ryerson, Ph.D., FASPRS, bryerson@kimgeomatics.com

GIS Tips & Tricks

Alvan Karlin, Ph.D., CMS-L, GISP akarlin@Dewberry.com

ASPRS Staff

Assistant Director — Publications

Rae Kelley, rkelley@asprs.org

Electronic Publications Manager/Graphic Artist

Matthew Austin, maustin@asprs.org

Advertising Sales Representative

Bill Spilman, bill@innovativemediasolutions.com

AWARDS AND SCHOLARSHIPS COMING FALL OF 2021

ESTES MEMORIAL TEACHING AWARD

The Estes Memorial Teaching Award was inaugurated in 2003 in honor of Professor John E. “Jack” Estes, teacher, mentor, scientist, and friend of the American Society for Photogrammetry and Remote Sensing.

Funding for the Award, initially provided by a corporate sponsor, lapsed in 2016. In 2020-21, the ASPRS Foundation trustees, in recognition of the important niche this Award occupies in ASPRS, reallocated a portion of the Foundation’s general-purpose funds to fully endow the Award at a minimum \$2,000 level.

This Award, which includes a presentation plaque and a check, is intended to be presented annually. The purpose of the Award to recognize individual achievement in the promotion of remote sensing and geographic information systems (GIS) technology and applications through educational efforts. Award recipients are chosen based on documented excellence in education, teaching, mentoring, and training.

Nominations for the Award are solicited from active members of ASPRS, including representatives from ASPRS’s Regions, by the Estes Award Selection Committee and are evaluated based on the following criteria:

- Professional duties with a significant role in education, teaching, mentoring, and training in the areas of remote sensing and GIS
- Documented excellence in education, teaching, mentoring, and training
- A demonstrated commitment to the advancement of student learning in remote sensing and GIS

Further information and application details will be available on the ASPRS web site in the early Fall.

ASPRS GOVERNMENT SERVICES SCHOLARSHIP

The Awards Committee of the American Society for Photogrammetry and Remote Sensing (ASPRS) and the ASPRS Foundation announce the new ASPRS Government Services Scholarship for the 2022 application cycle. The scholarship is fully endowed at the initial amount of \$5,000, with potential for the award amount to grow in future years.

This scholarship, to be awarded annually, is designed to encourage upper-division, undergraduate-level and graduate-level college students in the United States or Canada to pursue a course of study in photogrammetry and

NEW ASPRS MEMBERS

ASPRS would like to welcome the following new members!

Alaska

Anke Gleitsmann, Ph.D.
Sean Mack

At Large

Robert Neville
Eduardo Hector Rotundo
Ahmed Sefi
Katherine Tuinman

Cascadia

Christina Friedle
Nicholas Clark Wilson
Erica Wynter

Eastern Great Lakes

Jessica Baculik
Kayla Keller
Meri Koskelainen
Alyssa Sklar
Alistair J H. Smith
Madeline Stewart
Jennifer Sturges
Michael Thomas

Florida

Shelby A. Berg
Paul J. DiGiacobbe, P. E.
Benjamin Lucero
John Blair Northrop
David Joseph O'Brien, Jr.

Gulf South

Josh Adams
William Marshall Alexander
Robert Bartlett
Julia Blaise Guidry
Coryell Kelsey
Chad Netto
Christopher Nixon
Angie Swirski

Heartland

Umesh Acharya
Patrick M. Bailey
Derek M. Cain
Adam Campbell, CMS
Melissa Glauber
Glenn Humphress

FOR MORE INFORMATION ON ASPRS MEMBERSHIP,
VISIT [HTTP://WWW.ASPRS.ORG/JOIN-NOW](http://www.asprs.org/join-now)

Mid South

Anna Victoria Kaufmann
David L. Page, Ph.D.
Michael Strunin
Taylor Watson

North Atlantic

Brandon Gravett
Russell F. Schimmer

Northeastern

Harry Crissy
Justin D. Gates
Preston Hartzell
Michael Parkin
Robin Poot
Udayalakshmi Vepakomma, PhD
Graylin C. Worcester

Pacific Southwest

Mark Allen
Chad Nathaniel Contreras
Brandon Glantz
Nicholas Lewin
Paul Read
Cengiz Yagcioglu

Potomac

Yvonne N. Harding
Chris McPartland
Farid Qamar
Mark Thomas
Andy Watiker
Daniel A. Zimble

Rocky Mountain

Glenn A. Farrington
Erik S. Halverson, CP
Douglas Eugene Jacoby, CMS
Jeff Lewis
Michael Tuffly, PhD, CMS
Robert Valentine

related topics leading to a career in the geospatial mapping profession in the government sector (federal, state or local) within the United States. The scholarship also encourages geospatial professionals already in government service to pursue advanced degrees and provides a preference to U.S. veterans. ASPRS membership (active or student) is required.

An eligible candidate who wishes to be considered for the scholarship must submit an on-line application that includes the following items:

- A listing of courses taken or planned in photogrammetry and related geospatial information technologies, recognizing that instruction in remote sensing is often embedded in courses taught in many different disciplines.
- A transcript of all college/university level courses completed, and grades received, to demonstrate scholastic ability.
- A listing of internships, special projects, or work experience; technical papers, research reports or other documents; courses taught as a lecturer or teaching assistant; and presentations made that demonstrate the applicant's capabilities in this field.
- Two letters of recommendation from faculty members or professionals having knowledge of the applicant's capabilities (demonstrated or potential).
- A statement, not to exceed 2 pages, detailing the applicant's educational and research goals that relate to the advancement of photogrammetry and related geospatial information technologies and the applications of these technologies.

Further information and application details will be available on the ASPRS web site in the early Fall.

ASPRS PARTNERS WITH PROMETRIC TO PROVIDE ALL FUTURE ASPRS CERTIFICATION EXAMS

This new partnership:

1. Removes the need for candidates to coordinate proctors
2. Allows for examinations to be offered in a Covid-safe environment
3. Provides immediate test results to the candidate
4. Allows for "remote proctoring" for candidates who do not have a Prometric testing center near their locations, to include international candidates

For more information regarding the ASPRS Certification Program, please click the button below or send questions to applications@asprs.org.

Three-Dimensional Reconstruction of Single Input Image Based on Point Cloud

Yu Hou, Ruifeng Zhai, Xueyan Li, Junfeng Song, Xuehan Ma, Shuzhao Hou, and Shuxu Guo

Abstract

Three-dimensional reconstruction from a single image has excellent future prospects. The use of neural networks for three-dimensional reconstruction has achieved remarkable results. Most of the current point-cloud-based three-dimensional reconstruction networks are trained using nonreal data sets and do not have good generalizability. Based on the Karlsruhe Institute of Technology and Toyota Technological Institute at Chicago () data set of large-scale scenes, this article proposes a method for processing real data sets. The data set produced in this work can better train our network model and realize point cloud reconstruction based on a single picture of the real world. Finally, the constructed point cloud data correspond well to the corresponding three-dimensional shapes, and to a certain extent, the disadvantage of the uneven distribution of the point cloud data obtained by light detection and ranging scanning is overcome using the proposed method.

Introduction

Three-dimensional (3D) reconstruction, an important environmental perception and computer vision technology, has good application prospects in fields such as autonomous driving, virtual reality, medical image processing, architectural design, and cultural relic protection. According to different reconstruction targets, the 3D reconstruction of an image can be divided into large-scale scene reconstruction and single-target reconstruction. Scene reconstruction technology is relatively mature, and researchers have produced open-source and commercial 3D reconstruction software based on the structure from motion (Schönberger and Frahm 2016) and multi-view stereo (Jancosek and Pajdla 2011) algorithms. The present article is related to target reconstruction.

Existing 3D models can be divided into four main types based on their mode of expression: depth image, voxel grid, and point cloud. For the human eye, a depth image cannot show 3D shapes well. Further, voxel grid representations can be directly processed by 3D convolutional neural networks (CNN). However, the volume cost will be exceedingly high and the processing speed slow. Therefore, the resolution should be reduced, which in turn will result in a quantization error. Although point cloud is not coherent in terms of expression, it has the advantages of a simple structure, ease of learning, and convenient geometric transformation. Point cloud data, a collection of points containing 3D coordinate information, can be obtained using a light detection and ranging (lidar) scanner. According to whether the acquisition device actively emits

measurement signals, traditional 3D reconstruction methods are divided into two categories based on active and passive vision theories. Active vision-based 3D reconstruction is used to obtain the depth information of the target by comparing the gap between emission and reception using energy sources, such as lasers. Active methods can be divided into the Moiré fringe, time-of-flight (ToF), structured light, and triangulation methods. Among them, the 64-line real-time lidar on Google's driverless car uses ToF to measure the relative distance between the surfaces of objects and the device to obtain point cloud data. To restore 3D information, the passive vision-based 3D reconstruction method uses a camera to estimate the depth of two-dimensional (2D) images obtained by the 2D projection of the 3D world. Multi-view stereo vision reconstruction uses a set of images of the target object, obtained from different perspectives, for feature matching and then uses the matched feature points to complete the point cloud reconstruction. In fact, in many cases, we cannot obtain images of the target at multiple angles simultaneously, especially when real-time 3D reconstruction is required during driving. Therefore, it is necessary to use a single 2D picture to perform 3D reconstruction. In traditional methods, monocular vision reconstruction is more difficult because a single image corresponds to a variety of possible real targets, and prior knowledge is required to solve the uncertainty of the prediction of the invisible part of the image. This is also one of the challenges of the 3D reconstruction of a single image. Deep learning allows computers to learn the manner in which the human retina captures 3D shapes and completes the 3D reconstruction of a single picture. With the gradual development of neural networks, 3D reconstruction methods based on deep learning have shown remarkable performance. Fan *et al.* (2017) used an autoencoder (Shao 2019) to build a single input-image point cloud generation network, and they were the first to use deep learning to achieve point cloud generation. Since then, researchers have continuously developed point cloud generation networks (Sun *et al.* 2019; Mandikal and Babu 2019; Mandikal *et al.* 2018) based on single input image.

Simultaneously, large-scale computer-aided design (CAD) model libraries, such as ShapeNet (Chang *et al.* 2015), ModelNet (Vishwanath *et al.* 2009), and PartNet (Yu *et al.* 2019), have appeared in recent years. These 3D model libraries have played a very important role in 3D reconstruction tasks. In the past, many point cloud-based 3D reconstruction tasks were conducted using these modeling data, but the real situation is often suboptimal: (1) the target in the picture is occluded; (2) the point cloud data only correspond to the surface of the target from one perspective; and (3) the point cloud data are unevenly distributed (Zhai *et al.* 2020). This study aims to use neural networks to predict the structure of a 3D point cloud for a given image. Owing to the large difference between the

Yu Hou, Rui-feng Zhai, Xue-yan Li, Jun-feng Song, Xuehan Ma, Shu-zhao Hou, and Shu-xu Guo are with the State Key Laboratory on Integrated Optoelectronics, College of Electronic Science and Engineering, Jilin University, Changchun, China (leexy@jlu.edu.cn).

Rui-feng Zhai, Xue-yan Li, and Jun-feng Song are also with Peng Cheng Laboratory, Shenzhen, China.

Contributed by Zhenfeng Shao, October 31, 2020 (sent for review December 28, 2020; reviewed by Hongping Zhang, Nan Yang).

Photogrammetric Engineering & Remote Sensing
Vol. 87, No. 7, July 2021, pp. 479–484.
0099-1112/21/479–484

© 2021 American Society for Photogrammetry
and Remote Sensing
doi: 10.14358/PERS.87.7.479

modeling data and the read data, a model trained using modeling data is often difficult to apply in practical situations. In contrast to the aforementioned studies, we implement 3D reconstruction based on a real road data set, Karlsruhe Institute of Technology and Toyota Technological Institute at Chicago (KITTI) (Geiger *et al.* 2013). This study uses a semiautomatic segmentation program to achieve single-objective data set production. Such data help our network to better simulate real-world situations. The up-sampling part of the point cloud can counteract the shortcomings of overly sparse point cloud data in the data set to a certain extent. We also used an encoder-decoder network to complete the reconstruction of 3D point cloud data. The content of this article includes the following:

- We propose a method to create the data set required for 3D reconstruction based on the open-source KITTI data set;
- A new neural network model for efficiently generating dense point cloud shapes is proposed. Unlike previous 3D reconstruction studies, the 3D reconstruction of the vehicle target in this study is based on the road data of real urban environments;
- A point cloud up-sampling module in the network is proposed to make the point cloud data dense according to the characteristics of the multi-line lidar scanning point cloud data. It can improve the predictive point cloud effect of a single input image.

Method and Materials

Method

Based on the vehicle-mounted lidar point cloud data and the corresponding 2D images, we designed a real point cloud reconstruction network for a single input image. In this section, we will introduce the overall content and design process

of the network in detail. First, we will introduce the 2D image data used by Mask region-based convolutional neural networks (R-CNN) (He *et al.* 2017) to train the network. Second, we will describe the point cloud up-sampling method in detail. Finally, we will describe how the reconstruction network converts the input 2D road vehicle target image (red-green-blue (RGB)) into a 3D point cloud $S = \{(x_i, y_i, z_i)\}_{i=1}^N$. Figure 1 shows the pipeline of our entire experiment.

Mask R-CNN was developed from R-CNN (Girshick *et al.* 2014), Fast R-CNN (Girshick 2015), Faster-RCNN (Ren *et al.* 2017), and fully convolutional networks (FCN) (Long *et al.* 2015). R-CNN uses the selective search method to generate one to two thousand candidate regions on the input image. Subsequently, the neural network of the winding machine is used to extract the image features in the candidate area to obtain the corresponding feature map. R-CNN performs a substantial amount of repetitive work in the image feature extraction stage, whereas Fast-RCNN simplifies the feature extraction stage. Fast-RCNN uses a neural network to extract high-dimensional features of the entire image at once and obtains the feature map of the candidate region through the mapping between the image and the feature map. Faster-RCNN uses region proposal network structures instead of the selective search method to generate candidate frames, and it uses neural networks instead of the support vector machine to implement tasks such as classification. Mask R-CNN adds FCN based on Faster-RCNN, which can complete target detection tasks and instance segmentation tasks on the Common Objects in Context (COCO) (Lin *et al.* 2014) data set.

The segmentation results of Mask R-CNN meet most of the requirements of image segmentation. Mask Scoring R-CNN was proposed in 2019 by Huang *et al.* (2019), who added a new

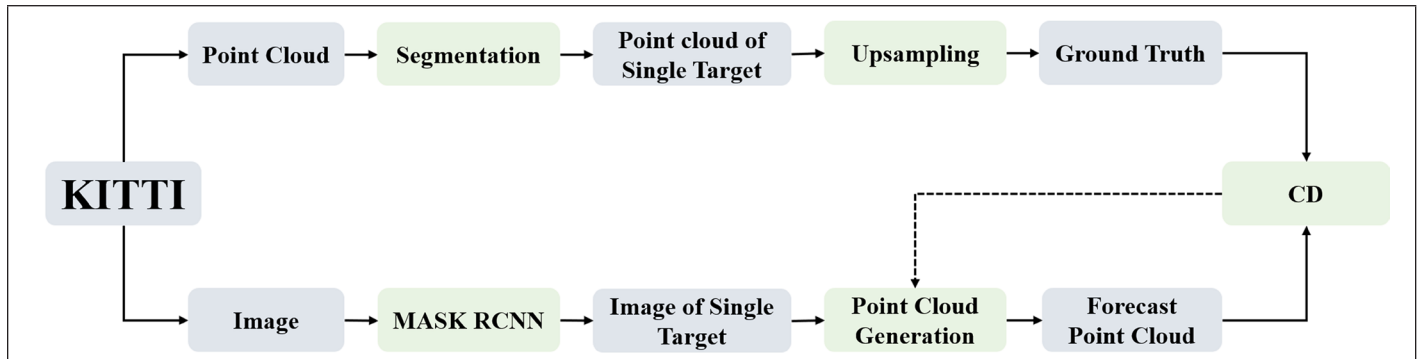


Figure 1. Pipeline of the present study. The reconstruction network is divided into two stages: In the first stage, the trained Mask region-based convolutional neural networks is used to segment the input image; in the second stage, the segmented image is reconstructed from the point cloud. The point cloud output predicted by the network is similar to the lidar scan result.

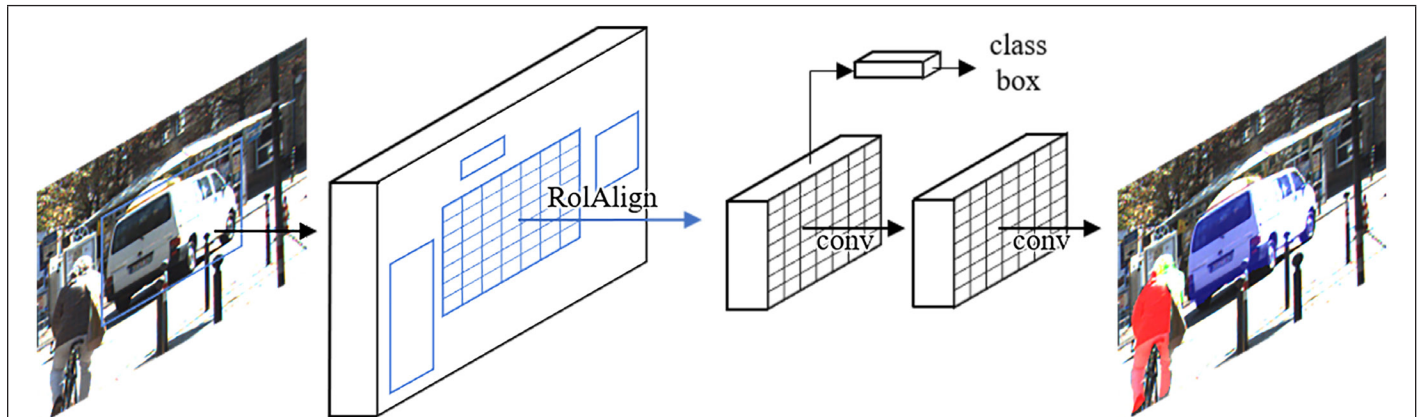


Figure 2. Mask region-based convolutional neural networks image segmentation process.

scoring method (mask score) based on Mask R-CNN. The Mask Scoring R-CNN model learns a score for each mask instead of using its classification score. We believe that the space and time complexity of Mask Scoring R-CNN are higher than those of Mask R-CNN. Therefore, this study chooses Mask R-CNN as the segmentation model.

Up-Sampling Method

Point Cloud Library (Rusu and Cousins 2011) used the moving least squares (MLS) algorithm for up-sampling. It reconstructs surfaces through an algorithm and traverses all the

points in the point cloud for interpolation, allowing outliers and surface vacancies in the point cloud to be removed. This is a process of performing the interpolation of existing point cloud data; therefore, the reconstruction result will not be completely accurate. This study also uses an interpolation method for point cloud up-sampling. Considering the characteristics of the point cloud data scanned by the multi-line lidar, the point nearest to each point must appear on a line, as shown in Figure 3b. To make the points added by up-sampling appear between the lines, we shifted our attention from the nearest point to the other points contained in the

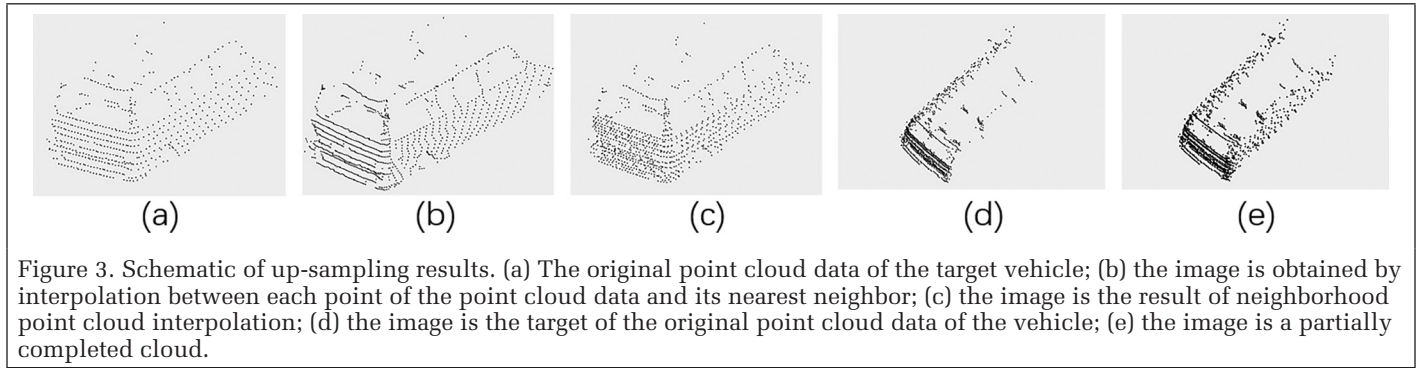


Figure 3. Schematic of up-sampling results. (a) The original point cloud data of the target vehicle; (b) the image is obtained by interpolation between each point of the point cloud data and its nearest neighbor; (c) the image is the result of neighborhood point cloud interpolation; (d) the image is the target of the original point cloud data of the vehicle; (e) the image is a partially completed cloud.

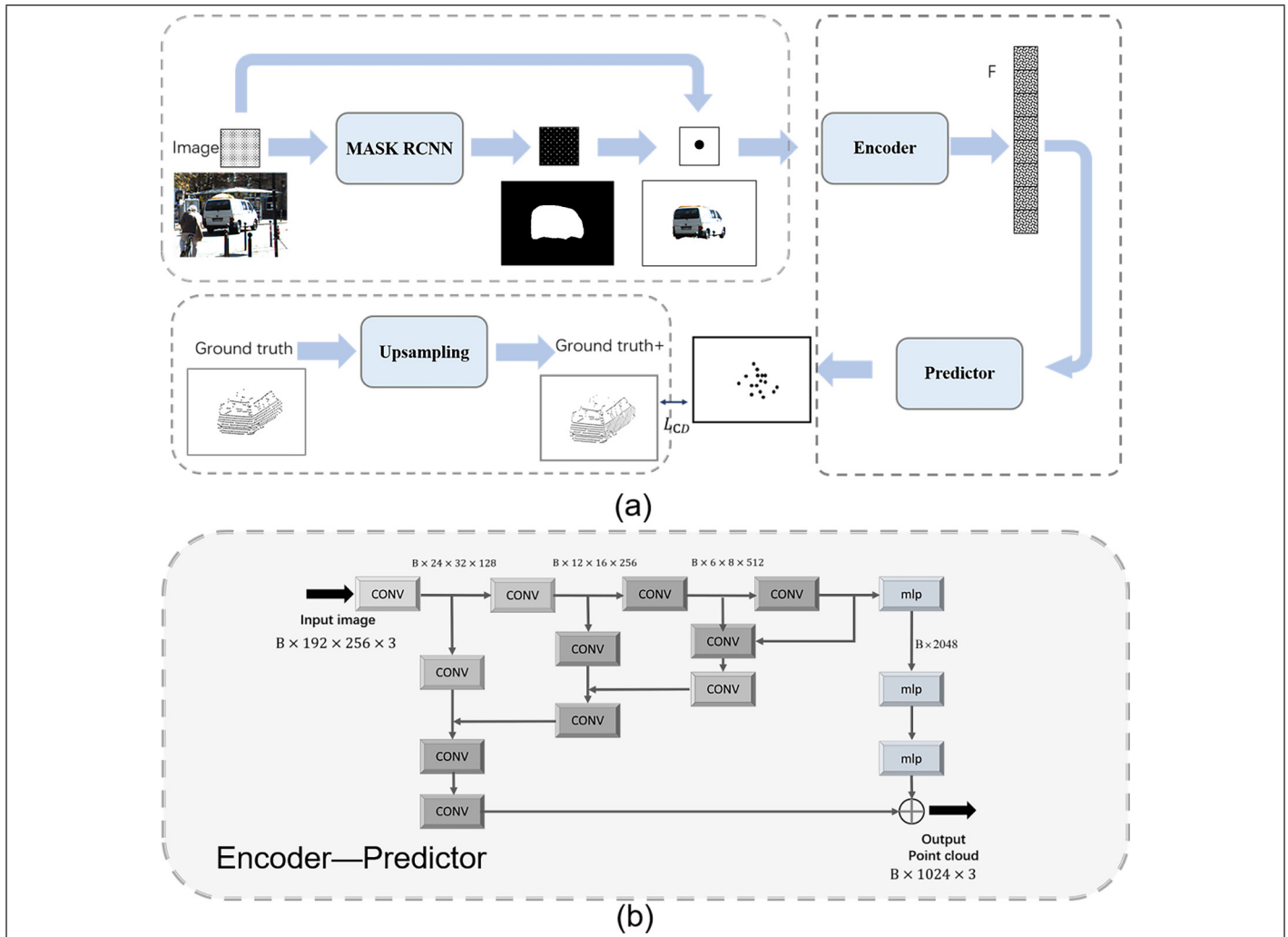


Figure 4. Point cloud generation network structure. (a) F is the latent features of the image in high-dimensional space; L_{CD} is the loss of the network (see the section “Point Set Generation Net”); (b) this subfigure is the network structure of the autoencoder in (a). “B” represents batch size.

neighborhood of each point. Note that here the point cloud data in KITTI can be approximated as multi-line scanning lines perpendicular to the z-axis. Find a point and set the Euclidean distance as the neighborhood radius. Subsequently, find a point in the neighborhood whose z value differs from that of this point by more than a small number. Figure 3c is obtained by interpolating such points.

In the actual environment, the multi-line lidar can scan only one side of the target object, and the point cloud data obtained by scanning are incomplete. The most commonly used methods are as follows: (1) Fill in the incomplete part by inputting geometric hints (Berger *et al.* 2014). (2) The symmetry axis is determined to complete the repetitive structure (Sipiran *et al.* 2014; Sung *et al.* 2015). (3) Learn the geometry of the missing part through deep learning and restore the 3D shape of the target (Yuan *et al.* 2018). The Point Completion Network realizes the completion of incomplete target point clouds. Here, we considered a simple up-sampling method, based on the symmetry of the 3D object, to partially complete the point cloud of the target vehicle, as shown in Figure 3e. Through simple point statistics, we can easily find the symmetry plane separating the left and right sides of the vehicle. The two parts of the point cloud space separated by a plane can share information with each other to achieve partial completion of 3D point cloud data. To facilitate calculation using a computer, we up-sampled the point cloud to 1024 points, as shown in Figure 3(e).

Point Set Generation Net

A point cloud generation network is important for realizing single input-image point cloud reconstruction. Based on this, to simulate a real point cloud data set, we proposed a ground truth (GT) up-sampling module. The nonuniqueness of the GT is caused by the discontinuity of point cloud data. In the real data set, it can be understood that the point cloud data obtained by the lidar will not be exactly the same every time the lidar scans the same target object.

We propose a real point cloud reconstruction network for single-input RGB images (Figure 4). A network that simulates the nonuniqueness of a GT is added based on the point set generation network. Our network is mainly divided into three modules: image coding module, point cloud prediction module, and GT up-sampling module, as shown in Figure 4. The image coding module is composed of encoders and is used to map images to high-dimensional spaces. The point cloud prediction module generates $N \times 3$ point cloud data from the image depth learned by the network through a fully connected network. The process of periodic encoding and decoding can make better use of global and local information. We found that the point cloud data obtained by lidar scanning were arranged in line. Based on this feature, we can observe that in the point cloud data of the KITTI data set scanned by the 64-line lidar, the nearest neighbors of each point are on the same line. The simulation of real point cloud data sets can be performed well by interpolation of the points and their nearest neighbors.

Encoder-decoder network in Figure 4 shows the proposed basic network composition; the network is trained to understand the mapping relationship between 2D images and 3D point clouds. In the 2D stage, the network encodes the input image into the latent space for feature extraction. The irregularity of the point cloud causes the 3D CNN to not exhibit good performance on the 3D point cloud. The fully connected decoder performs well at reading potential vectors to complete the point set prediction.

Evaluation Indicators

In the point cloud reconstruction network, we use an N-layer convolution machine to extract and encode information from the input segmented target image. In the decoding process, we use a fully connected network to decode the extracted high-dimensional information and set $N \times 3$ neurons in the output

layer to make their output results correspond to the coordinates of the point cloud. Owing to the disorder of the point cloud, we cannot use the reconstruction loss and latent loss commonly used in 2D images in the point cloud reconstruction problem. We use the chamfer distance (CD) as the loss function of our point cloud generation network.

CD considers the average of the point-to-point closest distances between the two sets of point clouds as the evaluation result. In the process of finding the closest points for two sets of point clouds, there may be multiple points corresponding to one point. When this phenomenon occurs, only one set of point clouds is used as the search item and the other set is used as the GT, which cannot accurately express the result of matching between points. CD uses two sets of point clouds to find the points closest to each other, and the average value is used to solve this problem.

$$CD(S_1, S_2) = \frac{1}{|S_1|} \sum_{x \in S_1} \min_{y \in S_2} \|x - y\| + \frac{1}{|S_2|} \sum_{y \in S_2} \min_{x \in S_1} \|x - y\| \quad (1)$$

where S_1 and S_2 are the generated point cloud and GT, respectively. x and y are the points in the generated point cloud and the standard point cloud, respectively, and $\|\cdot\|$ is a two-norm operation, $\Phi: S_1 \rightarrow S_2$, and a bijection, the smaller is better.

Materials

Experimental Environment

The experiment was completed on a computer with a Core i9-7920X processor, 11 gigabytes RAM, and GTX 1080 Ti hardware configuration. The program was implemented in the Python (version 3.6) programming language, and the deep learning platform is TensorFlow (version 1.12.0).

Experimental Data

The open-source database KITTI is currently one of the most important test sets in the field of autonomous driving. KITTI is mainly used for image processing technology in the field of autonomous driving and in autonomous driving perception and prediction. Pix3D (Sun *et al.* 2018) entailed 3D shape modeling from a single image, which is similar to our goal of predicting point cloud data from a single image. KITTI provides a large number of real scenes, which can be used to better measure and test the performance of algorithms. The experimental data in this work were obtained from the 375 \times 1242 charge coupled device (CCD) image and large-scale point cloud data in the object detection task data set in KITTI as well as the label file matching the labeled data. The label file can be used to easily associate the CCD image data of a particular vehicle target with 3D point cloud data. In the previous literature, training point cloud reconstruction networks used nonreal data sets, such as ShapeNet, ModelNet, and PartNet. Compared with the point cloud data obtained by modeling, the obvious disadvantage of the KITTI data set obtained using multi-line lidar scanning is that the point cloud data of the target are incomplete. We make and choose the corresponding CCD images and point cloud data according to the following principles. (1) The vehicles in the CCD image are incomplete, and some of them are obscured by more than 1/3. (2) The point cloud data of the target in the data set cannot be too sparse. Therefore, we choose the point cloud data with more than 400 points. Thus, we established our experimental data set.

Figure 5 shows the visualization of the data set. The segmentation result is obtained by passing the first line of the image through the Mask R-CNN network, which can remove the surrounding area that is not of interest. Simultaneously, to ensure the segmentation effect of Mask R-CNN, we try to ensure that the target vehicle in the produced image is in the middle of the image.

Result and Discussion

We found that the 2D image data set in KITTI is smaller than most of the current 2D data sets, and there is no available GT. To complete the task of 2D image instance segmentation in the first stage more optimally, we did not use the 2D images in the KITTI for segmentation using the Mask R-CNN network, but used the prevalent COCO data set for the instance segmentation training of the network. During the test, we found that the trained Mask-RCNN network can complete the segmentation task of the 2D images of the KITTI data set. In the segmentation of the 3D point cloud, we used the position and bounding box provided by the data set to extract the true 3D information of the target from the disorderly point cloud data.

The experimental results obtained after training the network are shown in Figure 6c, and the CD is 0.0273. It can be seen that the distribution of the predicted point cloud data is uneven and concentrated in a certain area, especially in the category of “people”, because local information has a greater impact on the results. In fact, by continuously integrating global and local information, the density of the point set can be redistributed (Figure 6d). It can also be seen from Figure 6d that the reconstruction effect is significantly better than before, the 3D structure is more stable, and its CD is 0.0285.

Conclusion

It is difficult to train a network using real data sets because the data content is too complex. In the case of 2D images, weather and light will affect the content of the acquired images, and the target is often blocked. Regarding 3D data, point clouds are often sparse and uneven; particularly, in the case of autonomous driving, it is impossible to obtain complete point cloud information. Therefore, training with real data sets is a substantial challenge, and the 3D reconstruction index in such a case will inevitably be high. However, in real scenarios, such as autonomous driving, the reconstruction ability of our model is higher than that of previous models.

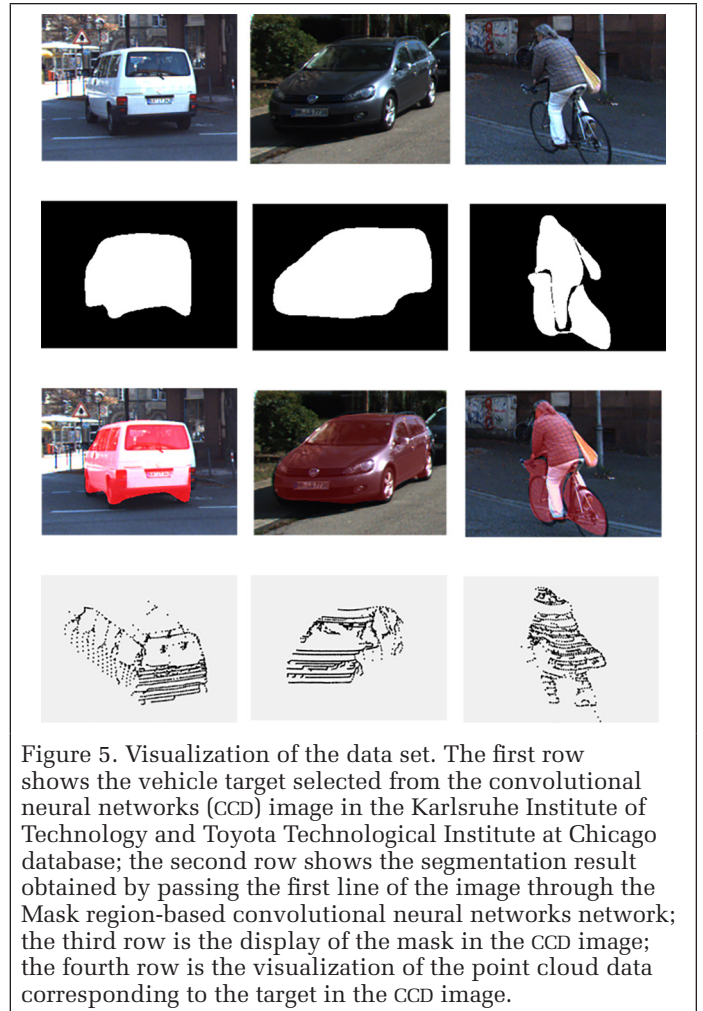


Figure 5. Visualization of the data set. The first row shows the vehicle target selected from the convolutional neural networks (CCD) image in the Karlsruhe Institute of Technology and Toyota Technological Institute at Chicago database; the second row shows the segmentation result obtained by passing the first line of the image through the Mask region-based convolutional neural networks network; the third row is the display of the mask in the CCD image; the fourth row is the visualization of the point cloud data corresponding to the target in the CCD image.

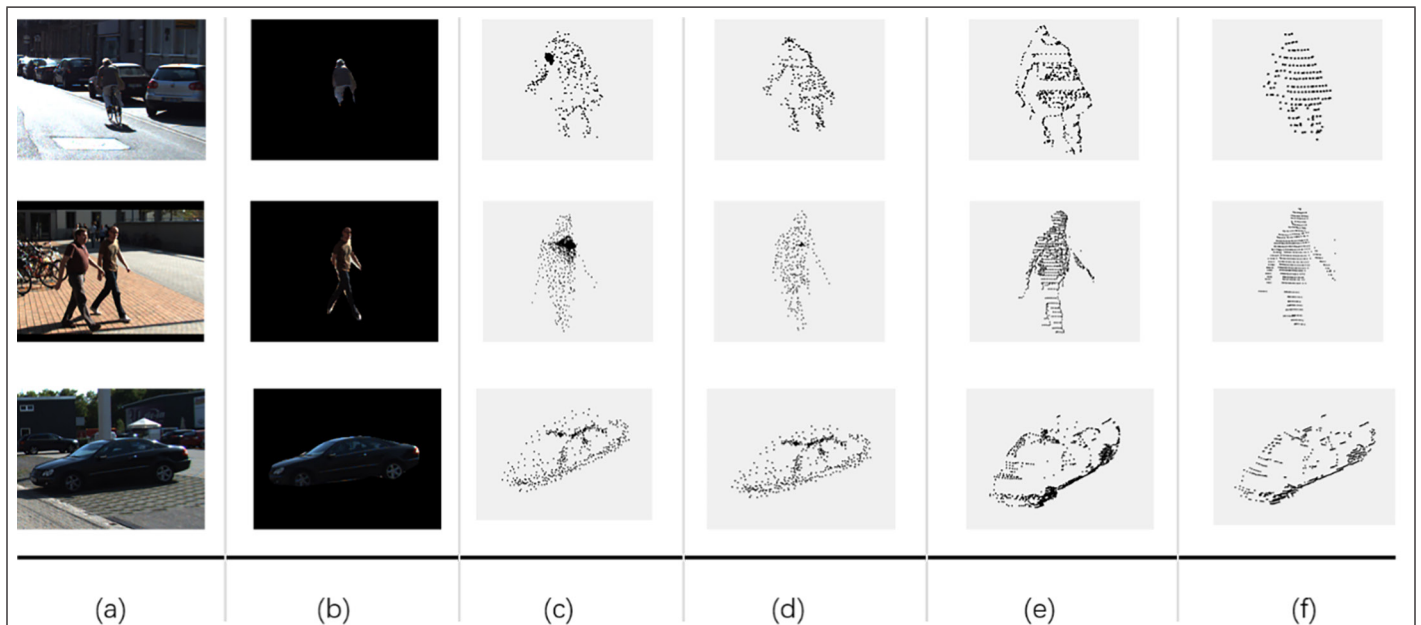


Figure 6. Experimental results. (a) The input image; (b) the segmented object of interest; (c) the visualization of the reconstructed point cloud data; (d) the visualization result of the reconstructed point cloud after improvement with integrating global and local information; (e) the ground truth; (f) raw data in the Karlsruhe Institute of Technology and Toyota Technological Institute at Chicago database, which has not been up-sampled.

Acknowledgments

This work is supported by the National Key R&D Program of China under Grant No. 2016YFE0200700; the National Natural Science Foundation of China under Grants No. 61934003, No. 61627820, and No. 62090054; major scientific and technological program of Jilin Province under Grants No. 20200501007GX; industrial technology research and development of Jilin Province Development and Reform Commission No. 2019C054-1 and No. 2020C019-2.

References

- Berger, M., A. Tagliasacchi, L. M. Seversky, P. Alliez, J. A. Levine, A. Sharf and C. T. Silva. 2014. State of the art in surface reconstruction from point clouds. Pages 161–185 in *Proceedings Eurographics*, held in Strasbourg, France.
- Chang, A. X., T. Funkhouser, L. Guibas, P. Hanrahan, Q. Huang, Z. Li, S. Savarese, M. Savva, S. Song, H. Su, J. Xiao, L. Yi and F. Yu. 2015. ShapeNet: An information-rich 3D model repository. ArXiv: abs/1512.03012.
- Fan, H., H. Su and L. Guibas. 2017. A point set generation network for 3D object reconstruction from a single image. Pages 2463–2471 in *Proceedings 2017 IEEE Conference on Computer Vision and Pattern Recognition (CVPR)*, held in Honolulu, Hawaii.
- Geiger, A., P. Lenz, C. Stiller and R. Urtasun. 2013. Vision meets robotics: The KITTI dataset. *The International Journal of Robotics Research* 32:1231–1237.
- Girshick, R. B. 2015. Fast R-CNN. Pages 1440–1448 in *Proceedings 2015 IEEE International Conference on Computer Vision (ICCV)*, held in Santiago, Chile.
- Girshick, R. B., J. Donahue, T. Darrell and J. Malik. 2014. Rich feature hierarchies for accurate object detection and semantic segmentation. Pages 580–587 in *Proceedings 2014 IEEE Conference on Computer Vision and Pattern Recognition*, held in Columbus, Ohio.
- He, K., G. Gkioxari, P. Dollár and R. B. Girshick. 2017. Mask R-CNN. Pages 2980–2988 in *Proceedings 2017 IEEE International Conference on Computer Vision (ICCV)*, held in Venice, Italy.
- Huang, Z., L. Huang, Y. Gong, C. Huang and X. Wang. 2019. Mask scoring R-CNN. Pages 6402–6411 in *Proceedings 2019 IEEE/CVF Conference on Computer Vision and Pattern Recognition (CVPR)*, held in Long Beach, Calif. doi:10.1109/CVPR.2019.00657.
- Jancosek, M. and T. Pajdla. 2011. Multi-view reconstruction preserving weakly-supported surfaces. Pages 3121–3128 in *Proceedings 2011 IEEE Conference on Computer Vision and Pattern Recognition (CVPR)*, held in Providence, R.I.
- Lin, T. Y., M. Maire, S. Belongie, J. Hays and C. L. Zitnick. 2014. Microsoft COCO: Common objects in context. Pages 740–755 in *Proceedings European Conference on Computer Vision*. Edited by D. Fleet, T. Pajdla, B. Schiele, and T. Tuytelaars. Cham, Switzerland: Springer International Publishing.
- Long, J., E. Shelhamer and T. Darrell. 2015. Fully convolutional networks for semantic segmentation. Pages 3431–3440 in *Proceedings 2015 IEEE Conference on Computer Vision and Pattern Recognition (CVPR)*, held in Boston, Mass.
- Mandikal, P., K. L. Navaneet, M. Agarwal and R. Venkatesh Babu. 2018. 3D-LMNet: Latent embedding matching for accurate and diverse 3D point cloud reconstruction from a single image. Pages 1–19 in *Proceedings British Machine Vision Conference (BMVC)*, held in Newcastle Upon Tyne, England.
- Mandikal, P. and R. Venkatesh Babu. 2019. Dense 3D point cloud reconstruction using a deep pyramid network. Pages 1052–1060 in *Proceedings 2019 IEEE Winter Conference on Applications of Computer Vision (WACV)*, held in Waikoloa Village, Hawaii.
- Ren, S., K. He, R. B. Girshick and J. Sun. 2015. Faster R-CNN: Towards real-time object detection with region proposal networks. *IEEE Transactions on Pattern Analysis and Machine Intelligence* 39:1137–1149.
- Rusu, R. B. and S. Cousins. 2011. 3D is here: Point cloud library (PCL). Pages 1–4 in *Proceedings 2011 IEEE International Conference on Robotics and Automation*, held in Shanghai, China.
- Schönberger, J. L. and J. Frahm. 2016. Structure-from-motion revisited. Pages 4104–4113 in *Proceedings 2016 IEEE Conference on Computer Vision and Pattern Recognition (CVPR)*, held in Las Vegas, Nev.
- Shao, Z. F., L. Wang, Z. Wang and J. Deng. 2019. Remote sensing image super-resolution using sparse representation and coupled sparse autoencoder. *IEEE Journal of Selected Topics in Applied Earth Observations and Remote Sensing* 12:2663–2674.
- Sipiran, I., R. Gregor and T. Schreck. 2014. Approximate symmetry detection in partial 3D meshes. *Computer Graphics Forum* 33:131–140.
- Sun, R., Y. Gao, Z. Fang, A. Wang and C. Zhong. 2019. SSL-Net: Point-cloud generation network with self-supervised learning. *IEEE Access* 7:82206–82217.
- Sun, X., J. Wu, X. Zhang, Z. Zhang, C. Zhang, T. Xue, J. Tenenbaum and W. Freeman. 2018. Pix3D: Dataset and methods for single-image 3D shape modeling. Pages 2974–2983 in *Proceedings IEEE/CVF Conference on Computer Vision and Pattern Recognition*, held in Salt Lake City, Utah.
- Sung, M., V. G. Kim, R. Angst and L. Guibas. 2015. Data-driven structural priors for shape completion. *ACM Transactions on Graphics*, 34(175):1–175:11.
- Vishwanath, K., A. Vahdat, K. Yocum and D. Gupta. 2009. ModelNet: Towards a datacenter emulation environment. Pages 81–82 in *Proceedings 2009 IEEE Ninth International Conference on Peer-to-Peer Computing*, held in Seattle, Wash.
- Yu, F., K. Liu, Y. Zhang, C. Zhu and K. Xu. 2019. PartNet: A recursive part decomposition network for fine-grained and hierarchical shape segmentation. Pages 9483–9492 in *Proceedings 2019 IEEE/CVF Conference on Computer Vision and Pattern Recognition (CVPR)*, held in Long Beach, Calif.
- Yuan, W., T. Khot, D. Held, C. Mertz and M. Hebert. 2018. PCN: Point completion network. Pages 728–737 in *Proceedings International Conference on 3D Vision (3DV)*, held in Verona, Italy.
- Zhai, R., X. Li, Z. Wang, S. Guo, S. Hou, Y. Hou, F. Gao and J. Song. 2020. Point cloud classification model based on a dual-input deep network framework. *IEEE Access* 8(2020):55991–55999.

A Unified Framework of Bundle Adjustment and Feature Matching for High-Resolution Satellite Images

Xiao Ling, Xu Huang, and Rongjun Qin

Abstract

Bundle adjustment (BA) is a technique for refining sensor orientations of satellite images, while adjustment accuracy is correlated with feature matching results. Feature matching often contains high uncertainties in weak/repeat textures, while BA results are helpful in reducing these uncertainties. To compute more accurate orientations, this article incorporates BA and feature matching in a unified framework and formulates the union as the optimization of a global energy function so that the solutions of the BA and feature matching are constrained with each other. To avoid a degeneracy in the optimization, we propose a comprised solution by breaking the optimization of the global energy function into two-step suboptimizations and compute the local minimums of each suboptimization in an incremental manner. Experiments on multi-view high-resolution satellite images show that our proposed method outperforms state-of-the-art orientation techniques with or without accurate least-squares matching.

Introduction

Georeferencing of multi-view satellite images is a necessary step to geometrically align these images in a common coordinate system (Qin 2016) and to allow subsequent applications in, for example, digital surface model (DSM) generation (Di Rita *et al.* 2017; Qin 2016, 2017, 2019), change detection (Zhuang *et al.* 2018), data fusion (Mohammadi *et al.* 2019), and so on. Typically, the georeferencing of multi-view images follows two major steps: (1) feature point matching across different images and (2) bundle adjustment (BA), which aligns the positions and attitudes of the cameras so that the optical rays from corresponding pixels intersect at the same ground point in the object space. However, the accuracy of BA relies highly on the quality of the feature matching results (e.g., point localization accuracy and distributions). Many of the existing feature point extraction methods, such as the scale-invariant feature transform (SIFT) (Lowe 2004) and Speeded Up Robust Features (Bay *et al.* 2006) operators, utilize the scale space by locating the interest point in a reduced resolution, and the descriptors of these operators explore the gradient of local patches and do not accommodate geometric distortions of the local patches (affine or perspective), which often lead to reduced location and matching accuracy of the

points. Since the standard BA takes the matched feature points as observations and optimizes only the poses, we hypothesize that simultaneously optimizing the pose and the location of the matched points may improve georeferencing accuracy.

There have been several attempts (Dos Santos *et al.* 2016; Ling *et al.* 2016; Noh and Howat 2018; Zhou *et al.* 2018) to combine feature matching and BA for more accurate orientations. All of these works follow a coarse-to-fine strategy: they used either coarse BA results (from a few robust initial matches) or original sensor model parameters to reduce the searching space of each feature point with epipolar constraints, then found a large number of robust matches in the reduced searching space for the accurate BA. However, these methods did not fully utilize the BA results for the purpose of subpixel-level matching. Their epipolar constraints reduced the searching space only at the integer pixel level, thus resulting in only pixel-level matches. To achieve more accurate matching results, the least-squares matching (LSM) technique (Hu and Wu 2017) is used to find subpixel-level matches by estimating the best fit between matching windows of corresponding pixels. However, given the nonlinear and nonquadratic nature of the LSM formation, the convergence of the LSM is often uncontrolled, especially in weak-textured or nonlinear radiometric distortion regions (Gruen 2012).

To further improve orientation accuracies, we combine feature matching and BA in a unified framework where the solutions of feature matching and BA are mutually constrained. The rationale here is (1) to improve point localization/matching accuracy and (2) to improve 2D and 3D consistency through the constraints casted by the use of an approximately adjusted rational function model and to reduce the chances of divergence in LSM. The core algorithm formulates the combination into the optimization of a global energy function where feature matching and BA are formulated as two terms in the energy function. However, the solutions of feature matching and BA have some redundant variables that may bring a degeneracy in the optimization. We therefore propose a comprised solution by breaking the optimization into suboptimizations and, respectively, assigning the redundant variables into different suboptimizations so that the variables in the suboptimizations are independent. Finally, the local minimums of the suboptimizations are computed in an incremental manner. Experiments on a multi-view satellite data set show that our approach is capable of computing more accurate orientation results with more accurate matches when compared with the state-of-the-art orientation techniques with or without LSM points.

Xiao Ling is with the Department of Civil, Environmental and Geodetic Engineering, The Ohio State University.

Xu Huang is with the Department of Civil, Environmental and Geodetic Engineering, The Ohio State University.

Rongjun Qin is with the Department of Civil, Environmental and Geodetic Engineering, and the Department of Electrical and Computer Engineering, and Translational Data Analytics Institute, The Ohio State University, 218B Bolz Hall, 2036 Neil Avenue, Columbus, OH 43210 (qin.324@osu.edu)..

Contributed by Hongyan Zhang, March 28, 2020 (sent for review May 19, 2020; reviewed by Wanshou Jiang, Wei Yao).

Photogrammetric Engineering & Remote Sensing
Vol. 87, No. 7, July 2021, pp. 485–490.
0099-1112/21/485–490

© 2021 American Society for Photogrammetry
and Remote Sensing
doi: 10.14358/PERS.87.7.485

Methodology

Problem Formulation

Given multi-view high-resolution satellite images i , corresponding generic sensor models (rational polynomial coefficients [RPC] [Grodecki and Dial 2003]) R , and a series of multi-view matches $\mathbf{P} = \{\mathbf{P}_i^j\}$ with \mathbf{P}_i^j being an image matching point of the object space point i on the image j , our goal is to estimate accurate BA results with corrected matches. In general, we consider the geometric constraints of the forward and backward projections (also called reprojections) in the BA and the photo-consistency constraints in the LSM and formulate these two constraints as two terms in a global energy function, as shown in Equation 1. The first term, e_{proj} , formulates the reprojection error, which is the squared sum of distances between the corrected feature matching points and the reprojection points, and the second term, e_{LSM} , is the LSM objective term, which measures the similarities in intensity of corresponding matching windows against the linear radiometric distortions. These two terms are mutually constrained since the reprojection error e_{proj} uses measurement from the LSM $(\Delta x_i^j, \Delta y_i^j)^T$ and the LSM error term e_{LSM} takes the refined parameters from the reprojection error term $(x_i^b, y_i^b)^T$:

(Equation 1, see below)

where E is the global energy function; $\mathbf{x}_0, \mathbf{y}_0$ are vectors of RPC biases of all satellite images in column and row directions; $\Delta \mathbf{x}, \Delta \mathbf{y}$ are vectors of image coordinate corrections of the given feature matching points; $\mathbf{N}, \mathbf{L}, \mathbf{H}$ are vectors of object space point coordinates of all matches in latitude, longitude, and height directions; $\mathbf{h}_0, \mathbf{h}_1$ are vectors of radiometric distortion corrections that are used to correct the linear intensity distortions among multi-view matches; i is an object space point; \mathbf{S}_i is a set of images that contain the matches of i ; j is an image in \mathbf{S}_i ; $\mathbf{R}_j = (R_{j,x}, R_{j,y})^T$ is the RPC model of the image j in column and row directions; $(N_i, L_i, H_i)^T$ is ground coordinates (latitude, longitude, and height) of the object space point i ; $S_{s,j}, O_{s,j}, S_{l,j}, O_{l,j}$ are default RPC normalization parameters of the image j in the column and row directions; x_i^b, y_i^b are RPC biases of the image j in the column and the row directions; $\bar{\mathbf{R}}_j(N_i, L_i, H_i) - (x_i^b, y_i^b)^T$ is the biased reprojection points of the object space point i on the image j ; $\Delta x_i^j, \Delta y_i^j$ are image coordinate corrections of \mathbf{P}_i^j ; and b is a reference image so that the matches in other images in \mathbf{S}_i must satisfy the photo-consistency with b . Therefore, the image coordinate corrections $\Delta x_i^b, \Delta y_i^b$ can be set as 0. In this article, we compute zero-based normalized cross-correlation scores for any two corresponding pixels in the matches, accumulate the scores that are related to the same image, and find an image with the highest accumulation results as the reference image; $h_{i,0}^j, h_{i,1}^j$ are radiometric distortion corrections of \mathbf{P}_i^j , and $\mathbf{I}_{j,w}$ is a matching window on the image j with the window size w .

Often, on-orbit geometric calibration has compensated for high-order systematic errors; thus, orientation errors can be corrected by constant biases in the image space as long as the corresponding satellite orbit is no longer than 500 km (Fraser and Hanley 2005). Therefore, we adopt the constant RPC biases in Equation 1. We also adopt the LSM model (Hu and Wu 2017) with eight parameters (two radiometric parameters and six geometric parameters) to correct image coordinates of matches. Thus, the global energy function in Equation 1 can be minimized through standard Newton-Raphson method, as shown in Equation 2. The

first two equations are derived from the geometric term, and the third equation is derived from the photo-consistency term:

$$\begin{aligned} f_y^{i,j} &= \frac{y_i^j + \Delta y_i^j + y_0^j - O_{l,j}}{S_{l,j}} - R_{j,y}(N_i, L_i, H_i) & j \in \mathbf{S}_i \\ f_x^{i,j} &= \frac{x_i^j + \Delta x_i^j + x_0^j - O_{s,j}}{S_{s,j}} - R_{j,x}(N_i, L_i, H_i) \\ f_{c,\delta}^{i,j} &= \mathbf{I}_b(\mathbf{P}_i^b + \delta) - h_{i,0}^j - h_{i,1}^j \mathbf{I}_j(\mathbf{P}_i^j + \delta + (\Delta x_i^j, \Delta y_i^j)^T) & j, b \in \mathbf{S}_i \\ & & j \neq b \end{aligned} \quad (2)$$

$$\begin{aligned} \Delta y_i^j &= b0_i^j + b1_i^j \cdot x_i^b + b2_i^j \cdot y_i^b \\ \Delta x_i^j &= a0_i^j + a1_i^j \cdot x_i^b + a2_i^j \cdot y_i^b \\ \Delta x_i^b &= \Delta y_i^b = 0 \\ \mathbf{P}_i^b + \delta &\in \mathbf{I}_{b,w}(\mathbf{P}_i^b) \quad \mathbf{P}_i^j + \delta \in \mathbf{I}_{j,w}(\mathbf{P}_i^j) \end{aligned}$$

where $f_y^{i,j}, f_x^{i,j}$ are functions to measure the image location differences between the corrected image point of \mathbf{P}_i^j and its corresponding reprojection point; x_i^j, y_i^j are column and row coordinates of \mathbf{P}_i^j in the image space; $\mathbf{P}_i^j + \delta$ is a pixel in the matching window of \mathbf{P}_i^j with δ being an offset vector to \mathbf{P}_i^j ; $f_{c,\delta}^{i,j}$ is a function to measure the photo-consistency between $\mathbf{P}_i^b + \delta$ and $\mathbf{P}_i^j + \delta$; x_i^b, y_i^b are column and row coordinates of \mathbf{P}_i^b in the reference image b ; and $a0_i^j, a1_i^j, a2_i^j, b0_i^j, b1_i^j, b2_i^j$ are affine parameters to correct image coordinates of \mathbf{P}_i^j . For each matching point \mathbf{P}_i^j , the number of geometric equations $f_x^{i,j}$ and $f_y^{i,j}$ is only one, while the number of the photo-consistency equations $f_{c,\delta}^{i,j}$ are in total w^2 . Therefore, it is better to assign higher weights to $f_x^{i,j}, f_y^{i,j}$ during the optimization so that the geometric term and the photo-consistency term can make comparable contributions to the final solution. The detailed weight strategy is introduced next.

Solution

Equation 2 is nonlinear, so it is hard to directly compute the optimal solution. Therefore, we first estimate the initial values of all unknowns $\mathbf{x}_0, \mathbf{y}_0, \mathbf{N}, \mathbf{L}, \mathbf{H}, \Delta \mathbf{x}, \Delta \mathbf{y}, \mathbf{h}_0, \mathbf{h}_1$ and then linearize Equation 2 by the first-order Taylor expansion. The initial values of $\mathbf{x}_0, \mathbf{y}_0$ are set as 0; the initial values of $\mathbf{N}, \mathbf{L}, \mathbf{H}$ are computed by triangulating the given matches using the original RPC parameters; and the initial values of the image coordinate correction parameters $\{a0_i^j, a1_i^j, a2_i^j\}$ and $\{b0_i^j, b1_i^j, b2_i^j\}$ are, respectively, set as $\{-x_i^b, 1, 0\}$ and $\{-y_i^b, 1, 0\}$. We normalize the intensities in all matching windows so that the initial values of $\mathbf{h}_0, \mathbf{h}_1$ can be set as 0 and 1. Given these initial values, the linearization of Equation 2 is as follows:

(Equation 3, see next page)

where $(f_y^{i,j})_0, (f_x^{i,j})_0$, and $(f_{c,\delta}^{i,j})_0$ are initial values of functions $f_y^{i,j}, f_x^{i,j}$, and $f_{c,\delta}^{i,j}$; $V_x^{i,j}, V_y^{i,j}$ are geometric residual errors of the image locations of \mathbf{P}_i^j ; $V_{c,\delta}^{i,j}$ is the intensity residual error; and $dy_0^j, dx_0^j, da0_i^j, da1_i^j, da2_i^j, db0_i^j, db1_i^j, db2_i^j, dh0_i^j, dh1_i^j, dN_i, dL_i$, and dH_i are corrections of all unknowns in the global energy function.

However, there exist some redundancies between the RPC biases x_0^j, y_0^j and the image coordinate corrections $a0_i^j, b0_i^j$, which may make the residual error equations in Equation 3 degenerate. Moreover, the large quantities of the image coordinate corrections also bring great challenges in efficient computation. Therefore, we assign the RPC biases and the image coordinate corrections in different computation tasks and propose a comprised solution by breaking the optimization

$$\begin{aligned} \min E(x_0, y_0, N, L, H, \Delta x, \Delta y, h_0, h_1) &= \sum_i e_{\text{proj}} + e_{\text{LSM}} = \sum_i \left(\sum_{j \in \mathbf{S}_i} \left\| \bar{\mathbf{R}}_j(N_i, L_i, H_i) - (x_i^j, y_i^j)^T - (\mathbf{P}_i^j + (\Delta x_i^j, \Delta y_i^j)^T) \right\|_2 + \sum_{j, b \in \mathbf{S}_i, j \neq b} \left\| \mathbf{I}_{b,w}(\mathbf{P}_i^b) - h_{i,0}^j - h_{i,1}^j \mathbf{I}_{j,w}(\mathbf{P}_i^j + (\Delta x_i^j, \Delta y_i^j)^T) \right\|_2 \right) \\ \bar{\mathbf{R}}_j(N_i, L_i, H_i) &= (S_{s,j} \cdot R_{j,x}(N_i, L_i, H_i) + O_{s,j}, S_{l,j} \cdot R_{j,y}(N_i, L_i, H_i) + O_{l,j})^T \\ \Delta x_i^b &= \Delta y_i^b = 0 \end{aligned} \quad (1)$$

of the global energy function in Equation 1 into two kinds of suboptimizations in an incremental manner: (1) the suboptimization of RPC biases and object space point coordinates without considering image coordinate corrections or radiometric distortion corrections and (2) the suboptimization of image coordinate corrections, radiometric distortion corrections, and object space point coordinates with refined RPC biases from the first suboptimization.

In the first suboptimization, the image coordinate corrections and radiometric distortion corrections are fixed as the initial values, while only the RPC biases and the object space point coordinates are considered. Therefore, Equation 3 can be simplified by removing the terms of image coordinate corrections and radiometric distortion corrections in $V_y^{i,j}$, $V_x^{i,j}$ and removing the entire function of $V_{c,\delta}^{i,j}$ as follows:

$$\begin{aligned} V_y^{i,j} &= \frac{\partial(f_y^{i,j})_0}{\partial y_0^j} dy_0^j + \frac{\partial(f_y^{i,j})_0}{\partial N_i} dN_i + \frac{\partial(f_y^{i,j})_0}{\partial L_i} dL_i + \frac{\partial(f_y^{i,j})_0}{\partial H_i} dH_i - (f_y^{i,j})_0 \\ V_x^{i,j} &= \frac{\partial(f_x^{i,j})_0}{\partial x_0^j} dx_0^j + \frac{\partial(f_x^{i,j})_0}{\partial N_i} dN_i + \frac{\partial(f_x^{i,j})_0}{\partial L_i} dL_i + \frac{\partial(f_x^{i,j})_0}{\partial H_i} dH_i - (f_x^{i,j})_0 \end{aligned} \quad (4)$$

Equation 4 is similar to the traditional BA model. Least-squares or gradient descent methods (Zheng and Zhang 2016) can be used to compute the optimal solution of Equation 4. The RPC biases are then used to refine the RPC parameters of each image, and the refined RPCs are used in the second suboptimizations to provide geometric guidance for more accurate matching. Given the refined RPC parameters, the second suboptimizations of Equation 3 can be simplified as follows:

(Equation 5, *see below*)

The initial values of the ground coordinates \mathbf{N} , \mathbf{L} , \mathbf{H} can be updated by the refined RPCs in the first suboptimization. Since RPC bias corrections were not considered in Equation 5, the second suboptimization can be formulated as the individual optimizations of each match. However, the solution of Equation 5 depends partly on the geometric accuracies of the refined RPCs. High-accuracy RPCs can provide accurate geometric guidance for the feature matching and vice versa. To compute robust solutions of Equation 5, we formulate the geometric accuracies of the refined RPCs as the reprojection errors of the matches and define the root-mean-square error (RMSE) of reprojection errors of the matches as weights for the geometric

terms $V_y^{i,j}$ and $V_x^{i,j}$ in Equation 5. Higher reprojection errors correspond to lower weights and vice versa. To ensure that the geometric terms $V_y^{i,j}$, $V_x^{i,j}$ make comparable contributions with the photo-consistency term $V_{c,\delta}^{i,j}$ in the solution of Equation 5, we consider both the reprojection errors and the matching window sizes in the weight strategy as follows:

$$\begin{aligned} W_{\text{reprj}} &= W_{\text{max}} \cdot \exp(-\varepsilon^2/\sigma) \\ W_{\text{max}} &= P \cdot w^2 \cdot \frac{n-1}{2} \\ \varepsilon &= \sqrt{\sum_j^n (d_{j,x}^2 + d_{j,y}^2) / (n-1.5)} \end{aligned} \quad (6)$$

where W_{reprj} is a weight of $V_y^{i,j}$, $V_x^{i,j}$, depending on the RMSE of reprojection errors and the matching window sizes; ε is the RMSE of reprojection errors; n is the viewing ray number of the matches; and $d_{j,x}$, $d_{j,y}$ are reprojection errors between the matching points and the reprojection points in the column and row directions on the image j . Since each matching point gives two observations and the unknowns of the object space point coordinates are only three, 1.5 was subtracted from the viewing ray number for more robust RMSE evaluation. W_{max} means the maximum weights of $V_y^{i,j}$, $V_x^{i,j}$ in the solution. Since the number of the photo-consistency terms $V_{c,\delta}^{i,j}$ of each match is $w^2 \cdot (n-1)/2$ times larger than the number of the geometric terms, W_{max} is scaled by $w^2 \cdot (n-1)/2$ to ensure comparable contributions of the geometric terms and the photo-consistency terms in the solution of Equation 5. P is a factor that controls the maximum weights in the solution, which is empirically set as 0.5 in our experiments. σ is a factor that controls the impact of reprojection errors on the weights of the geometric terms. σ is set as two pixels in our experiments so that large reprojection errors (larger than two pixels) will produce negligible weights for the geometric terms. Therefore, the uncertainties in the refined RPCs have only negligible impacts on the matches correction process.

However, too small weights (close to zero) may make the error equations in Equation 5 degenerate; thus, we also add a virtual ground control point (VGCP) constraint by setting the refined object space point in the first suboptimizations as VGCP as follows:

$$\begin{aligned} dlat_i &= 0 \quad dlon_i = 0 \quad dhe_i = 0 \\ W_{\text{VGCP}} &= W_{\text{max}} - W_{\text{reprj}} \end{aligned} \quad (7)$$

$$\begin{aligned} V_y^{i,j} &= \frac{\partial(f_y^{i,j})_0}{\partial y_0^j} dy_0^j + \frac{\partial(f_y^{i,j})_0}{\partial b0_i^j} db0_i^j + \frac{\partial(f_y^{i,j})_0}{\partial b1_i^j} db1_i^j + \frac{\partial(f_y^{i,j})_0}{\partial b2_i^j} db2_i^j + \frac{\partial(f_y^{i,j})_0}{\partial N_i} dN_i + \frac{\partial(f_y^{i,j})_0}{\partial L_i} dL_i + \frac{\partial(f_y^{i,j})_0}{\partial H_i} dH_i - (f_y^{i,j})_0 \\ V_x^{i,j} &= \frac{\partial(f_x^{i,j})_0}{\partial x_0^j} dx_0^j + \frac{\partial(f_x^{i,j})_0}{\partial a0_i^j} da0_i^j + \frac{\partial(f_x^{i,j})_0}{\partial a1_i^j} da1_i^j + \frac{\partial(f_x^{i,j})_0}{\partial a2_i^j} da2_i^j + \frac{\partial(f_x^{i,j})_0}{\partial N_i} dN_i + \frac{\partial(f_x^{i,j})_0}{\partial L_i} dL_i + \frac{\partial(f_x^{i,j})_0}{\partial H_i} dH_i - (f_x^{i,j})_0 \\ V_{c,\delta}^{i,j} &= \frac{\partial(f_{c,\delta}^{i,j})_0}{\partial h0_i^j} dh0_i^j + \frac{\partial(f_{c,\delta}^{i,j})_0}{\partial h1_i^j} dh1_i^j + \frac{\partial(f_{c,\delta}^{i,j})_0}{\partial a0_i^j} da0_i^j + \frac{\partial(f_{c,\delta}^{i,j})_0}{\partial a1_i^j} da1_i^j + \frac{\partial(f_{c,\delta}^{i,j})_0}{\partial a2_i^j} da2_i^j + \frac{\partial(f_{c,\delta}^{i,j})_0}{\partial b0_i^j} db0_i^j + \frac{\partial(f_{c,\delta}^{i,j})_0}{\partial b1_i^j} db1_i^j + \frac{\partial(f_{c,\delta}^{i,j})_0}{\partial b2_i^j} db2_i^j - (f_{c,\delta}^{i,j})_0 \end{aligned} \quad (3)$$

$j, b \in S_i$

$j \neq b$

$$da0_i^b = da1_i^b = da2_i^b = db0_i^b = db1_i^b = db2_i^b = 0$$

$$\begin{aligned} V_y^{i,j} &= \frac{\partial(f_y^{i,j})_0}{\partial b0_i^j} db0_i^j + \frac{\partial(f_y^{i,j})_0}{\partial N_i} dN_i + \frac{\partial(f_y^{i,j})_0}{\partial L_i} dL_i + \frac{\partial(f_y^{i,j})_0}{\partial H_i} dH_i - (f_y^{i,j})_0 \\ V_x^{i,j} &= \frac{\partial(f_x^{i,j})_0}{\partial a0_i^j} da0_i^j + \frac{\partial(f_x^{i,j})_0}{\partial N_i} dN_i + \frac{\partial(f_x^{i,j})_0}{\partial L_i} dL_i + \frac{\partial(f_x^{i,j})_0}{\partial H_i} dH_i - (f_x^{i,j})_0 \quad j \in S_i \\ V_{c,\delta}^{i,j} &= \frac{\partial(f_{c,\delta}^{i,j})_0}{\partial h0_i^j} dh0_i^j + \frac{\partial(f_{c,\delta}^{i,j})_0}{\partial h1_i^j} dh1_i^j + \frac{\partial(f_{c,\delta}^{i,j})_0}{\partial a0_i^j} da0_i^j + \frac{\partial(f_{c,\delta}^{i,j})_0}{\partial a1_i^j} da1_i^j + \frac{\partial(f_{c,\delta}^{i,j})_0}{\partial a2_i^j} da2_i^j + \frac{\partial(f_{c,\delta}^{i,j})_0}{\partial b0_i^j} db0_i^j + \frac{\partial(f_{c,\delta}^{i,j})_0}{\partial b1_i^j} db1_i^j + \frac{\partial(f_{c,\delta}^{i,j})_0}{\partial b2_i^j} db2_i^j - (f_{c,\delta}^{i,j})_0 \quad \begin{matrix} j, b \in S_i \\ j \neq b \end{matrix} \end{aligned} \quad (5)$$

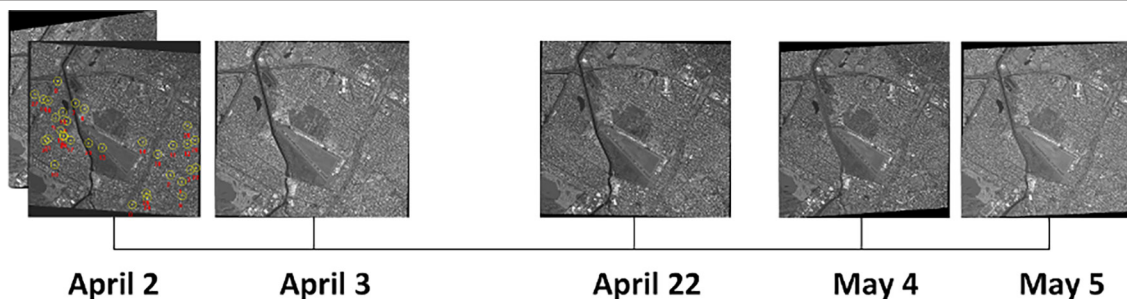


Figure 1. Testing images from the Intelligence Advanced Research Projects Activity Multi-View Stereo benchmark.

where W_{VGCP} is a weight of VGCP constraints. If reprojection errors are small, the geometric terms V_y^{ij} , V_x^{ij} made more contributions to the solution so that the feature matching corrections are geometrically constrained. Otherwise, the VGCP constraints made more contributions in the solution. In an extreme case that $W_{\text{VGCP}} \approx 1$, the solution of the second suboptimizations will degenerate into the traditional LSM model (Hu and Wu 2017).

Next, we compute the solution of the second suboptimizations of each match by combining Equations 5–7. The image coordinate corrections in the solution are then used to correct the matches. Finally, the more accurate matching results and the corresponding refined object space points are used in the first suboptimizations for more accurate BA results.

Experiments

Our proposed method was tested on six WorldView-3 panchromatic images near San Fernando, Argentina, from the Intelligence Advanced Research Projects Activity Multi-View Stereo benchmark data set (Bosch *et al.* 2016). The rationale of using the single-source data sets to test the performance of our methods is twofold. First, our methods can be used for any images that use rational function models and are not sensor specific, and the use of single-source data helps keep the experiments impacted by other factors, such as images with complex distortions. Second, these images can utilize observations with as many as six rays, which is sufficient to test a BA system while remaining manageable in an experimental setup. All images are Level 2 products, which means that high-order systematic errors in the ancillary data have already been compensated for and have been systematically mapped into a standard cartographic map projection based on a prediction of where the satellite was when the image was acquired (NASA 2019). Their sizes are around 13000×12000 and have a greater than 90% overlap ratio. The covering landscape is a typical urban area containing buildings, rivers, trees, and so on. The ground sampling distance of these images is about 0.5 m, and the imaging time of them was from April 2 to May 5, as shown in Figure 1.

To demonstrate the generality and reliability of the proposed method, we utilized a mainstream SIFT feature matching method to obtain initial matches. There are a total of 4210 SIFT matches (see Figure 2), more than 90% of which have the multi-view connectivity (at least three). Given these SIFT matches, our proposed method was compared with two methods: (1) a state-of-the-art orientation method (Ozcanli *et al.* 2014) that initially corrected RPC biases between stereo pairs, then removed mismatching image points/outliers by eliminating the points whose distances to their corresponding epipolar lines are larger than two pixels, and finally computed the BA results in a reference coordinate system of the best stereo pair without any matches corrections (termed BA), and (2) an LSM-based method that followed the same BA technique with the first method. However, the initial matches were corrected by the LSM technique (Hu and Wu 2017) before BA (termed

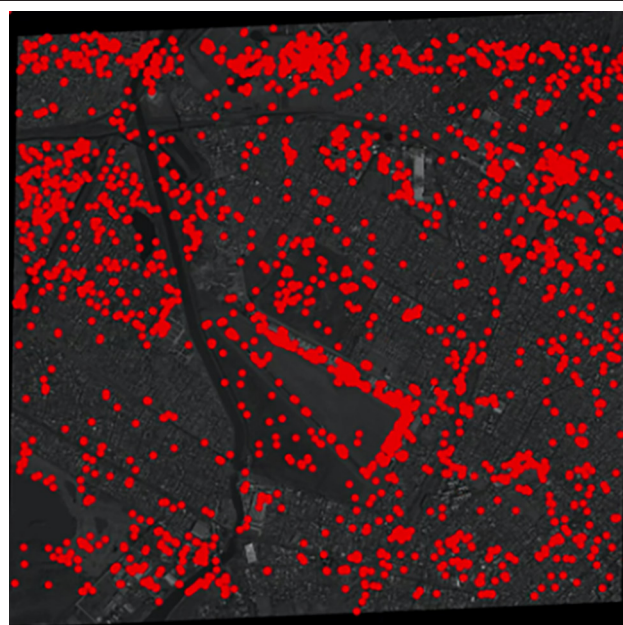


Figure 2. Distribution of scale-invariant feature transform (SIFT) matches on one image. All SIFT points are colored in red.

LSM + BA). For fair comparisons, the outlier elimination technique is also applied in our proposed method after the image coordinate corrections in the second suboptimizations.

Both the proposed method and the LSM + BA need fixed matching windows to correct matches; we therefore utilized a series of different matching windows—{5×5, 7×7, 9×9, 11×11, 13×13, 15×15, 17×17, 19×19, 21×21, 31×31, 41×41}—in the proposed method and the LSM + BA for matches corrections, thus resulting in different BA results. We then compared the results of the three methods from four aspects: (1) the number of diverged matches in the LSM procedure (fewer diverged matches mean a more reliable LSM algorithm); (2) the number of outliers (fewer outliers mean a more robust matching result); (3) average RMSE of reprojection errors for the matches in BA and the corrected matches in LSM + BA and our proposed method (termed internal accuracy), which is used to evaluate the fitting between matches/corrected matches and the BA results; and (4) average RMSE of reprojection errors for the manually selected matches (termed external accuracy), which gives a more comprehensive evaluation to the final orientation accuracies.

Convergence of the LSM

The LSM is able to locate subpixel-level matches, while the convergence of the traditional LSM is often uncontrolled due to weak-textured or nonlinear radiometric distortion regions. To overcome this weakness, the proposed method not only introduces the photo-consistency term, as does the traditional

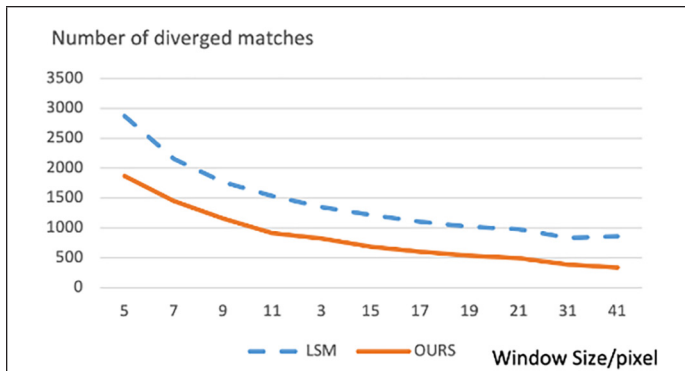


Figure 3. Convergence comparison between traditional least-squares matching and our proposed method. The polylines are the number of diverged matches varying with window size.

LSM method, but also incorporates geometric terms into the LSM procedure to improve its convergence. A series of matching windows were utilized in the traditional LSM and the proposed method, then the numbers of the diverge matches were counted as an evaluation indicator to check the performance of the two methods. The output numbers of diverged matches are shown in Figure 3.

Figure 3 shows that both methods got fewer diverged matches as window size increased since larger windows reduce the matching uncertainties. More specifically, geometric constraints are powerful supplements to photo-consistency constraints and help our proposed method, gaining hundreds of converged matches more than the traditional LSM with different window sizes.

Outlier Comparisons

A series of matching windows were utilized in the LSM + BA and the proposed method for matches corrections, and then outliers in the corrected matches were detected via the following steps: (1) computing 3D coordinates of matches via forward intersection, (2) computing their reprojected image coordinates on all available images via backward projection, (3) computing residual errors on all available images, and (4) counting a view observation as one outlier when the residual error on this view was larger than a predefined threshold (two pixels in our experiments). The outlier numbers of LSM + BA and the proposed method are shown in Figure 4.

Figure 4 shows a fairly intuitive conclusion that the number of outliers is negatively correlated with the size of the windows, as smaller windows tend to feed fewer observations to the LSM. In contrast, our method, due to the employment of the geometric 2D and 3D consistencies, is more robust and shows significantly fewer outliers with all window sizes. This has provided competing advantages over the traditional methods since window size is often a hyperparameter and our method, being less dependent on window size, will yield better robustness and thus can be favorably considered in operations.

Analysis of Internal and External Accuracy

To comprehensively compare BA (with SIFT), LSM + BA, and our proposed method, we analyzed the internal accuracies of matches/corrected matches and the external accuracies of manually selected points. The hyperparameters of the SIFT algorithm remain the same throughout the experiment (the threshold of the ratio of the distance between the best matching keypoint and the distance to the second-best one is set to 0.35, while other parameters are same as in Lowe [2004]). We selected a total of 33 points with the six-ray connectivity for the accuracy checking, as shown in the yellow circles in the satellite image on April 2 in Figure 1. The accuracies of BA,

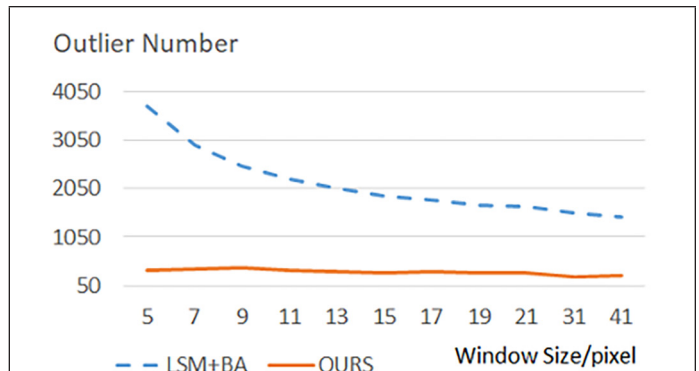
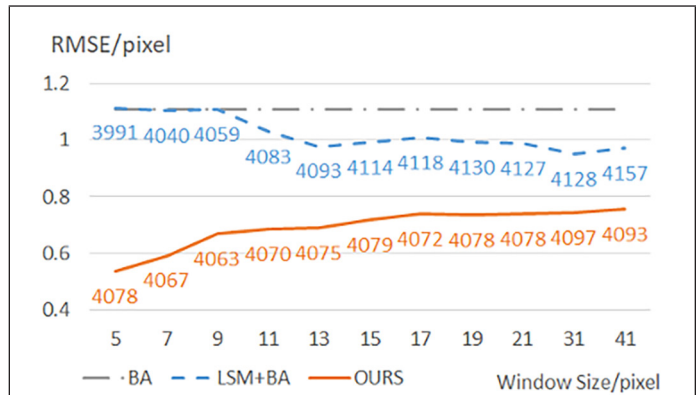
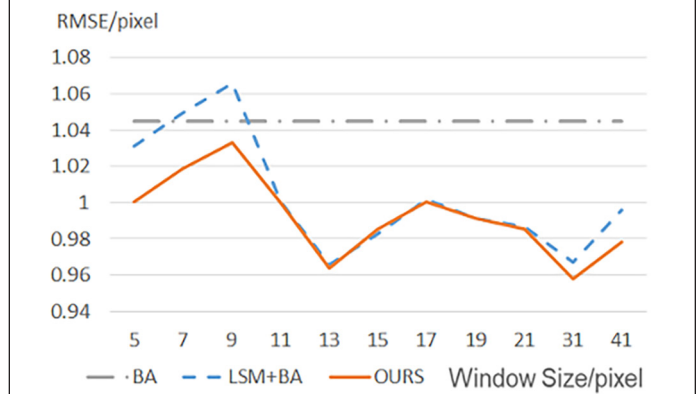


Figure 4. Outlier comparison between the least-squares matching technique before bundle adjustment and our proposed method. The polylines are the number of outliers varying with window size.



(a)



(b)

Figure 5. Accuracy comparisons of the three methods on the scale-invariant feature transform match set. The x-axis represents the different matching window sizes, and the y-axis represents the average root-mean-square error of reprojection errors. The numbers around the polylines are the corresponding number of corrected matches.

LSM + BA, and our proposed method on the SIFT match set are shown in Figure 5.

We have collected 4210 SIFT matches for testing. It was noted that SIFT, with its nature of locating the interest point in the scale space, yields lower positioning accuracy than corner-based operators (Remondino 2006). Thus, the pure BA result on the SIFT match set, as shown in Figure 4, had lower accuracy than the other two methods in terms of both internal and external accuracies, and its RMSE was larger than one pixel.

However, by introducing the LSM to improve the position accuracy for matches, both the LSM + BA method and the proposed method were able to achieve higher internal accuracy, especially subpixel accuracy when the window size was larger than 11×11 pixels. In addition to the photo-consistency constraints, our proposed method also introduces geometric constraints to guide the matching; thus, more matching uncertainties were further reduced compared to the LSM + BA method, and the internal accuracies of our proposed method were always higher than those of the LSM + BA method regardless of matching window sizes. More specifically, our method outperformed the other two methods in terms of internal accuracy regardless of window size.

Figure 5a shows the fittings between the matches/corrected matches and the orientation results, while the orientation results with the highest internal accuracies may not be the best fit for the remaining pixels. Therefore, we manually selected several matches to evaluate the orientation results of different methods, as shown in Figure 5b. The external accuracies of the LSM + BA method sometimes was lower than the pure BA method when the matching window size was small due to high matching uncertainties in the small window size making the LSM unstable. With the increasing matching window sizes, the external accuracies of LSM + BA method surpassed BA by involving more image information. The LSM + BA performed quite closely to our proposed method and was able to achieve subpixel external accuracy when the matching window size was larger than 11×11 pixels. However, our proposed method, integrated with geometric constraint multi-view LSM, was able to achieve the most accurate BA results regardless of window size.

Conclusions

In this article, we propose a unified framework of feature matching and BA for more accurate orientation results. In general, we formulate the union as the optimization of a global energy function and propose a comprised solution by breaking the optimization into two-step sub-optimizations in an incremental manner. Tested on six full-scale high-resolution satellite images, our comparative study demonstrated that compared to SIFT + BA and LSM + BA, our proposed method is able to consistently achieve the best internal and external accuracies on multi-view satellite image data sets, is much less dependent on window size, and is able to improve the convergence in LSM. Although with a relatively marginal improvement, by simultaneously adjusting both the matches and the biases iteratively, our proposed method plays a role in potentially improving standard “feature + BA” solution.

Acknowledgement

This work is supported in part by the Office of Naval Research (ONR Award No. N000141712928 & N000142012141). The authors would like to thank the John Hopkins University Applied Physics Lab and the IARPA multi-view stereo 3D mapping Challenge for making the benchmark dataset available.

References

Bay, H., T. Tuytelaars, and L. Van Gool. 2006. Surf: Speeded up robust features. Pages 404–417 in *European Conference on Computer Vision (ECCV)*, held in City, ST, Country, day–day Month year. Edited by X. Xxxx. Berlin: Springer.

Bosch, M., Z. Kurtz, S. Hagstrom and M. Brown. 2016. A multiple view stereo benchmark for satellite imagery. Pages 1–9 in *IEEE Applied Imagery Pattern Recognition Workshop (AIPR)*, 2016 IEEE, held in City, ST, Country, day–day Month year. Edited by X. Xxxx. New York: IEEE.

Di Rita, M., A. Nascetti and M. Crespi. 2017. Open source tool for DSMs generation from high resolution optical satellite imagery: Development and testing of an OSSIM plug-in. *International Journal of Remote Sensing*, 38(7):1788–1808.

Dos Santos, D. R., M. A. Basso, K. Khoshelham, E. de Oliveira, N. L. Pavan and G. Vosselman. 2016. Mapping indoor spaces by adaptive coarse-to-fine registration of RGB-D data. *IEEE Geoscience and Remote Sensing Letters* 13(2):262–266.

Fraser, C. S. and H. B. Hanley. 2005. Bias-compensated RPCs for sensor orientation of high-resolution satellite imagery. *Photogrammetric Engineering and Remote Sensing* 71(8):909–915.

Grodecki, J. and G. Dial. 2003. Block adjustment of high-resolution satellite images described by rational polynomials. *Photogrammetric Engineering and Remote Sensing* 69(1):59–68.

Gruen, A. 2012. Development and status of image matching in photogrammetry. *The Photogrammetric Record* 27(137):36–57.

Hu, H. and B. Wu. 2017. Bound-constrained multiple-image least-squares matching for multiple-resolution images. *Photogrammetric Engineering and Remote Sensing* 83(10):667–677.

Ling, X., Y. Zhang, J. Xiong, X. Huang and Z. Chen. 2016. An image matching algorithm integrating global SRTM and image segmentation for multi-source satellite imagery. *Remote Sensing* 8(8):1–19.

Lowe, D. G. 2004. Distinctive image features from scale-invariant keypoints. *International Journal of Computer Vision* 60(2):91–110.

Mohammadi, H., F. Samadzadegan and P. Reinartz. 2019. 2D/3D information fusion for building extraction from high-resolution satellite stereo images using kernel graph cuts. *International Journal of Remote Sensing* 40(1):5835–5860.

NASA. 2019. Data Processing Levels. <<https://earthdata.nasa.gov/collaborate/open-data-services-and-software/data-information-policy/data-levels>> Accessed day Month year.

Noh, M. J. and I. M. Howat. 2018. Automatic relative RPC image model bias compensation through hierarchical image matching for improving DEM quality. *ISPRS Journal of Photogrammetry and Remote Sensing* 136:120–133.

Ozcanli, O. C., Y. Dong, J. L. Mundy, H. Webb, R. Hammoud and T. Victor. 2014. Automatic geo-location correction of satellite imagery. Pages 307–314 in *IEEE Conference on Computer Vision and Pattern Recognition Workshops*, held in City, ST, Country, day–day Month year. Edited by X. Xxxx. New York: IEEE.

Qin, R. 2016. RPC Stereo Processor (rsp)—A software package for digital surface model and orthophoto generation from satellite stereo imagery. *ISPRS Annals of Photogrammetry, Remote Sensing and Spatial Information Sciences* 3(1):77–82

Qin, R. 2017. Automated 3D recovery from very high resolution multi-view images: Overview of 3D recovery from multi-view satellite images. Pages 12–16 in *ASPRS Conference (IGTF)*, held in City, ST, Country, day–day Month year. Edited by X. Xxxx. Publisher location: Publisher.

Qin, R. 2019. A critical analysis of satellite stereo pairs for digital surface model generation and a matching quality prediction model. *ISPRS Journal of Photogrammetry and Remote Sensing* 154:139–150.

Remondino, F. 2006. Detectors and descriptors for photogrammetric applications. *International Archives of the Photogrammetry, Remote Sensing and Spatial Information Sciences* 36(3):49–54.

Zheng, M. and Y. Zhang. 2016. DEM-aided bundle adjustment with multisource satellite imagery: ZY-3 and GF-1 in large areas. *IEEE Geoscience and Remote Sensing Letters* 13(6):880–884.

Zhou, P., X. Tang, L. Guo, X. Wang and W. Fan. 2018. DEM generation using Ziyuan-3 mapping satellite imagery without ground control points. *International Journal of Remote Sensing* 39(19):6213–6233.

Zhuang, H., Z. Tan, K. Deng and G. Yao. 2018. Change detection in multispectral images based on multiband structural information. *Remote Sensing Letters* 9(12):1167–1176.

The Spatiotemporal Evolution of Urban Impervious Surface for Chengdu, China

Mujie Li, Zezhong Zheng, Mingcang Zhu, Yue He, Jun Xia, Xueye Chen, Qingjun Peng, Yong He, Xiang Zhang, and Pengshan Li

Abstract

The spatiotemporal evolution of an impervious surface (IS) is significant for urban planning. In this paper, the IS was extracted and its spatiotemporal evolution for the Chengdu urban area was analyzed based on Landsat imagery. Our experimental results indicated that convolutional neural networks achieved the better performance with an overall accuracy of 98.32%, Kappa coefficient of 0.98, and Macro F1 of 98.28%, and the farmland was replaced by IS from 2001 to 2017, and the IS area (ISA) increased by 51.24 km²; that is, the growth rate was up to 13.8% in sixteen years. According to the landscape metrics, the IS expanded and agglomerated into large patches from small fragmented ones. In addition, the gross domestic product change of the secondary industry was similar to the change of ISA between 2001 and 2017. Thus, the spatiotemporal evolution of IS was associated with the economic development of the Chengdu urban area in the past sixteen years.

Mujie Li, Zezhong Zheng, and Jun Xia are with the State Key Laboratory of Water Resources and Hydropower Engineering Science, Wuhan University, Wuhan 430072, China (zezhongzheng@uestc.edu.cn).

Mujie Li, Zezhong Zheng, and Yue He are also with the School of Resources and Environment, University of Electronic Science and Technology of China (UESTC), Chengdu 611731, China; the State Key Laboratory of Remote Sensing Science, jointly sponsored by Beijing Normal University and Aerospace Information Research Institute of Chinese Academy of Sciences, Beijing 100101, China; and the Guangxi Key Laboratory for Spatial Information and Geomatics, Guilin University of Technology, Guilin 541004, China.

Zezhong Zheng and Xueye Chen are with the Key Laboratory of Urban Land Resources Monitoring and Simulation, Ministry of Natural Resources, Shenzhen Research Center of Digital City Engineering, Shenzhen 518040, China (xueye31@163.com).

Mingcang Zhu is with the Department of Natural Resources of Sichuan Province, Chengdu 610072, China.

Qingjun Peng is with the Joint Laboratory of Power Remote Sensing Technology, Electric Power Research Institute, Yunnan Power Grid Company Ltd., Kunming 650217, China (13648716143@139.com).

Yong He is with the Sichuan Research Institute for Ecosystem Restoration & Geohazard Prevention, Chengdu 610081, China.

Xiang Zhang is with the Hubei Provincial Key Lab of Water System Science for Sponge City Construction, Wuhan University, Wuhan 430072, China.

Pengshan Li is with the Chengdu Land Planning and Cadastre Center, Chengdu 610073, China.

Contributed by Zhenfeng Shao, October 31, 2020 (sent for review December 12, 2020; reviewed by Lei Zhang, Md Enamul Huq).

Introduction

Impervious surface area (ISA) is defined as an area composed of a constructed surface that prevents water from infiltrating to the soil (Shao and Liu 2014; Herwindiati *et al.* 2017). With the process of urbanization, the soil in the natural state is covered by impervious or semipervious materials such as concrete, asphalt, glass, plastic, etc., which will lead to the reduction of arable land or green space (Shao *et al.* 2020). Thus, the permeability and storage function of soil for the water is changed. The change of impervious surfaces (IS) has brought profound changes and problems for the environment and landscape structure (Li and Zhou 2017; Piano *et al.* 2017; Shao *et al.* 2019). For example, the exchange of materials and energy between the land surface and the atmosphere is hindered. Thus, the waterlogging disaster happens for the imperviousness change of an urban surface. Many previous studies have also shown the influences of ISA for urban land surface temperature change (Nie *et al.* 2016; Ma *et al.* 2019; Wu *et al.* 2019). These problems directly or indirectly affect human health and the ecological environment. Accurate information about the spatial extent and temporal change of ISA is critical for urban planning.

Due to various advantages, remote sensing has attracted unprecedented attention for urban IS (Liu and Shao 2013; Song *et al.* 2016). Medium-resolution remote sensing data, such as Landsat, provide a wealth of surface observations on a global scale. These data sets are widely used to monitor urban land cover and land use change (Xian *et al.* 2019). Many methods have been proposed to extract ISA with medium-resolution remote sensing data. Most of the approaches belong to regression (Elvidge *et al.* 2007; Lu *et al.* 2008), linear spectral mixture analysis (LSMA) (Sun *et al.* 2017; Xu *et al.* 2018), index method (Sekertekin *et al.* 2018; Tian *et al.* 2018; Wang *et al.* 2015), machine learning, and deep learning (Sun *et al.* 2011; Deng and Wu 2013; Shao *et al.* 2016; Deng *et al.* 2017; Huang *et al.* 2019a, 2019b; Sun *et al.* 2019; Liu *et al.* 2020; Misra *et al.* 2020). Bauer, Loffelholz and Wilson (2007) conducted a regression analysis using panchromatic digital orthophoto quadrangles, and the Landsat tasseled cap was used to derive the greenness to map the IS in the state of Minnesota, U.S. Yang *et al.* (2003) extended the regression method by developing a classification and regression tree algorithm, which used the classification result of high-resolution imagery as the training data set to generate rule-based modeling for prediction of sub-pixel percent imperviousness for a large area. Shao *et al.* (2020) put forward a fusion method for optical and synthetic aperture radar data to improve the extraction accuracy on urban impervious surface. Hong *et al.* (2013) extracted the ISA information based on Landsat images by using artificial neural network and monitored the IS change in the Dianci Basin by analyzing the multitemporal ISA. Zhang *et al.* (2018) used a semisupervised

Photogrammetric Engineering & Remote Sensing
Vol. 87, No. 7, July 2021, pp. 491–501.
0099-1112/21/491–501

© 2021 American Society for Photogrammetry
and Remote Sensing
doi: 10.14358/PERS.87.7.491

support vector machine (SVM) algorithm to classify IS and mapped the ISA by using time-series Landsat data.

Traditional methods mentioned above are insufficient in some respects. For example, the regression method has to consider major limitations related to model calibration, validation, and extrapolation of the models in other study areas. The LSMA method has a problem; that is, the ISA tends to be overestimated in the areas with small amounts of IS, but underestimated in the areas with large amounts of IS. The index method extracts ISA based on the spectral value, which is difficult to solve the problems of “metameric substance of same spectrum” and “metameric spectrum of same substance”. With the development of deep learning, the convolutional neural network (CNN) yields an excellent performance in the field of computer vision and has been applied in the classification of remotely sensed images. In the field of ISA, Zhang *et al.* (2018) compared the extracting results of ISA obtained with AlexNet, SVM, and GoogLeNet, based on optical image and synthetic-aperture radar (SAR) data. The results showed that AlexNet had a better performance than SVM and GoogLeNet. Sun *et al.* (2019) proposed an approach of three-dimensional (3D) convolutional neural networks (3D CNNs) to extract IS from the *WorldView-2* and airborne lidar data sets, and the results indicated that deep learning had great potential and better performance on IS extraction. Zhang *et al.* (2019) designed a spectral-spatial residual convolution neural network for impervious surface classification, and demonstrated the method was able to handle the massive imagery with high speed and accuracy. Due to the powerful learning ability, deep learning has great advantages in IS extraction.

However, for medium-resolution images including Landsat, mixed pixels usually account for a large proportion of pixels. Extracting the accurate ISA is difficult for the mixed pixels that represent several land cover types. It is still a challenge to extract IS based on medium-resolution satellite image data.

Our research objective is to perform a spatiotemporal analysis of the impervious surface for the Chengdu urban area based on the medium-resolution remote sensing data. Based on Landsat data sets and other information such as field survey, band calculation, digital surface model (DSM) (Grigillo and Kanjir 2012), vegetation index, and Google Earth, a labeled data set was created. Then, the CNN was constructed to extract the IS, and the performance was compared with that of back-propagation (BP) neural network. To analyze the spatiotemporal change of ISA for the Chengdu urban area, the standard deviational ellipse was calculated to identify the directional distribution of urban IS, and the spatiotemporal evolution was pinpointed.

Study Area

Chengdu city is located in the Chengdu plain,

as shown in Figure 1. The total population of Chengdu city was up to 13.99 million in 2016. In 1990, the urban area of Chengdu city was 1382 km², and the building land of the Chengdu urban area was 85.0 km². In 2016, the urban area came up to 4241.81 km², and the building land area was 770.78 km². In the past 26 years, Chengdu has shown a trend of rapid expansion. The main land cover types in the study area are vegetation, water, bare land, and impervious surface.

Data Set

In this paper, the period for our research was from 2001 to 2017. The images were collected every four years. The Landsat 5 thematic mapper (TM) images were gathered on 28 October 2001, on 14 April 2005, and on 24 March 2009, respectively. The Landsat 8 operational land imager (OLI) data were collected on 12 April 2013 and on 1 May 2017, respectively (Table 1).

Table 1. Images of study area.

No.	Satellite	Sensor	Time	Orbit No.	Resolution (m)	Cloud (%)
1	Landsat-5	TM	28 October 2001	129/39	30	5.86
2	Landsat-5	TM	14 April 2005	129/39	30	16.03
3	Landsat-5	TM	24 March 2009	129/39	30	1.00
4	Landsat-8	OLI	12 April 2013	129/39	30	6.52
5	Landsat-8	OLI	1 May 2017	129/39	30	0.86

No. = number; TM = thematic mapper; OLI = operational land imager.

In this paper, the bands of TM from band 1 to band 6 and the bands of OLI from band 2 to band 7 were used to extract

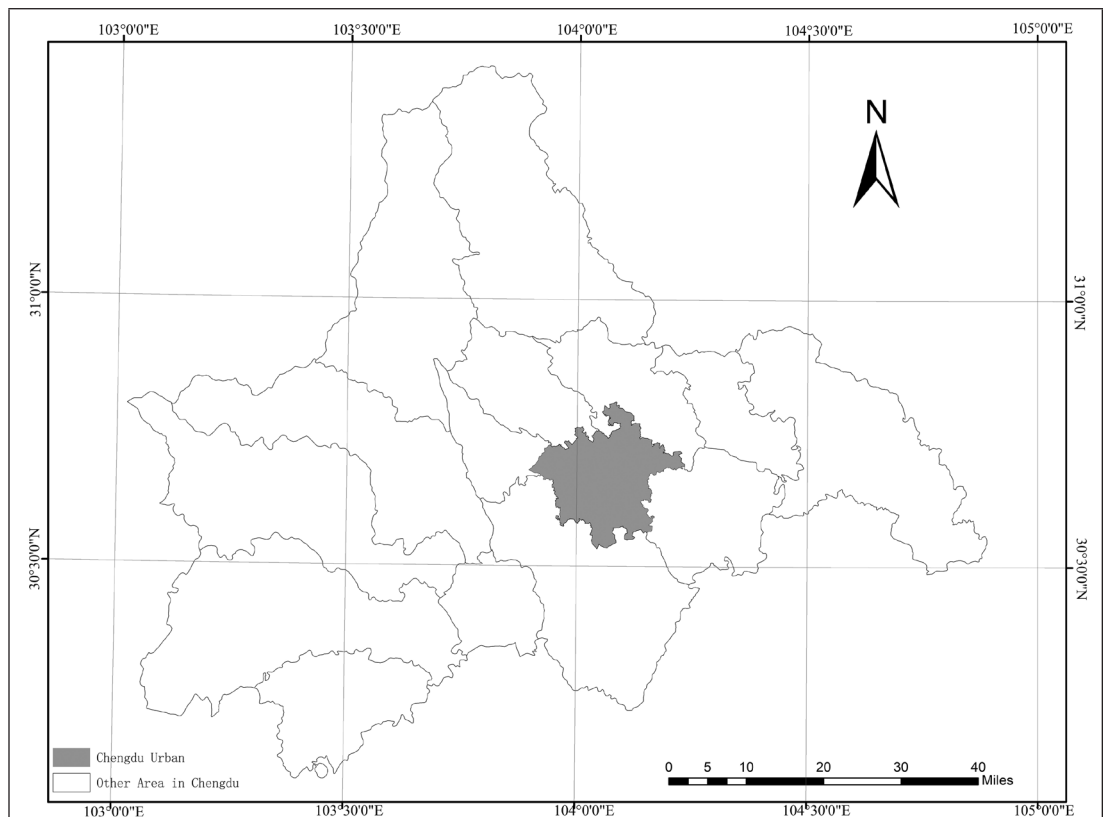


Figure 1. Overview of the Chengdu urban area.

the ISA. Radiation calibration and atmospheric correction were conducted on the TM images. The values of images were normalized within a range between 0 and 1. For BP, the input sample data was a one-dimensional vector, and six bands of each sample were input into the model in the form of a one-dimensional vector. For CNN, the input data was an image block, and the size of image block was set as $7 \times 7 \times 6$ in our experiments, where 7×7 is the length and width of the image, and 6 is the number of bands. The label of the image block was the type of central pixel. All data sets were labeled with the approach and the data sets were randomly divided into a training data set and testing data set at a ratio of 7:3.

Methods

Our flowchart is described in Figure 2.

First, the Landsat images are preprocessed with some operators such as radiation calibration and atmospheric correction. Second, combined with normalized vegetation index (NDVI), modified normalized difference water index (MNDWI), biophysical composition index (BCI), and Google Earth images, a labeled data set is then created. Third, a one-dimensional BP neural network model and a two-dimensional CNN model are used to extract the IS with the 2017 image, and the accuracy is evaluated and compared. Then, CNN is selected as our IS extraction algorithm. Finally, to investigate the spatio-temporal change of urban IS, the transition matrix is used to analyze the index of urban feature types quantitatively, the landscape metrics are used to examine its spatial change, and the standard deviational ellipse is used to identify its spatial direction.

Training Data Sets

The labeled data set is crucial for deep learning. In the Chengdu urban area, the roof of many buildings is covered by vegetation, leading to an underestimate of ISA if we only consider the spectral information when labeling the data set. Figure 3 is an instance mentioned above.

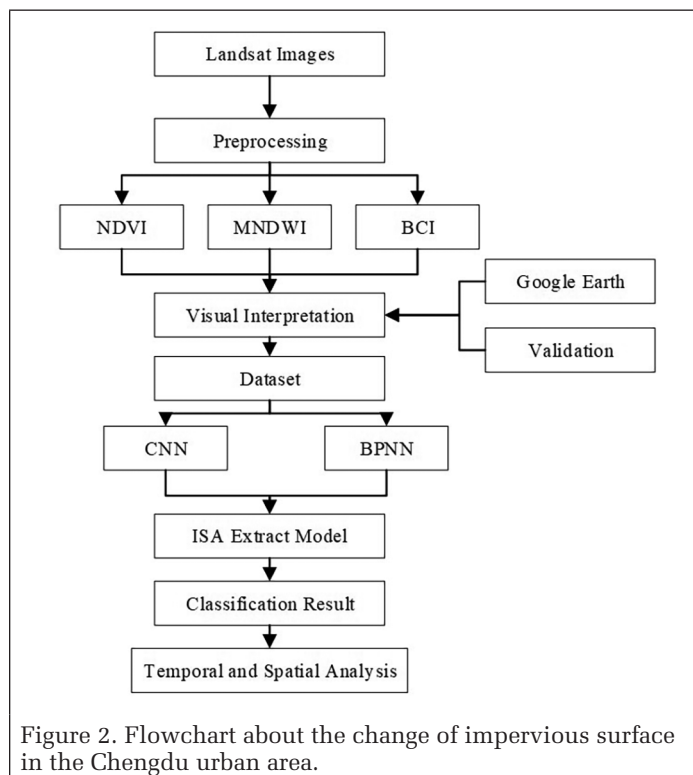


Figure 2. Flowchart about the change of impervious surface in the Chengdu urban area.

To solve the aforementioned problem, the DSM is introduced in the establishment of the data set. DSM is different from the digital elevation model, and it contains the elevation information of buildings and vegetation.

The interpretation of mixed pixels significantly affects the labeling accuracy of medium-resolution images. Based on the index method, the features including the location and visual interpretation are used to extract the IS of the Chengdu urban area. The vegetation sample points are selected with NDVI. The water sample points are identified with MNDWI, while the bare land and IS sample points are defined with BCI (Deng and



Figure 3. Roofs of buildings covered by vegetation.

Wu 2013). NDVI, MNDWI, and BCI can be expressed as (Carlson and Ripley 1997; Xu 2005):

$$NDVI = \frac{NIR - R}{NIR + R} \quad (1)$$

$$MNDWI = \frac{Green - SWIR}{Green + SWIR} \quad (2)$$

$$BCI = \left(\frac{H+L}{2} - V \right) / \left(\frac{H+L}{2} + V \right) \quad (3)$$

where NIR presents the near-infrared band, R denotes the visible red band, Green refers to the green light band, SWIR indicates the short-wave infrared band, H is the normalized brightness component of the tasseled cap transformation (Crist and Cicone 1984), which represents high reflectivity features, V denotes the normalized greenness component of the tasseled cap transformation, which represents vegetation, and L is the normalized humidity component of tasseled cap transformation. A higher BCI value represents ISA, while a lower BCI value indicates vegetation or bare soil. The samples are selected from the images of 2001, 2005, 2009, 2013, and 2017, respectively. The selection of sample points follows the principle that the spectrum separability is higher than 1.9, and the spatial distribution is uniform so as to ensure that the sample points cover all features as much as possible. The number of sample points selected in each year is depicted in Table 2.

Table 2. Number of sample pixels for the land cover types.

Types	Year				
	2001	2005	2009	2013	2017
Water	1953	1415	1140	1088	3130
Impervious	2573	2935	2227	2459	3987
Vegetation	3013	3007	2299	2201	4950
Bare land	509	1113	2047	1913	2337
Total	8048	8470	7713	7661	14 404

Classification

In this paper, the BP neural network and CNN are constructed to extract ISA, respectively. BP is a multilayer feedforward neural network, which is composed of an input layer, an output layer, and a hidden layer. The information is propagated through the network from top to bottom, and the hidden layer derives the information from the input layer. In contrast, the signal in the output layer is from the adjacent hidden layer, realizing the forward propagation. The error between the nodes is transmitted from the output layer to the input layer. The input layer has M nodes corresponding to the number of inputs, and the output layer has N nodes corresponding to the number of outputs for the network.

In recent years, CNN has been widely used in the computer vision field (LeCun *et al.* 2010). It has the characteristics of local receptive fields, shared weight, and spatial subsampling (Fanany *et al.* 2017). CNN is the hierarchical network like many traditional neural networks, which are composed of four types of layers: convolutional layer, active layer, pooling layer, and fully connected layer. CNN can learn the underlying features of images independently, without manually constructing features. In this paper, a multilayer CNN model is constructed with convolutional layers, rectified linear units (ReLU) layers, and pooling layers.

Accuracy Assessment

The overall accuracy (OA), user's accuracy (UA), producer's accuracy (PA), F1, Macro_F1, and the Kappa coefficient (KC)

are used as performance metrics in our study (Sim and Wright 2005; Tan 2005; McHugh 2012; Zheng *et al.* 2013):

$$OA = \frac{\text{Number of correctly classified pixels}}{\text{Number of overall pixels}} \times 100\% \quad (4)$$

$$UA = \frac{\text{Number of correctly classified pixels for a specific class}}{\text{Number of pixels classified as this class}} \times 100\% \quad (5)$$

$$PA = \frac{\text{Number of correctly classified pixels for a specific class}}{\text{Number of reference pixels classified for this class}} \times 100\% \quad (6)$$

$$KC = \frac{P_o - P_c}{1 - P_c} \quad (7)$$

$$F1 = \frac{2 \times UA \times PA}{UA + PA} \quad (8)$$

$$Macro_F1 = \sum_{i=1}^k \frac{F1_i}{N} \quad (9)$$

where P_o refers to the proportion of observed agreements, P_c represents the proportion of agreements expected by chance, N denotes the number of samples, and k indicates the number of land types.

Transition Matrix

The land cover transition matrix records the change of land cover types, and the matrix is expressed as an $N \times N$ matrix, where N is the number of ground object types in the images. The sum of each column in the state matrix represents the number of pixels for the initial ground object type. The sum of each row denotes the number of pixels for the final ground object type, and the diagonal of matrix represents the number of pixels that have no state change for each ground object type. Thus, the ISA, the proportion of ISA, the annual average change rate of ISA, and the change intensity of ISA can be calculated according to the state transition matrix. The information of IS for the Chengdu urban area can also be quantitatively investigated. Equation 10 and Equation 11 (Braimoh 2006) indicate the annual velocity (V) and the change intensity (CI), respectively.

$$V = \frac{A_{n+i} - A_i}{n} \quad (10)$$

$$CI = \frac{A_{n+i} - A_i}{nA_i} \times 100\% \quad (11)$$

where A_{n+i} represents the ISA of the $(n + i)$ th year, A_i denotes that of the i th year.

Landscape Metrics

According to Gao *et al.* (2019), Wu (2004), Zhang *et al.* (2014), and Wu (2009), eight standard landscape metrics including the number of patches (NP), patch density (PD), edge density (ED), patch cohesion index (COHESION), aggregation index (AI), largest patch index (LPI), landscape shape index (LSI), and landscape division index are selected to quantitatively describe the spatial morphology change of ISA for the Chengdu urban area. The formulas are defined as (Turner and Ruscher 1988; Milne *et al.* 1989; Zhang and Guo 2001; Sklenicka and Zouhar 2018):

$$ED_i = \frac{E_i}{A} \times 10^6 \quad (12)$$

where E_i denotes the total perimeter of the patches for the i th ground object, and A represents the total area of the Chengdu urban area.

$$PD_i = N_i/A \times 10^6 \quad (13)$$

where N_i indicates the number of patches of i th ground object. PD denotes the number of patches for a given ground object per 100 ha, which represents the uniformity of the spatial distribution.

$$AI = \left[\frac{g_{ii}}{\max \rightarrow g_{ii}} \right] \times 100\% \quad (14)$$

where g_{ii} represents the number of similar adjacent patches, $\max \rightarrow g_{ii}$ denotes the maximum number of similar adjacent patches.

$$\text{DIVISION} = \left[1 - \sum_{j=1}^n \frac{a_{ij}}{A} \right] \quad (15)$$

where a_{ij} represents the area of the j th patch in i th ground object. The larger DIVISION indicates a higher degree of fragmentation.

$$\text{LPI} = \frac{\max(a_{i1}, a_{i2}, \dots, a_{in})}{A_i} \times 100\% \quad (16)$$

where a_{in} denotes the area of the n th patch in the i th ground object, and A_i represents the total area of the i th ground object. LPI indicates the influence of maximum patch in the i th ground object.

$$\text{LSI} = \frac{0.25E}{\sqrt{A}} \times 100\% \quad (17)$$

where E denotes the total perimeter of the patches for all ground objects. LSI represents the complexity for landscape shape.

Standard Deviation Ellipse

Standard deviation ellipse (SDE) belongs to the spatial statistical algorithm. It is used to analyze the spatial extent and direction of the given data. The area of ellipse denotes the spatial extent, and the direction of long axis represents the distribution direction for the data. The bigger the ratio of the long axis to the short one is, the more concentrated the distribution direction of the data will be. The length of short axis of the ellipse denotes the degree of dispersion for the given data. The longer the short axis is, the higher the degree of dispersion is. When the short axis is equal to the long axis, it means that the distribution of data does not have direction. In this paper, the spatiotemporal evolution analysis of ISA is introduced to obtain the spatial directional characteristics of ISA. The standard deviation can be calculated with these steps (Lefever 1926).

1. Identifying the coordinate of average center point.

$$\bar{X} = \frac{\sum_{i=1}^n x_i}{n} \quad (18)$$

$$\bar{Y} = \frac{\sum_{i=1}^n y_i}{n} \quad (19)$$

where \bar{X} and \bar{Y} represent the coordinates of the average center point of the data, x_i and y_i denote the coordinates of the i th point in the data, and n is the amount of data.

2. Calculating the standard deviation for the center of ellipse.

$$\text{SDE}_x = \sqrt{\frac{\sum_{i=1}^n (x_i - \bar{X})^2}{n}} \quad (20)$$

$$\text{SDE}_y = \sqrt{\frac{\sum_{i=1}^n (y_i - \bar{Y})^2}{n}} \quad (21)$$

3. Identifying the rotation angle for the standard deviation ellipse.

$$\tan\theta = \frac{A+B}{C} \quad (22)$$

$$A = \left(\sum_{i=1}^n \tilde{x}_i^2 - \sum_{i=1}^n \tilde{y}_i^2 \right) \quad (23)$$

$$B = \sqrt{\left(\sum_{i=1}^n \tilde{x}_i^2 - \sum_{i=1}^n \tilde{y}_i^2 \right)^2 + 4 \left(\sum_{i=1}^n \tilde{x}_i \tilde{y}_i \right)^2} \quad (24)$$

$$C = 2 \sum_{i=1}^n \tilde{x}_i \tilde{y}_i \quad (25)$$

$$\tilde{x}_i = \bar{X} - x_i \quad (26)$$

$$\tilde{y}_i = \bar{Y} - y_i \quad (27)$$

where θ denotes the rotation angle of ellipse from the north, \tilde{x}_i and \tilde{y}_i are the difference between the average center point and the i th point.

4. Calculating the standard deviation ellipse.

$$\sigma_x = \sqrt{2} \sqrt{\frac{\sum_{i=1}^n (\tilde{x}_i \cos\theta - \tilde{y}_i \sin\theta)^2}{n}} \quad (28)$$

$$\sigma_y = \sqrt{2} \sqrt{\frac{\sum_{i=1}^n (\tilde{x}_i \sin\theta + \tilde{y}_i \cos\theta)^2}{n}} \quad (29)$$

5. Identifying the equation of ellipse.

$$\left(\frac{x}{\sigma_x} \right)^2 + \left(\frac{y}{\sigma_y} \right)^2 = S \quad (30)$$

where S is the confidence coefficient from the Chi-Square probabilities table.

Experimental Setup

Experiments

We used a multilayer BP neural network structure including an input layer, two hidden layers, and an output layer, with 64 neurons for the first hidden layer and 32 for the second hidden layer. The stochastic gradient descent (SGD) was used as the optimization algorithm. The batch size and learning rate of the model were adjusted, respectively, and the optimal parameter combination was selected based on the overall accuracy. After trial and error, the batch size was set as 64, and the learning

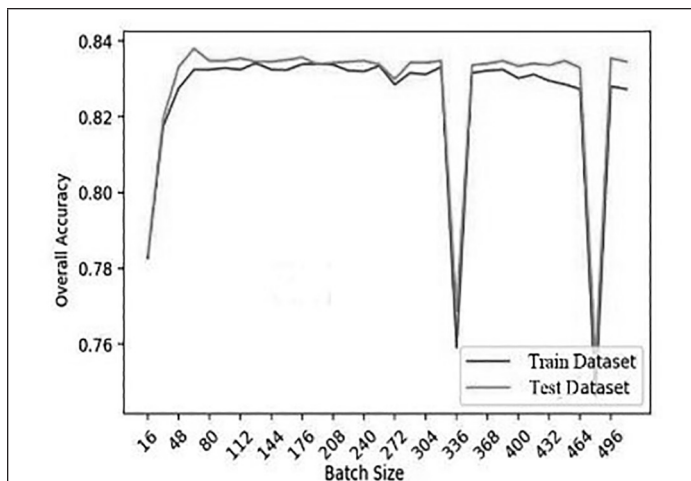


Figure 4. Overall accuracy of different batch sizes for back-propagation.

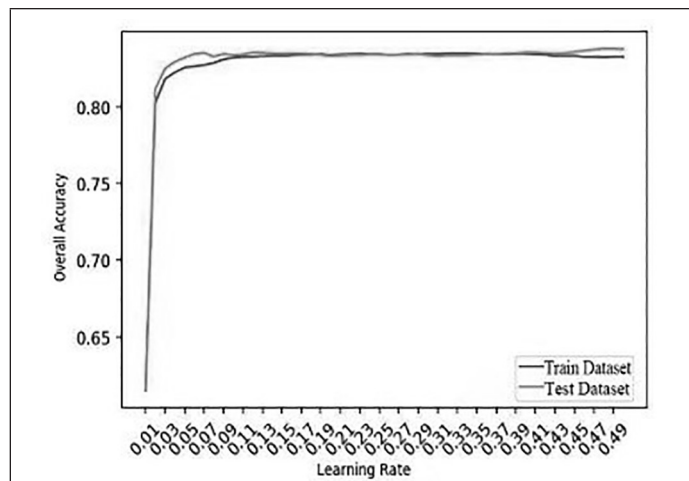


Figure 5. Overall accuracy of different learning rates for back-propagation.

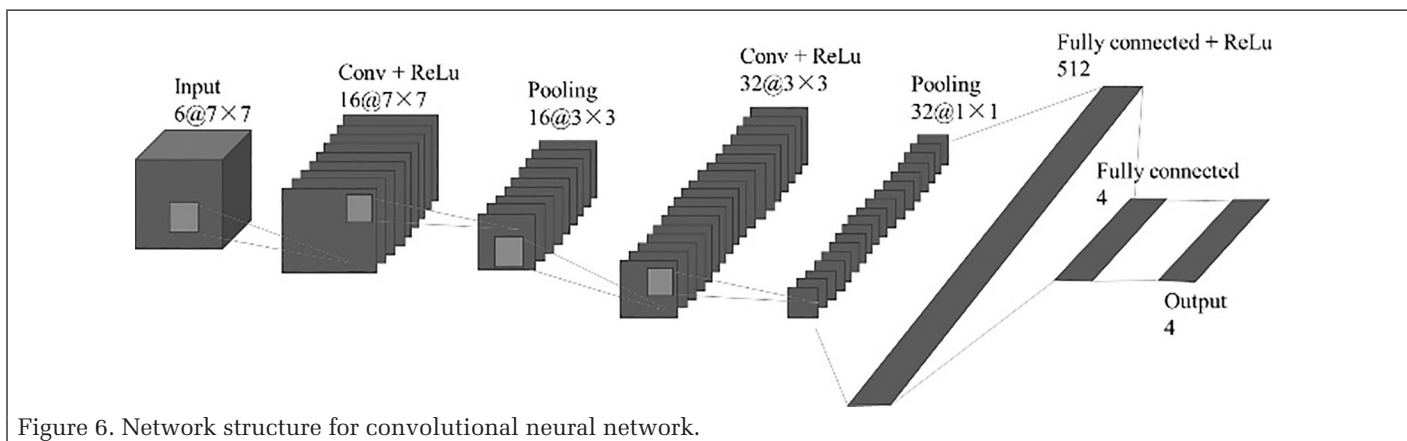


Figure 6. Network structure for convolutional neural network.

rate was set as 0.05. Figure 4 and Figure 5 report the impacts of batch size and learning rate on the overall accuracy of BP.

Based on the characteristics of the data set, a three-layer CNN model was constructed, and it was mainly composed of the input layer, convolutional layer, ReLu layer, pooling layer, and full connection layer. The structure of CNN in this study is shown in Figure 6. SGD was used to train the parameters of the convolutional layer and the full connection layer so that the classification results calculated by the CNN could match the labels of each image in the training data set. The image block size of the input model was $7 \times 7 \times 6$. In the convolution process, zero-padding was executed. After convolution operation, the feature maps of the same size as the original images were derived. Max-pooling was also used, and more texture information of the images was kept. The batch size and learning rate of the model were also set as the optimal combination. The architecture of CNN in this paper is depicted in Table 3.

Table 3. Architecture of convolutional neural network.

Layer Type	Filter Size	Output Size
Input	— ^a	$7 \times 7 \times 6$
Conv + ReLu	3×3	$7 \times 7 \times 16$
Pooling	2×2	$3 \times 3 \times 16$
Conv + ReLu	3×3	$3 \times 3 \times 32$
Pooling	2×2	$1 \times 1 \times 32$
Fully connected + ReLu	—	1×512
Fully connected	—	1×4
Softmax	—	1×4

Conv = convolutional; ReLu = rectified linear units.
^aDashes indicate XXXX.

Results

Model Performance

For BP, we used 4321 sample points to evaluate the classification accuracy for our model. In these sample points, 939 sample points belonged to water bodies, 1196 were IS, 1485 belonged to vegetation, and 701 were bare land. In the experiment, the batch size was set as 64, and the learning rate was set as 0.05, as mentioned above. Figure 7 depicts the change of loss in the process of training with the image in 2009.

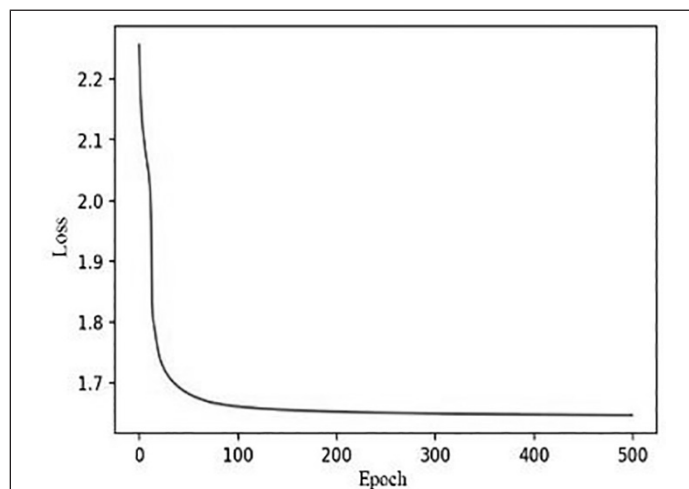


Figure 7. Loss curve of back-propagation with the image in 2009.

Table 4. Confusion matrix and accuracy of back-propagation with the image in 2017.

Types	Impervious			Bare Land	Total	PA (%)
	Water	Surface	Vegetation			
Water	884	0	13	42	939	94.14
Impervious Surface	95	709	20	372	1196	59.28
Vegetation	69	1	1410	5	1485	94.95
Bare Land	35	67	2	597	701	85.16
Total	1083	777	1445	1016	— ^a	—
UA (%)	81.63	91.25	97.58	58.76	—	—

UA = user's accuracy; PA = producer's accuracy.
^aDashes indicate XXXX.

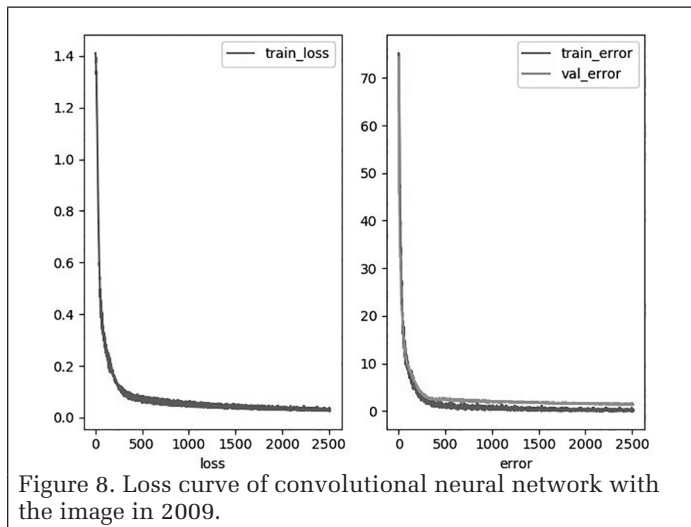


Figure 8. Loss curve of convolutional neural network with the image in 2009.

The confusion matrix based on the classification of BP with the image in 2017, the user accuracy, and producer accuracy of various samples are described in Table 4. For CNN, 4296 validation sample points were labeled to evaluate the accuracy of our model. In these sample points, 936 points belonged to water bodies, 1193 were IS, 1470 belonged to vegetation, and 697 were bare land. Figure 8 describes the change of loss in the process of training with the image in 2009.

The confusion matrix based upon CNN, the user accuracy, and producer accuracy of the land covers are described in Table 5. OA, Macro F1, and Kappa are shown in Table 6. From Table 6, it can obviously be seen that CNN achieved a better performance than BP.

With our CNN model, the land cover maps were yielded in 2001, 2005, 2009, 2013, and 2017, respectively (Figure 9, Figure 10, Figure 11, Figure 12, and Figure 13, see next page).

Change Analysis of ISA

The land cover maps were analyzed to investigate the characteristics of ISA changes for the Chengdu urban area from 2001 to 2017. Figure 14 discloses the changes in the proportion of each land cover type.

From Figure 14, it can be seen that the ISA accounted for the largest proportion, the vegetation was ranked second, the bare land maintained a small proportion but with a peak in 2013, while the water bodies almost kept the least proportion in the sixteen years. From 2001 to 2009, the percentage of ISA was increasing, but a trough occurred in 2013. By contrast, the water bodies and vegetation had almost been decreasing year by year.

To further investigate the transformation of land cover types, the state transition matrix was derived to analyze the area changes of land cover types for the Chengdu urban area.

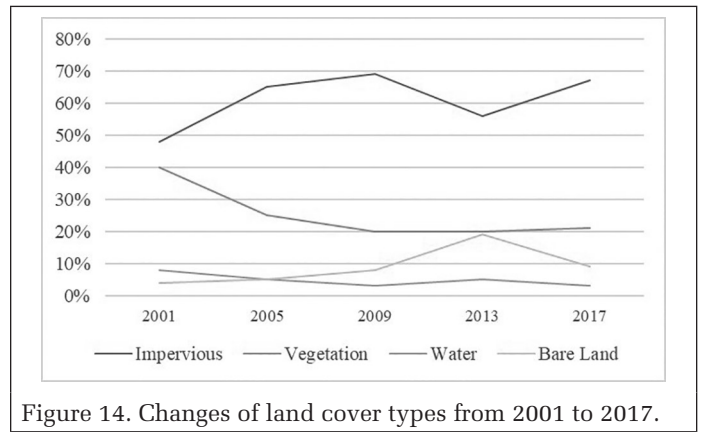


Figure 14. Changes of land cover types from 2001 to 2017.

Table 5. Confusion matrix and accuracy of convolutional neural network with the image in 2017.

Types	Impervious			Bare Land	Total	PA (%)
	Water	Surface	Vegetation			
Water	919	14	2	1	936	98.18
Impervious Surface	4	1169	13	7	1193	97.99
Vegetation	1	9	1457	3	1470	99.12
Bare Land	0	14	4	679	697	97.42
Total	924	1206	1476	690	— ^a	—
UA (%)	99.46	96.93	98.71	98.41	—	—

UA = user's accuracy; PA = producer's accuracy.
^aDashes indicate XXXX.

Table 6. Macro F1, overall accuracy (OA), Kappa of back-propagation (BP) and convolutional neural network (CNN) with the image in 2017.

Models	Macro F1 (%)	OA (%)	Kappa
BP	81.27	83.31	0.78
CNN	98.28	98.32	0.98

Table 7. Transition matrix from 2001 to 2005.

Types	2005				
	Water	Impervious Surface	Vegetation	Bare Land	Total
Water	1554	1288	748	197	3787
Impervious Surface	220	19 917	1313	684	22 134
Vegetation	360	7370	9719	1302	18 752
Bare Land	23	1383	154	173	1733
Total	2158	29 958	11 935	2356	46 406

Note: The unit is ha.

Table 8. Transition matrix from 2005 to 2009.

Types	2009				
	Water	Impervious Surface	Vegetation	Bare Land	Total
Water	919	668	390	181	2158
Impervious Surface	373	25 500	2325	1759	29 958
Vegetation	198	4068	6420	1249	11 935
Bare Land	76	1634	287	358	2356
Total	1566	31 870	9422	3548	46 406

Note: The unit is ha.

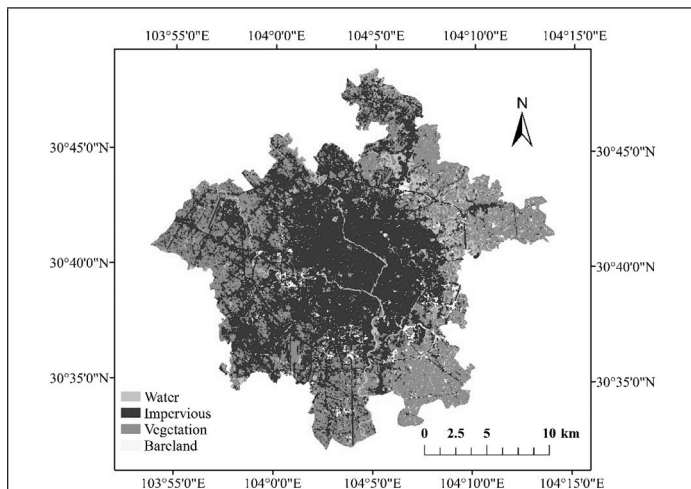


Figure 9. Land cover map of 2001.

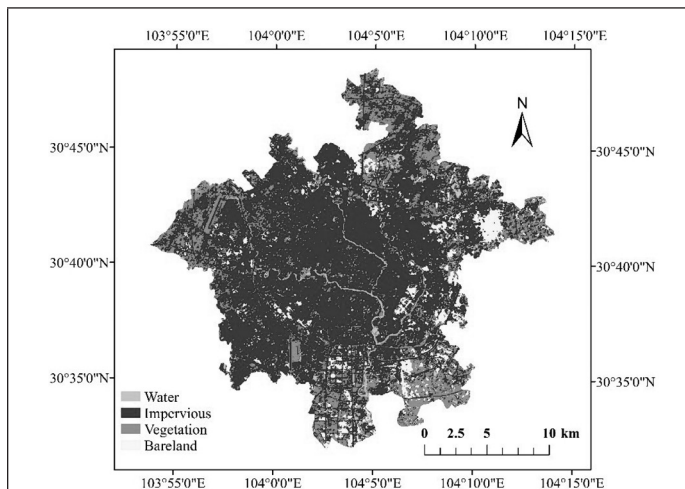


Figure 11. Land cover map of 2009.

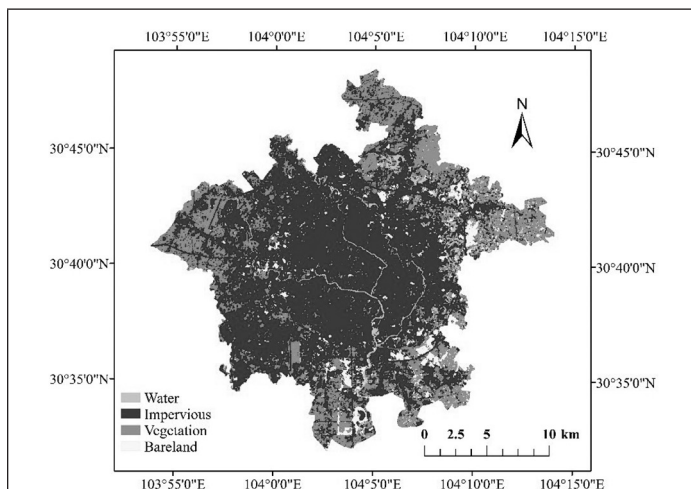


Figure 10. Land cover map of 2005.

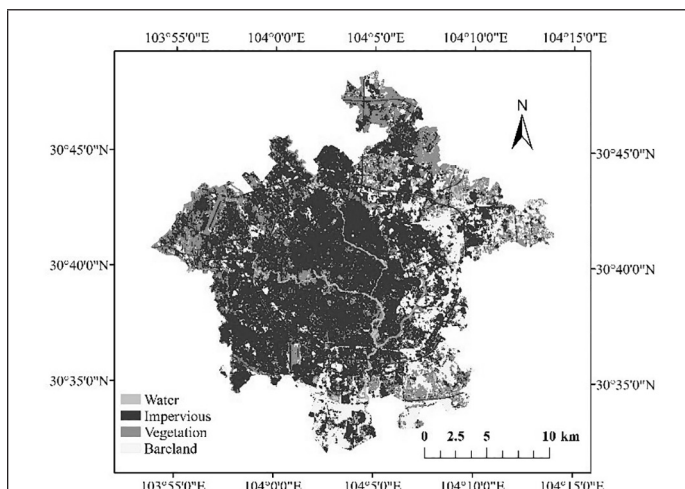


Figure 12. Land cover map of 2013.

Table 9. Transition matrix from 2009 to 2013.

Types		2013				Total
		Water	Impervious Surface	Vegetation	Bare Land	
2009	Water	895	232	305	134	1566
	Impervious Surface	1010	23 120	3457	4284	31 870
	Vegetation	267	1548	4973	2633	9422
	Bare Land	90	1489	378	1592	3548
	Total	2261	26 389	9113	8643	46 406

Note: The unit is ha.

Table 10. Transition matrix from 2013 to 2017.

Type		2017				Total
		Water	Impervious Surface	Vegetation	Bare Land	
2013	Water	921	1111	168	61	2261
	Impervious Surface	168	23 380	1711	1130	26 389
	Vegetation	160	2366	5970	617	9113
	Bare Land	185	3958	2106	2394	8643
	Total	1434	30 814	9955	4203	46 406

Note: The unit is ha.

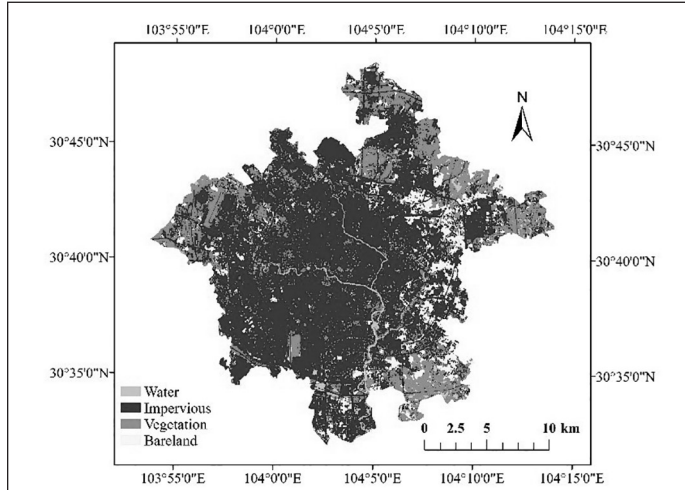


Figure 13. Land cover map of 2017.

From the tables, it can be seen that (1) the ISA increased from 2001 to 2005, and the vegetation of 7370 ha was converted to IS (see Table 7). (2) The ISA continued to increase from 2005 to 2009, and the vegetation of 4068 ha changed to IS (see Table 8). (3) The ISA decreased from 2009 to 2013, and the IS of 4284 ha changed into bare land (see Table 9). (4) The ISA increased from 26 389 ha to 30 814 ha from 2013 to 2017 because the bare land of 3958 ha was transformed into IS (see Table 10).

The locations of the IS center in 2001, 2005, 2009, 2013, and 2017 are calculated and reported in Figure 15. Between 2001 and 2017, there was a slight shift for the center of the IS. From 2001 to 2005, the movement direction was southeast, and the distance was 398 m. From 2005 to 2009, the direction was northeast, and the distance was 462 m. From 2009 to 2013, the direction was southwest, and the distance was 657 m. From 2013 to 2017, the direction was southeast, and the distance was 388 m.

The standard deviational ellipse of IS in 2001, 2005, 2009, 2013, and 2017 are calculated and depicted in Figure 16.

The standard deviational ellipse reflected the directional distribution of IS. The long axis denoted the distribution direction of the data, and the short one indicated the distribution range of the data. When the ratio of the long to the short approached 1, it meant that there was no obvious distribution direction for the data. It can be seen from Figure 16, the standard deviational ellipse of IS in each year was almost circular, indicating that the IS in the Chengdu urban area did not have an obvious distribution direction in these years.

Table 11 describes the landscape metrics of IS at length. It indicates that the NP and PD decreased, while the LPI was increasing yearly. As the IS increased in these years, this phenomenon disclosed that the IS in the Chengdu urban area gradually expanded from the small and fragmented patches to the larger ones. The AI became larger, it denoted that the adjacent patches of IS were increasing. The COHESION was up to 99%, mainly because of a huge IS patch, which dominated the connectivity. The ED represented the openness, and the increasing ED disclosed that the degree of fragmentation became bigger. This phenomenon was beneficial to improve the energy flow between the surface patch and its surrounding ones. The LSI was the complexity of the IS shape. The decreasing LSI indicated that the complexity of IS shape became smaller.

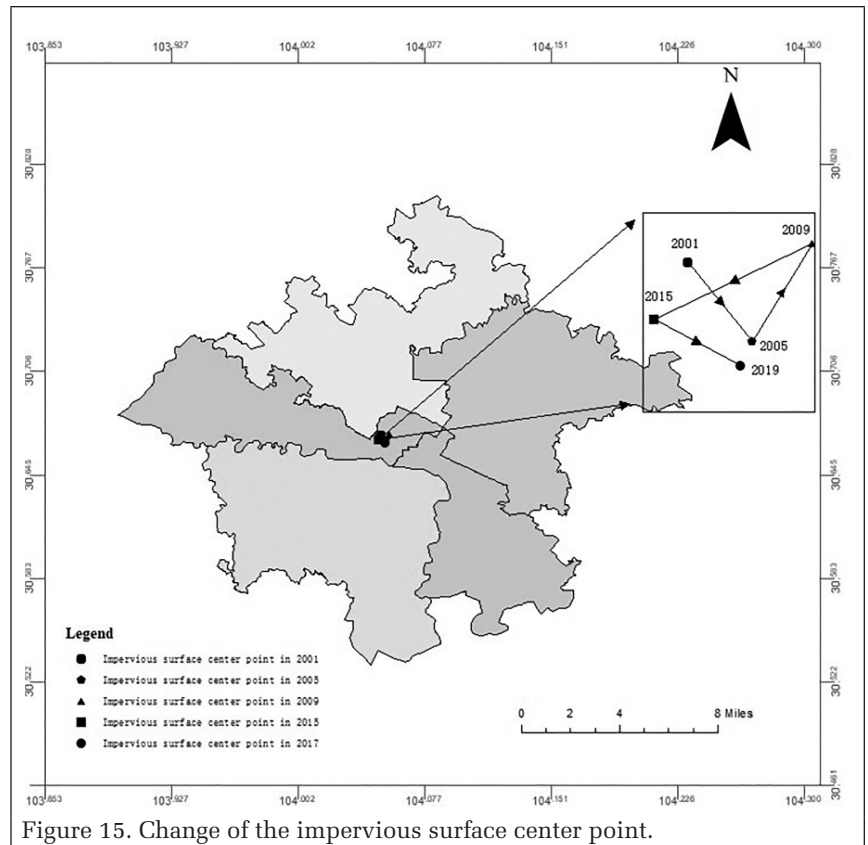


Figure 15. Change of the impervious surface center point.

According to the results of IS extraction for the Chengdu urban area, the ISA accounted for the bigger percent, the vegetation was ranked second, and the water bodies were the least. The percentage of ISA has a trough in 2013. From 2001 to 2009, the proportion of vegetation area increased, but it was stabilized after 2009. Bare land showed an upward trend from 2001 to 2013, but it decreased after 2013. It could be presumed that the ISA was mostly transformed by vegetation from 2001 to 2009. In 2013, there was a process of demolition and construction in the Chengdu urban area, which led to a decrease in the proportion

Discussion

The confusion matrix in our experiments showed that BP often failed to distinguish IS and bare land. The classification of pixels by BP was based on the spectral information. Thus, different land cover types with similar spectra were misclassified. The input of CNN was an image block, which contained the spectral and texture information. And the confusion matrix showed that CNN could effectively improve the classification between the IS and bare land. According to Table 6, CNN yielded an excellent performance in Macro F1, overall accuracy, and Kappa coefficient.

Table 11. Landscape metrics of impervious surface.

Year	NP	PD (/100ha)	ED (m/ha)	COHESION (%)	AI (%)	LPI (%)	LSI	DIVISION (%)
2001	2593	5.59	70.98	99.81	88.88	42.49	56.03	0.82
2005	1544	3.37	59.08	99.88	93.12	58.82	40.63	0.65
2009	1198	2.58	73.36	99.93	91.9	65.97	49.09	0.56
2013	1791	3.86	75.29	99.86	90.02	50	54.93	0.75
2017	1305	2.81	66.07	99.92	92.42	63.11	45.21	0.6

NP = number of patches; PD = patch density; ED = edge density; COHESION = patch cohesion index; AI = aggregation index; LPI = largest patch index; LSI = landscape shape index; DIVISION = degree of fragmentation.

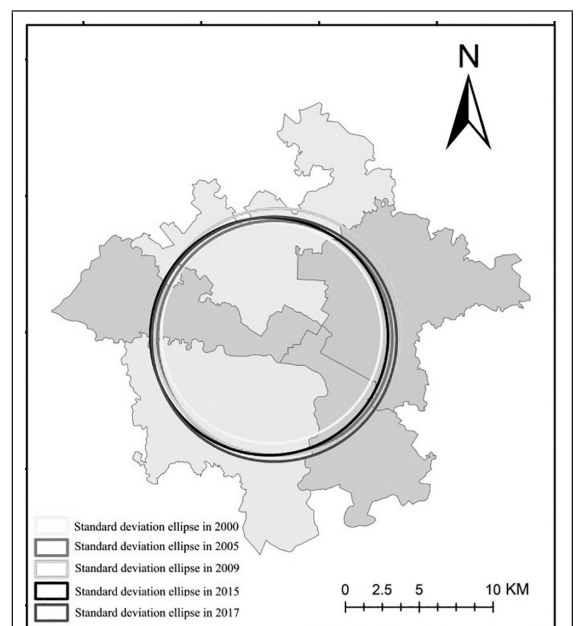


Figure 16. Standard deviational ellipse of impervious surface.

of ISA and an increase in the proportion of bare land. The transition matrix could validate our premise.

In the process of urban development, the policy was the main cause for the change of IS. According to the master planning of the Chengdu urban area, the main space expansion direction for an urban area was from east and south between 2003 and 2015. The main expansion direction of the urban area was from south to north between 2015 and 2020. The policy revealed the reasons why the IS center for the Chengdu urban area shifted to the east from 2001 to 2009, to the south from 2009 to 2017, and the distribution of IS was almost circular.

According to the “Statistical Yearbook” of Chengdu over the years, the area of farmland could be obtained. Table 12 depicts the area changes for the farmland, IS, and bare land in the Chengdu urban area. From Table 12, it can be seen that the area of farmland in the Chengdu urban area was decreasing year by year. From 2001 to 2005, the area of farmland decreased with a rate of -4537 ha/a. From 2013 to 2017, the farmland had a slight change, with a rate of -283 ha/a. From 2001 to 2005, the change rate of IS and bare land area was 8447 ha/a, and from 2013 to 2017, the rate of IS and bare land area was -15 ha/a. The trend of IS and bare land was similar to that of farmland, and the farmland in the Chengdu urban area had gradually converted into IS and bare land over the past sixteen years in the Chengdu urban area. In addition, the changes of gross domestic product (GDP) for the secondary industry were similar to the changes of ISA from 2001 to 2017. Thus, the spatiotemporal evolution of ISA was associated with the economic development of the Chengdu urban area over the past sixteen years.

Table 12. Change rate of farmland.

Periods	Types		
	Farmland (Ha/a)	IS and Bare Land (Ha/a)	IS (Ha/a)
2001–2005	-4537	8447	7824
2005–2009	-838	3104	1912
2009–2013	-1169	-386	-5418
2013–2017	-283	-15	4425

IS = impervious surface.

Conclusions

In this paper, the Landsat images were used to investigate the spatiotemporal evolution of ISA for the Chengdu urban area. The performance of two methods were compared and the experimental results showed that CNN achieved a higher accuracy. With the trained CNN, the ISA in 2001, 2005, 2009, 2013, and 2017 was extracted, respectively. And the spatiotemporal evolution of ISA for the Chengdu urban area was analyzed thoroughly. The ISA kept an increased trend from 2001 to 2017, and it was mostly transformed by vegetation. In addition, the GDP change of the secondary industry was similar to the evolution of ISA between 2001 and 2017 for the Chengdu urban area. Thus, the spatiotemporal evolution of IS was associated with the economic development of the Chengdu urban area in the past sixteen years. Therefore, the government has to switch the development patterns and take more measures to reduce the ISA to relieve the pressure of the ecological environment for the Chengdu urban area.

Acknowledgments

This paper is funded by the Open Fund of State Key Laboratory of Water Resources and Hydropower Engineering Science (Grant No. 2014SWG04 and Grant No. 2018SWG02); Open Fund of Hubei Provincial Key Lab of Water System

Science for Sponge City Construction, Wuhan University (Grant No. 201904); Open Fund of Key Laboratory of Urban Land Resources Monitoring and Simulation, Ministry of Natural Resources (Grant No. KF-2019-04-069 and Grant No. KF-2019-04-074); State Key Laboratory of Remote Sensing Science (Grant No. OFSLRSS201819); Science Research Program of Natural Resources Department of Sichuan Province (Grant No. KJ-2020-3 and Grant No. KJ-2021-13); the Key Technologies Research and Development Program of Sichuan Province (Grant No. 2020YFSY0041); Guangxi Key Laboratory for Spatial Information and Geomatics (Grant No. 17-259-16-14 and Grant No. 19-050-11-06).

References

- Bauer, M. E., B. C. Loffelholz and B. Wilson. 2007. Estimating and mapping impervious surface area by regression analysis of Landsat imagery. In *Remote Sensing of Impervious Surfaces*, 31–48. Boca Raton, Fla.: CRC Press.
- Braimoh, A. K. 2006. Random and systematic land-cover transitions in northern Ghana. *Agriculture, Ecosystems & Environment* 113(1–4):254–263.
- Carlson, T. N. and D. A. Ripley. 1997. On the relation between NDVI, fractional vegetation cover, and leaf area index. *Remote Sensing of Environment* 62(3):241–252.
- Crist, E. P. and R. C. Cicone. 1984. A physically-based transformation of thematic mapper data—The TM tasseled cap. *IEEE Transactions on Geoscience and Remote Sensing* 3:256–263.
- Deng, C., C. Li, Z. Zhu, W. Lin and L. Xi. 2017. Subpixel urban impervious surface mapping: The impact of input Landsat images. *ISPRS Journal of Photogrammetry and Remote Sensing* 133:89–103.
- Deng, C. and C. Wu. 2013. The use of single-date MODIS imagery for estimating large-scale urban impervious surface fraction with spectral mixture analysis and machine learning techniques. *ISPRS Journal of Photogrammetry and Remote Sensing* 86:100–110.
- Elvidge, C. D., B. T. Tuttle, C. Sutton, K. E. Baugh, A. T. Howard, C. Milesi, B. Bhaduri and R. Nemani. 2007. Global distribution and density of constructed impervious surfaces. *Sensors* 7(9):1962–1979.
- Fanany, M. I. 2017. Handwriting recognition on form document using convolutional neural network and support vector machines (CNN-SVM). Pages 1–6 in *Proceedings 2017 5th IEEE International Conference on Information and Communication Technology (ICoICT)*, held in Melaka, Malaysia.
- Gao, Z., M. Kii, A. Nonomura and K. Nakamura. 2019. Urban expansion using remote-sensing data and a monocentric urban model. *Computers, Environment and Urban Systems* 77:101152.
- Grigillo, D. and U. Kanjir. 2012. Urban object extraction from digital surface model and digital aerial images. *ISPRS Annals of the Photogrammetry, Remote Sensing and Spatial Information Sciences* 3:215–220.
- Herwindiati, D. E., J. Hendryli and L. Hiryanto. 2017. Impervious surface mapping using robust depth minimum vector variance regression. *European Journal of Sustainable Development* 6(3):29–29.
- Hong, L., G. Zhou, K. Yang and M. Deng. 2013. The study of spatiotemporal variation of impervious surfaces for Dianci basin using TM imagery from 2002 to 2009. Pages 1–4 in *Proceedings 2013 21st IEEE International Conference on Geoinformatics*, held in Kaifeng, China.
- Huang, F., Y. Yu and T. Feng. 2019a. Automatic extraction of impervious surfaces from high resolution remote sensing images based on deep learning. *Journal of Visual Communication and Image Representation* 58:453–461.
- Huang, F., Y. Yu and T. Feng. 2019b. Automatic extraction of urban impervious surfaces based on deep learning and multi-source remote sensing data. *Journal of Visual Communication and Image Representation* 60:16–27.
- LeCun, Y., K. Kavukcuoglu and C. Farabet. 2010. Convolutional networks and applications in vision. Pages 253–256 in *Proceedings of 2010 IEEE International Symposium on Circuits and Systems*, held in Paris, France.

- Lefever, D. W. 1926. Measuring geographic concentration by means of the standard deviational ellipse. *American Journal of Sociology* 32(1):88–94.
- Li, X. and Y. Zhou. 2017. Urban mapping using DMSP/OLS stable night-time light: A review. *International Journal of Remote Sensing* 38(21):6030–6046.
- Liu, C. and Z. Shao. 2013. MNDISI: A multi-source composition index for impervious surface area estimation at the individual city scale. *Remote Sensing Letters* 4(8):803–812.
- Liu, J., C. Liu, Q. Feng and Y. Ma. 2020. Subpixel impervious surface estimation in the Nansi Lake Basin using random forest regression combined with GF-5 hyperspectral data. *Journal of Applied Remote Sensing* 14(3):034515.
- Lu, D., H. Tian, G. Zhou and H. Ge. 2008. Regional mapping of human settlements in southeastern China with multi-sensor remotely sensed data. *Remote Sensing of Environment* 112(9):3668–3679.
- Ma, Y., K. Yang, S. Zhang and M. Li. 2019. Impacts of large-area impervious surfaces on regional land surface temperature in the great Pearl River Delta, China. *Journal of the Indian Society of Remote Sensing* 47(11):1831–1845.
- McHugh, M. L. 2012. Interrater reliability: The kappa statistic. *Biochemia Medica* 22(3):276–282.
- Milne, B. T., K. M. Johnston and R. T. Forman. 1989. Scale-dependent proximity of wildlife habitat in a spatially-neutral Bayesian model. *Landscape Ecology* 2(2):101–110.
- Misra, M., D. Kumar and S. Shekhar. 2020. Assessing machine learning based supervised classifiers for built-up impervious surface area extraction from Sentinel-2 images. *Urban Forestry & Urban Greening* 53:126714.
- Nie, Q., W. Man, Z. Li and Y. Huang. 2016. Spatio-temporal impact of urban impervious surface on land surface temperature in Shanghai, China. *Canadian Journal of Remote Sensing* 42(6):680–689.
- Piano, E., K. De Wolf, F. Bona, D. Bonte, D. E. Bowler, M. Isaia, L. Lens, T. Merckx, D. Mertens, M. Van Kerckvoorde and L. De Meester. 2017. Urbanization drives community shifts towards thermophilic and dispersive species at local and landscape scales. *Global Change Biology* 23(7):2554–2564.
- Sekertekin, A., S. Abdikan and A. M. Marangoz. 2018. The acquisition of impervious surface area from Landsat 8 satellite sensor data using urban indices: A comparative analysis. *Environmental Monitoring and Assessment* 190(7):381.
- Shao, Z., H. Fu, D. Li, O. Altan and T. Cheng. 2019. Remote sensing monitoring of multi-scale watersheds impermeability for urban hydrological evaluation. *Remote Sensing of Environment* 232:111338.
- Shao, Z., H. Fu and L. Yin. 2016. Mapping urban impervious surface by fusing optical and SAR data at the decision level. *Remote Sensing* 8(11):945.
- Shao, Z., C. Li, D. Li, O. Altan, L. Zhang and L. Ding. 2020. An accurate matching method for projecting vector data into surveillance video to monitor and protect cultivated land. *ISPRS International Journal Geo-Information* 9:448. <https://doi.org/10.3390/ijgi9070448>.
- Shao, Z. and C. Liu. 2014. The integrated use of DMSP-OLS nighttime light and MODIS data for monitoring large-scale impervious surface dynamics: A case study in the Yangtze River Delta. *Remote Sensing* 6(10):9359–9378.
- Shao, Z., W. Wu and S. Guo. 2020. IHS—GTF: A fusion method for optical and synthetic aperture radar data. *Remote Sensing* 12:2796. <https://doi.org/10.3390/rs12172796>.
- Sim, J. and C. C. Wright. 2005. The kappa statistic in reliability studies: Use, interpretation, and sample size requirements. *Physical Therapy* 85(3):257–268.
- Sklenicka, P. and J. Zouhar. 2018. Predicting the visual impact of onshore wind farms via landscape indices: A method for objectivizing planning and decision processes. *Applied Energy* 209:445–454.
- Song, X. P., J. O. Sexton, C. Huang, S. Channan and J. R. Townshend. 2016. Characterizing the magnitude, timing and duration of urban growth from time series of Landsat-based estimates of impervious cover. *Remote Sensing of Environment* 175:1–13.
- Sun, G., X. Chen, J. Ren, A. Zhang and X. Jia. 2017. Stratified spectral mixture analysis of medium resolution imagery for impervious surface mapping. *International Journal of Applied Earth Observation and Geoinformation* 60:38–48.
- Sun, Z., H. Guo, X. Li, L. Lu and X. Du. 2011. Estimating urban impervious surfaces from Landsat-5 TM imagery using multilayer perceptron neural network and support vector machine. *Journal of Applied Remote Sensing* 5(1):053501.
- Sun, Z., X. Zhao, M. Wu and C. Wang. 2019. Extracting urban impervious surface from WorldView-2 and airborne LiDAR data using 3D convolutional neural networks. *Journal of the Indian Society of Remote Sensing* 47(3):401–412.
- Tan, S. 2005. Neighbor-weighted k-nearest neighbor for unbalanced text corpus. *Expert Systems with Applications* 28(4):667–671.
- Tian, Y., H. Chen, Q. Song and K. Zheng. 2018. A novel index for impervious surface area mapping: Development and validation. *Remote Sensing* 10(10):1521.
- Turner, M. G. and C. L. Ruscher. 1988. Changes in landscape patterns in Georgia, USA. *Landscape Ecology* 1(4):241–251.
- Wang, Z., C. Gang, X. Li, Y. Chen and J. Li. 2015. Application of a normalized difference impervious index (NDII) to extract urban impervious surface features based on Landsat TM images. *International Journal of Remote Sensing* 36(4):1055–1069.
- Wu, C. 2004. Normalized spectral mixture analysis for monitoring urban composition using ETM+ imagery. *Remote Sensing of Environment* 93(4):480–492.
- Wu, C. 2009. Quantifying high-resolution impervious surfaces using spectral mixture analysis. *International Journal of Remote Sensing* 30(11):2915–2932.
- Wu, X., B. Li, M. Li, M. Guo, S. Zang and S. Zhang. 2019. Examining the relationship between spatial configurations of urban impervious surfaces and land surface temperature. *Chinese Geographical Science* 29(4):568–578.
- Xian, G., H. Shi, J. Dewitz and Z. Wu. 2019. Performances of WorldView-3, Sentinel-2, and Landsat 8 data in mapping impervious surface. *Remote Sensing Applications: Society and Environment* 15:100246.
- Xu, H. 2005. A study on information extraction of water body with the modified normalized difference water index (MNDWI). *Journal of Remote Sensing* 5:589–595.
- Xu, R., J. Liu and J. Xu. 2018. Extraction of high-precision urban impervious surfaces from Sentinel-2 multispectral imagery via modified linear spectral mixture analysis. *Sensors* 18(9):2873.
- Yang, L., C. Huang, C. G. Homer, B. K. Wylie and M. J. Coan. 2003. An approach for mapping large-area impervious surfaces: synergistic use of Landsat-7 ETM+ and high spatial resolution imagery. *Canadian Journal of Remote Sensing* 29(2):230–240.
- Zhang, H., L. Wan, T. Wang, Y. Lin, H. Lin and Z. Zheng. 2018. A comparative study of impervious surface estimation from optical and SAR data using deep convolutional networks. Pages 1656–1659 in *Proceedings IEEE International Geoscience and Remote Sensing Symposium*, held in Valencia, Spain.
- Zhang, L., M. Zhang and Y. Yao. 2018. Mapping seasonal impervious surface dynamics in Wuhan urban agglomeration, China from 2000 to 2016. *International Journal of Applied Earth Observation and Geoinformation* 70:51–61.
- Zhang, Y. and J. Guo. 2001. The dynamics of patch density and edge density in forested landscape of Shanxi, China—A case study in Guandishan mountain forest district. *Chinese Journal of Ecology* 20(1):18–21.
- Zhang, Y., H. Zhang and H. Lin. 2014. Improving the impervious surface estimation with combined use of optical and SAR remote sensing images. *Remote Sensing of Environment* 141:155–167.
- Zhang, Z., L. Xu and Q. Liu. 2019. The identification of impervious area from Sentinel-2 imagery using a novel spectral spatial residual convolution neural network. Pages 88–91 in *Proceedings of the 2019 3rd International Conference on Advances in Image Processing*, held in Chengdu, China.
- Zheng, Z., G. Zhou, Y. Wang, Y. Liu, X. Li, X. Wang and L. Jiang. 2013. A novel vehicle detection method with high resolution highway aerial image. *IEEE Journal of Selected Topics in Applied Earth Observations and Remote Sensing* 6(6):2338–2343.

IN-PRESS ARTICLES

- Qinghong Sheng, Rui Ren, Weilan Xu, Hui Xiao, Bo Wang, and Ran Hong. Spinor-based Attitude Determination with Star Sensor Considering Depth.
- Bharath H Aitha and Prakash PS. Digital building height preparation from satellite stereo images.
- Yanfei Zhong, Xiaoman Li, Yu Su, and Richen Ye. Scene Change Detection based on Multi-feature Fusion Latent Dirichlet Allocation Model for High Spatial Resolution Remote Sensing Imagery.
- Wenhui Wan, Jia Wang, Zhaoqin Liu, Man Peng, Yexin Wang, Tianyi Yu, Chuankai Liu, Lichun Li, and Kaichang Di. Enhanced Lunar Topographic mapping using Multiple Stereo Images Taken by Yutu-2 Rover with Changing Illumination Conditions.
- Jiabao Li, M.D, Wei Han, Ruyi Feng, Lizhe Wang, and Fengpeng Li. Unsupervised representation high-resolution remote sensing image scene classification via contrastive learning convolutional neural network.
- Longjie Ye, Wen Xiao, Yehua Sheng, Dong Su, Pengbo Wang, Shan Zhang, Na Zhao, Hui Chen, and Ka Zhang. Gaussian mixture model of ground filtering based on hierarchical curvature constraints for airborne LiDAR point clouds.
- Jonathan B. Thayn, Aaron M. Paque, and Megan C. Maher. Detecting Geo-Positional Bias in Imagery Collected using Small UASs.
- Chengming Ye, Hongfu Li, Ruilong Wei, Lixuan Wang, Tianbo Sui, Wensen Bai, and Saied Pirasteh. Twice Adaptive Intensity Threshold Method for Uneven LiDAR Data to Extract Road Markings.
- Majid Rahimzadegan, Arash Davari, and Ali Sayyadi. Estimating regional soil moisture with synergistic use of AMSR2 and MODIS images.
- Guoqing Zhou, Man Yuan, Xiaozhu Li, Hongjun Sha, Jiasheng Xu, Bo Song, and Feng Wang. Optimal regularization method based on L-curve for solution of the RFM parameters.
- Lisa M. LaForest, Tian Zhou, Seyyed Meghdad Hasheminasab, and Ayman Habib. System Calibration Including Time Delay Estimation for GNSS/INS-Assisted Push-Broom Scanners Onboard UAV Platforms.
- He Yanjun, Xu Jun, Li Jiansong, Peng Hao, Wu Bin. Information Extraction from High-resolution Remote Sensing Images Based on Multi-scale Segmentation and Case-based Reasoning.
- Radhika Ravi, Ayman Habib. Least Squares Adjustment with a Rank-deficient Weight Matrix and its Applicability towards Image/LiDAR Data Processing.
- Saket Gowravaram, Haiyang Chao, Andrew Molthan, Tiebiao Zhao, Pengzhi Tian, Harold Flanagan, Lori Schultz, and Jordan Bell. Spectral Reflectance Estimation of UAS Multispectral Imagery Using Satellite Cross-Calibration Method.
- Toshihiro Sakamoto. Early Classification Method for US Corn and Soybean by Incorporating MODIS-Estimated Phenological Data and Historical Classification Maps in Random-Forest Regression Algorithm.
- Mehdi Khoshboresh-Masouleh and Reza Shah-Hosseini. A Deep Multi-Modal Learning Method and a New RGB-Depth Data Set for Building Roof Extraction.
- Weining Zhu, Zeliang Zhang, Zaiqiao Yang, Shuna Pang, Jiang Chen, Qian Cheng. Spectral Probability Distribution of Closed Connected Water and Remote Sensing Statistical Inference for Yellow Substance.
- Abdullah Kayı, Bülent Bayram, and Dursun Zafer Şeker. The Analysis on the Annual Change of Digital Aerial Camera's IMUs Bore-sight Misalignment.

Optimizing the Segmentation of a High-Resolution Image by Using a Local Scale Parameter

Lei Zhang, Hongchao Liu, Xiaosong Li, and Xinyu Qian

Abstract

Image segmentation is a critical procedure in object-based identification and classification of remote sensing data. However, optimal scale-parameter selection presents a challenge, given the presence of complex landscapes and uncertain feature changes. This study proposes a local optimal segmentation approach that considers both inter-segment heterogeneity and intrasegment homogeneity, uses the standard deviation and local Moran's index to explore each optimal segment across different scale parameters, and combines the optimal segments into a single layer. The optimal segment is measured by using high-spatial-resolution images. Results show that our approach outperforms and generates less error than the global optimal segmentation approach. The variety of land cover types or intrasegment homogeneity leads to segment matching with the geo-objects on different scales. Local optimal segmentation demonstrates sensitivity to land cover discrepancy and provides good performance on cross-scale segmentation.

Introduction

With the increasing availability of very-high-spatial-resolution (VHR) remote sensing images, the high intraclass spectral variability or heterogeneity in VHR severely limits the application of traditional pixel-based approaches (Johnson 2013), as the relations between neighboring pixels are usually ignored. Object-based image analysis uses spatial concepts that effectively incorporate textural, spatial, geometric, contextual, and hierarchical relationships into spectral recognition (Benz *et al.* 2004; Hay and Castilla 2006; X. Zhang *et al.* 2013; Ming *et al.* 2015). Moreover, semantic feature recognition in object-based image analysis using an appropriate segmentation scale is close to human perception for measuring real landscape elements, compared with using the pixel-based approach (Goodchild *et al.* 2007; Cleve *et al.* 2008). The scale parameter is an important factor in geo-object recognition.

The initial and most important step in object-based image analysis is merging image pixels into relatively homogeneous regions called segments, which are taken as basic units for target recognition. Several methods have been developed for segmentation, including edge-based (Li *et al.* 2010) and region-based methods (Benz *et al.* 2004), most of which assign a scale parameter to control the average size and number of

image segments (Duro *et al.* 2012; Myint *et al.* 2011), but they do not provide optimal scale-parameter selection. The optimal scale segments a landscape scene into several meaningful geo-objects; therefore, the scale parameter is closely related to segmentation quality and plays a key role in segmenting remote sensing imagery. An inappropriate scale can lead to either over- or undersegmentation, which influences object-based classification accuracy (Ming *et al.* 2012). Therefore, the optimal image-segmentation scale maximizes both within-segment homogeneity and between-segments heterogeneity (Espindola *et al.* 2006; Johnson and Xie 2011; Johnson *et al.* 2015) and represents a balance between image over- and undersegmentation.

Selecting an appropriate segmentation scale (a single-scale approach) is an important topic that has received much interest in object-based classification research (Powers *et al.* 2012). Determining the scale parameters can be a time-consuming, subjective, and nonuniversal process, whether using visual analysis alone or shape comparison with either a ground truth or reference digitization (Anders *et al.* 2011). Accordingly, unsupervised approaches without reference objects have been developed to measure the optimal scale. One of the most successful approaches is estimation of scale parameter (ESP), which measures the homogeneity within segments and combines the local variance and its change rates in determining the appropriate segmentation scales (Drăguț *et al.* 2010, 2014). By considering the homogeneity within segments and the heterogeneity between equally treated segments, Johnson and Xie (2011) calculated the area-weighted variance to determine intrasegment homogeneity and used the global Moran's index to express intersegment heterogeneity. Both of these approaches are instances of global optimal segmentation (GOS), which aggregates local parameters to determine one or several optimal scales. The shortcoming of GOS is that it provides appropriate scales among all scales with the most optimal objects but not each object, which means that some objects on an appropriate scale are probably over- or undersegmented. Many types of land cover, such as buildings and bodies of water, may adapt to many different segmented scales (Anders *et al.* 2011; Johnson and Xie 2013).

To overcome the limitations of the single-scale approach, a cross-scale strategy has emerged (multi-scale approach). This strategy aims to combine the optimal segments from multiple scales to form a new segment layer. A simple solution of the multi-scale approach is segment comparison with reference polygons, used with expert knowledge to measure multiple scales for a variety of land cover matches (Myint *et al.* 2011; Anders *et al.* 2011; Johnson *et al.* 2015). This approach is

Lei Zhang, Xiaosong Li, and Xinyu Qian are with the Key Laboratory of Digital Earth Science, Aerospace Information Research Institute, Chinese Academy of Sciences, Beijing, China (lixs@radi.ac.cn).

Hongchao Liu is with the 28th Research Institute of China Electronics Technology Group Corporation, Jiangshu, China.

Contributed by Ribana Roscher, October 20, 2020 (sent for review December 11, 2020; reviewed by Liangpei Zhang, Salahuddin M. Jaber, Peng Li)

Photogrammetric Engineering & Remote Sensing
Vol. 87, No. 7, July 2021, pp. 503–511.
0099-1112/21/503–511

© 2021 American Society for Photogrammetry
and Remote Sensing
doi: 10.14358/PERS.87.7.503

relatively accurate, but time consuming. Johnson (2013) has proposed an unsupervised multi-scale method and applied probability evaluation to determine the optimal segments. A preliminary classification is performed for each multi-scale segment, then a higher probability for the assigned class indicates that a segment is a suitable geo-object; therefore, this method depends on classification accuracy. Another hybrid method is a two-step strategy that performs GOS first and subsequently refines the segments produced with the split-and-merge approach on over- and undersegmentation (Johnson and Xie 2011; X. Zhang *et al.* 2013; Xiao *et al.* 2018; Su 2019). The local optimal segmentation (LOS) method focuses on measuring optimal segments across scales rather than at an optimal scale; it analyzes each hierarchical segment of all scales, so that optimal segments can be on different scales, and combines these segments to produce all optimal segments. One LOS method uses stable local variance across scales to measure optimal segments and merge segments from a variety of scales (L. Zhang *et al.* 2014), but it does not consider intersegment changes. Although improved LOS deals with both intra- and intersegment changes (Shen *et al.* 2019), the intrasegment calculations still use a similar metric as the intersegment ones.

Methods

Rather than the GOS approach, this article proposed a novel unsupervised cross-scale LOS approach. One crucial strategy is that the target of interest is the segment rather than the segmentation scale, which avoids GOS's shortcoming of averaging segment characteristics at each scale. Another strategy is to use two sensitive feature analyses to examine the within-segment homogeneity and between-segments heterogeneity of each segment. The technical framework of the refined method is presented in Figure 1. A segmentation algorithm is initially applied to produce multi-scale segment layers. Afterwards, the standard deviation rate change (ROC) and local Moran's index (LMI) of each segment are calculated to measure within-segment homogeneity and between-segments heterogeneity. The integrated local optimal segmentation index (LOSI) metric—composed of the ROC and LMI—is used to express the goodness of the segmentation. The optimal segments are selected across different scales with LOSI evaluation, then combined into a segmentation layer based on the finest-scale segment boundary.

Multi-Scale Image Segmentation

The fractal net evolution approach of region-based segmentation is a bottom-up technique for growing and merging regions to create compact regions and identify suitable scales (Batz and Schäpe 2000). Each merging is controlled by a heterogeneity threshold or scale parameter (SP) and produces many scale segments (Benz *et al.* 2004). In contrast to the real-world landscape, this image segmentation begins at oversegmentation, then matched segmentation, and finally undersegmentation across the SP range.

Feature Measure of LOS Scale

Optimal segmentation is considered to be high homogeneity within a segment and high heterogeneity among segments. Intersegment heterogeneity and intrasegment homogeneity are both important in measuring optimal segmentation. Therefore, these two metrics need to be combined into a single integrated metric to assess segmentation.

The standard deviation is a common used heterogeneity metric to measure within-segment homogeneity. Given that the upward multi-scale segmentation algorithm gradually merges adjacent segments, segment SD in most cases increases during upscaling, but at different ROCs, which represents the similarity of segments in the nearest scales. Thus, the ROC metric can be more robust than SD for measuring within-segment homogeneity. A minimal ROC indicates that the segments between two successive scales are similar, whereas the

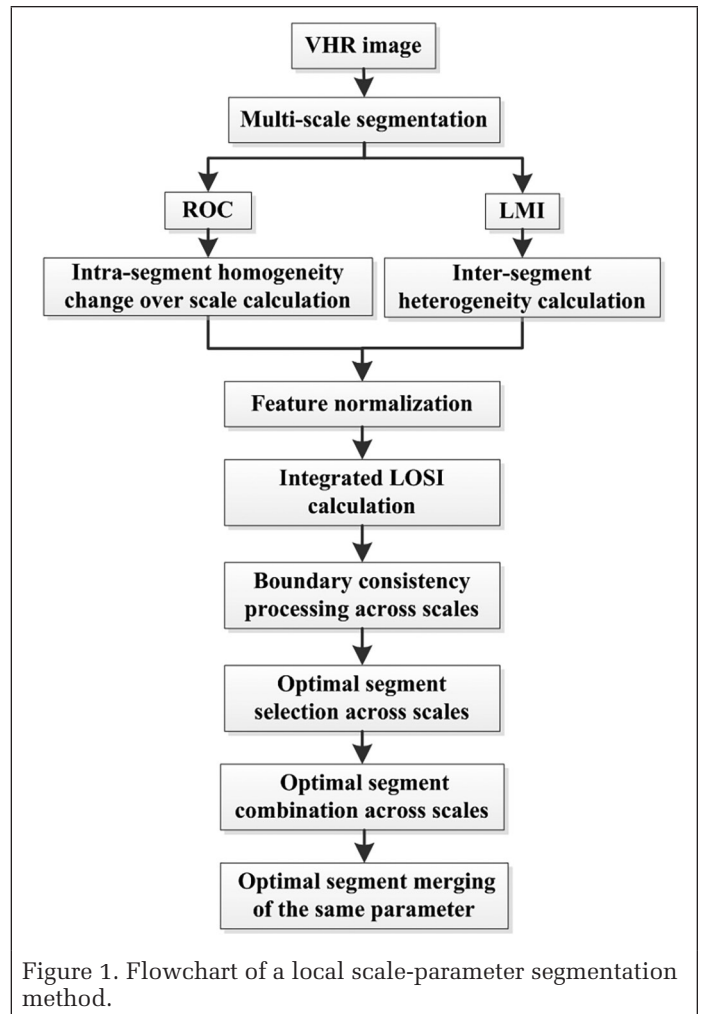


Figure 1. Flowchart of a local scale-parameter segmentation method.

merged segment on the higher scale is considered relatively suitable segmentation. The ROC of the ESP method (Drăguț *et al.* 2010) is calculated as

$$ROC_{ij} = \left| \frac{S_{ij} - S_{j-1}}{S_{j-1}} \right| \quad (1)$$

where ROC_{ij} is the rate of change of the SD of image object i at scale j , S_{ij} is the all-band average pixel SD within object i at segmentation scale j , and S_{j-1} is the all-band average pixel SD within the hierarchical and inherited object $i - 1$ at a finer segmentation scale $j - 1$ (the boundary of object $i - 1$ is inside the boundary of object i).

The intersegment heterogeneity of a segment is considered in measuring the spectral heterogeneity among segments. The global Moran's index was used to calculate between-segments heterogeneity (Johnson and Xie 2011). Since this index equalizes object-neighbor similarity, the local Moran's index was proposed, focusing on a single-segment feature measure to detect its spatial autocorrelation with adjacent segments. A lower LMI indicates a weaker correlation among adjacent segments and higher between-segments heterogeneity, which we take as optimal segmentation. The LMI is computed as

$$LMI_i = \frac{n(x_i - \bar{X})(x_j - \bar{X}) \sum_{j=1}^n w_{i,j}}{\sum_{i=1}^n (x_i - \bar{X})^2} \quad (2)$$

where LMI_i is the LMI at segmentation object i , n is the number of segments in a segmentation scale, x_i and x_j are the band gray values of segments i and j , \bar{X} is the mean of the band gray values of all segments in this segmentation scale, and w_{ij} is the spatial weight value between segments i and j . The weight is set to 1 only if a common boundary between the two segments is present; otherwise, the weight is set to 0.

An integrated index for assessing the goodness of a segmentation scale was built by combining the ROC and LMI. Normalizing the ROC and LMI in terms of the influence of the discrepancy in their magnitudes is necessary; accordingly, these parameters were rescaled to 0 and 1, respectively, using the following formula:

$$F(Y) = \frac{Y - Y_{\min}}{Y_{\max} - Y_{\min}} \quad (3)$$

where Y represents the ROC or LMI and Y_{\max} and Y_{\min} are its maximum and minimum values.

Given that low normalized values ROC_{norm} and LMI_{norm} indicate goodness of the segmentation, an integrated assessment metric of segmentation quality LOSI can be defined as, the sum of ROC_{norm} and LMI_{norm} :

$$LOSI = ROC_{\text{norm}} + LMI_{\text{norm}} \quad (4)$$

ranging from 0 to 2. A low LOSI value indicates both intrasegment homogeneity and intersegment heterogeneity.

Optimal Segment Selection from Different Segmentation Scales

Each segment LOSI at all scales was initially calculated. Afterward, the LOSIs of hierarchical or inherited (vertical) segments across all scales were compared, the segments with the minimum LOSI values across scales were defined as the optimal segments, and all selected optimal segments were combined horizontally to generate a new segmentation layer. Because of boundary inconsistencies of hierarchical (or vertical) segments, the combination of optimal segments from different segmentation scales sometimes led to overlaid or empty boundaries. Therefore, segments at coarser scales were divided by the segment boundaries at the finest scale before LOSI comparison, to ensure seamless combination. After combination, adjacent segments from the same scale that belonged to the same segment before they were divided were merged to generate the final optimal segments.

Experiments

Data and Study Areas

To examine the robustness of the method, we selected a variety of study sites, sensors, and land cover types for analysis. Study site I is a rural area (approximately 20 km²) in Hanzhong, China, whose landscape is simple and patch sizes large (Figure 2). A *WorldView-2* VHR image with a spatial resolution of 1.8 m, in multispectral mode (400–1040 μm) was acquired on April 29, 2010, while vegetation was growing and crops were seeding. Given these characteristics, obvious spectral differences were observed for identifying the land cover of the area. The test area was dominated by cropland, with dispersed built-up patches and bodies of water, as well as needleleaf forest and broadleaf forest. Study site II (approximately 50 km²) is located in a suburb of Beijing, China, whose landscape is relatively complex and patch sizes compact. A similar *Pléiades* VHR image, with a spatial resolution of 2 m, in multispectral mode (430–940 μm), was acquired on August 4, 2015, while vegetation was growing in peak greenness. The dominant landscape is composed of residences, roads, urban vegetation, and cropland.

Image preprocessing was performed with Erdas Imagine 9.0 software, involving image radiation calibration and georegistration.

Initial Segmentation

In this study, a series of successive SPs were created and multi-scale hierarchy segments built by the fractal net evolution approach in eCognition 8.7 software. The SP increment determines the detailed changes in segmentation; this multi-scale segmentation was performed with an equal scale increment of 5 and generated 40 SPs that ranged from 5 to 200. SPs of <5 and >200, respectively, can result in severe over- and undersegmentation for VHR images in study sites. The SP increment of 5 was sufficiently narrow to detect feature changes and measure the appropriate scales across multi-scale segmentation (L. Zhang *et al.* 2014). The other segmentation parameters remained at their default values. According to previous experience in land-surface segmentation, the weights for spectrum and shape homogeneity were set to 0.9 and 0.1, respectively, and the weights for each band were set at an equal value, with the same for smoothness and compactness.

Optimal Segment Measure

The LOSIs of each multi-scale segment were calculated in eCognition; these segments were then inputted into ArcGIS. Based on the finest segmentation layer, the boundaries of the multi-scale overlay were intersected for the coarse segmentation layer. The Python ArcPy module was used to read the processed segment attributes. The segments with the minimum LOSI values across scale rows, and their relevant segmentation scales, were selected, meaning those segments that maintain both higher intrasegment homogeneity and intersegment heterogeneity. A unique identification ID number was generated in a new attribute field. These IDs were selected to produce an optimal segmentation layer, and finally segments with the same LOSI were merged.

Segmentation Quality Evaluation

The reference polygons were selected to overlay spatially on the segments to measure boundary fitness. The reference samples were randomly distributed, and corresponding

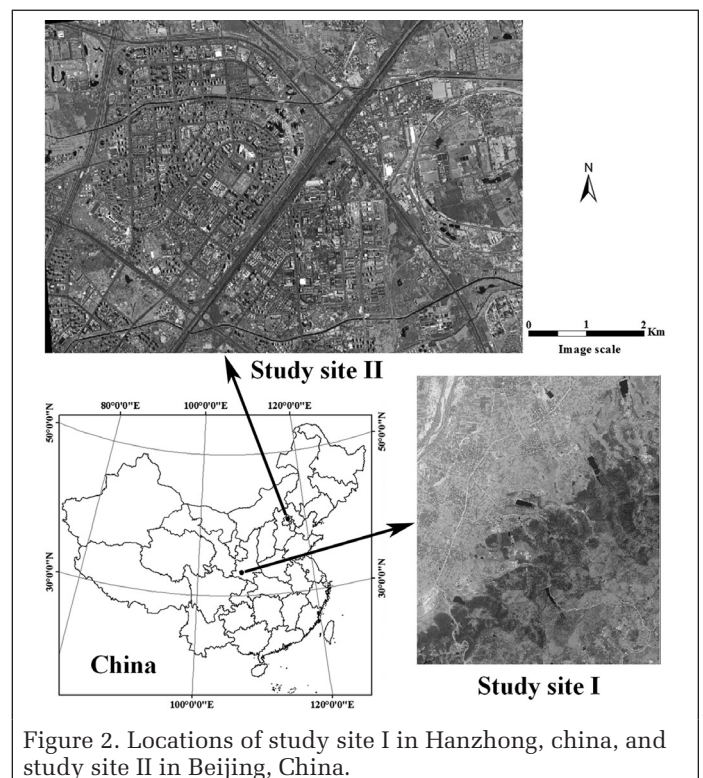


Figure 2. Locations of study site I in Hanzhong, China, and study site II in Beijing, China.

polygons were digitized along a single patch of land cover on the images. As shown in Figure 3, a total of 85 polygons of six land cover types were used to assess segmentation quality in study site I: 19 forest, four shrub, 17 cropland, 14 residence, 13 water, and 18 fallow land. In study site II, 116 random polygons were sampled: 25 forest, 14 grassland, 22 cropland, 37 residence, 11 water, and seven sandy land.

An optimal segment whose intersection area with the reference polygon covered half of either the optimal segment or the reference polygon was considered a matched segment (Clinton *et al.* 2010). The area and number of matched segments and reference polygons were compared to evaluate segmentation quality. As shown in Table 1, seven metrics were used to evaluate segmentation performance (Liu *et al.* 2012; Yang *et al.* 2014). The oversegmentation index, undersegmentation index, and quality corrected rate consider both the geometric matches and the arithmetic relationship between the reference polygons and corresponding segments. The values of these metrics range from 0 to 1, with a lower value indicating better segmentation, but the lowest values of the first two metrics do not indicate

the best segmentation, since they involve only one aspect of over- or undersegmentation; the quality corrected rate, on the other hand, considers both. The potential segmentation error (PSE) and number of segments ratio (NSR) reflect the arithmetic relationship between the reference polygons and corresponding segments and measure the area fitness regardless of the boundary match, ranging from 0 to ∞ . A PSE value of 0 indicates a segment matched to the reference polygon, and a large value implies a significant degree of undersegmentation. An NSR value of 0 indicates a preferred one-to-one relationship between reference polygons and corresponding segments, and a large value indicates that one reference polygon corresponded to many segments, or a significant degree of oversegmentation. The composition OS and US and composition PSE and NSR reflect the Euclidean distances of those four metrics. Specifically, the composition of OS and US is similar to the quality corrected rate but is more sensitive, whereas the composition of PSE and NSR balances the influence of the two metrics.

The results of our LOS approach were compared with the GOS approach of Johnson and Xie (2011; JX) and the ESP method (Drăguț *et al.* 2014), both of which use one or several scales. The JX method uses similar metrics of variance and the global Moran's I to measure intrasegment homogeneity and intersegment heterogeneity. The ESP method considers intrasegment homogeneity only, using the ROC metric. As the ESP method possibly produces several optimal scales, we selected a suitable scale by using the same scale increment as the LOS method.

Results and Discussion

Optimal Segments over the Segmentation Scales

A multi-scale segmentation of the image was performed, and the LOS approach generated a total of 8455 optimal segments in study site I. As shown in Figure 4a, they came from different scales. Most were relatively concentrated between segmentation scales 25 and 55, the numbers of optimized segments from scales coarser than 55 were evenly distributed, and no objects came from scales finer than 25. Despite a relatively large number of segments from finer scales, their areas were not obvious.

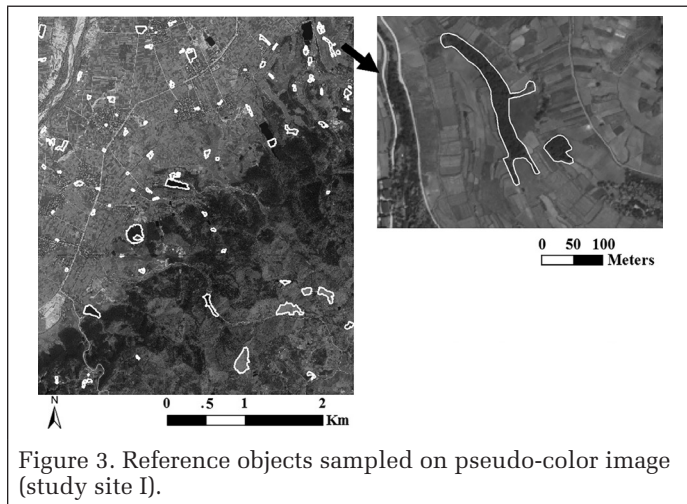


Figure 3. Reference objects sampled on pseudo-color image (study site I).

Table 1. Metrics for error assessment of the optimal segmentation measure.

Metric	Formula	Explanation
Oversegmentation index	$OS = \sum \left(1 - \frac{r_i \cap s_j}{r_i} \right), r_i \in R, s_j \in S$	R and S are the set of reference polygons and matched segments, respectively; r_i and s_j are an arbitrary matched polygon area and segment area, respectively.
Undersegmentation index	$US = \sum \left(1 - \frac{r_i \cap s_j}{s_j} \right), r_i \in R, s_j \in S$	Above
Segmentation error rate	$SER = \sum \left(1 - \frac{r_i \cap s_j}{r_i \cup s_j} \right), r_i \in R, s_j \in S$	Above
Potential segmentation error	$PSE = \frac{\sum s_j - r_i }{\sum r_i}, r_i \in R, s_j \in S$	Above
Number of segments ratio	$NSR = \frac{ m - v }{m}$	m is the number of reference polygons; v is the number of corresponding segments
Composition of OS and US	$ED1 = \sqrt{\frac{OS^2 + US^2}{2}}$	
Composition of PSE and NSR	$ED2 = \sqrt{\frac{PSE^2 + NSR^2}{2}}$	

Their areas over the segmentation scale were nearly similar, which highlights the presence of optimal segments on many scales with varied sizes. The JX and ESP methods identified SP 85 and 75 as the optimal segmentation scales, respectively. Given that the scales were located in the middle range, the two methods produced 1579 and 1963 segments with a similar size, respectively, which is less than what was produced by the LOS approach. The same situation occurred in study site II.

Optimal segments from different scales are presented in Figure 5b. In contrast to land cover, the LOS approach produces optimization segments on coarser scales (which usually have a large segment size) involving land cover types of forest, shrub, and water and on finer scales (which usually have a small segment size) involving residence, cropland, and fallow land. The optimization segments obtained by the LOS approach were not concentrated on a single scale or within a small range of scales. Therefore, using the GOS approach with a single segmentation-scale measure would both over- and undersegment.

Land Cover Effects on Segmentation

The LOS approach shows different effects with a variety of land cover types. Given the relative internal homogeneity of forest and shrub objects, the larger optimal segments matched these geo-objects on coarser scales in study site I (Figure 6a). Meanwhile, the GOS approach generated segments with relatively smaller and equal size, resulting in oversegmentation (Figure 6b–c). By contrast, the geo-objects of residence, cropland, and fallow land demonstrated relative internal heterogeneity; segments measured by the LOS approach fitted on finer scales and produced smaller segments (Figure 6d, 6j), whereas the GOS approach did not result in size changes, thereby leading to undersegmentation (Figure 6e–f, 6k–l). Water showed

no significant difference between GOS and LOS (Figures 6d, 6f, 7e), since its high spectral Euclidean distance from other land covers lead to weak sensitivity to segmentation scale.

The situation is similar in study site II, but the complex and mosaic patches lead to small objects. Therefore, forest (urban vegetation) segmented using the LOS approach showed similar or slightly better performance than using the GOS approach (Figures 6b–c, 7a). By contrast, the segmentation of residence is obviously better than using the JX and ESP methods (Figures 6e–f, 7d), as spectral changes of building rooftop and elevation influence the segmentation. Meanwhile, water illustrates the goodness of segmentation in the LOS method compared to the GOS approach (Figures 6g, 6i, 7h), since the compact-patch landscape causes finer-scale matching in the GOS approach, resulting in oversegmentation of water with intrasegment homogeneity.

The LOS approach explored local segment heterogeneity while considering changes in the features of each segment across all scales. Therefore, LOS segmentation is capable of measuring geo-objects with these land cover discrepancies. By comparison, the GOS approach uses an average feature measure of segment heterogeneity regardless of changes in each segment feature, thereby demonstrating limited sensitivity to land cover types and making this approach suitable for landscapes with consistent intrasegment homogeneity, meaning that most geo-objects of land cover are matched on close segmentation scales.

Local Scale Segmentation Error Analysis

Seven metrics were used to evaluate the quality of segmentation in the two study sites (Tables 2 and 3). The integrated metrics of segmentation error rate, composition of OS and US, and composition of PSE and NSR reveal that the LOS approach achieves high goodness of segmentation, producing average

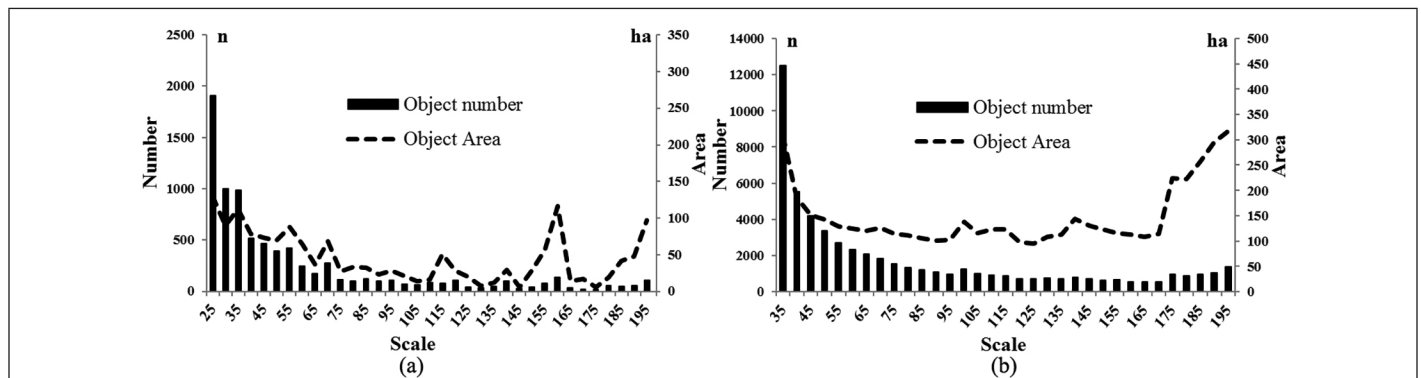


Figure 4. Number and areas of optimal segment occurrence over the segmentation scales: (a) study site I, (b) study site II.

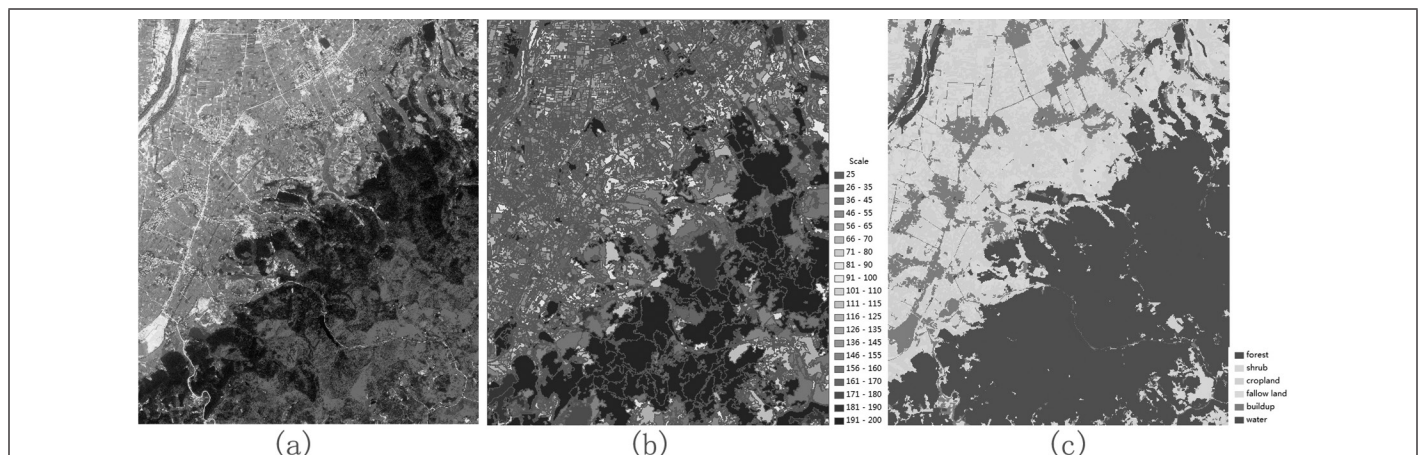


Figure 5. Scale map of optimal segments in study site I. (a) WorldView-2 RGB432 image; (b) scales of optimal segments; (c) land cover map.

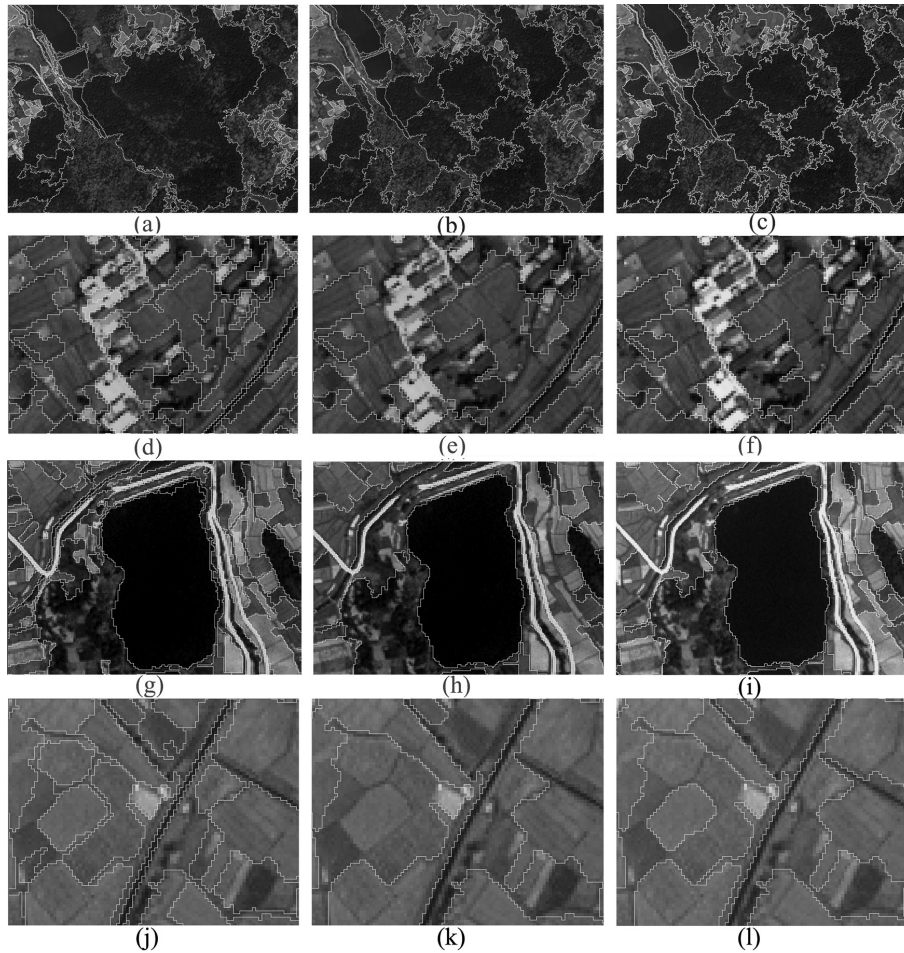


Figure 6. Comparison of segmentation results in study site I. From top to bottom: forest, residence, water, and cropland. (a), (d), (g), (j): local optimal segmentation method; (b), (e), (h), (k): JX method (Johnson and Xie 2011); (c), (f), (i), (l): estimation of scale parameter method.

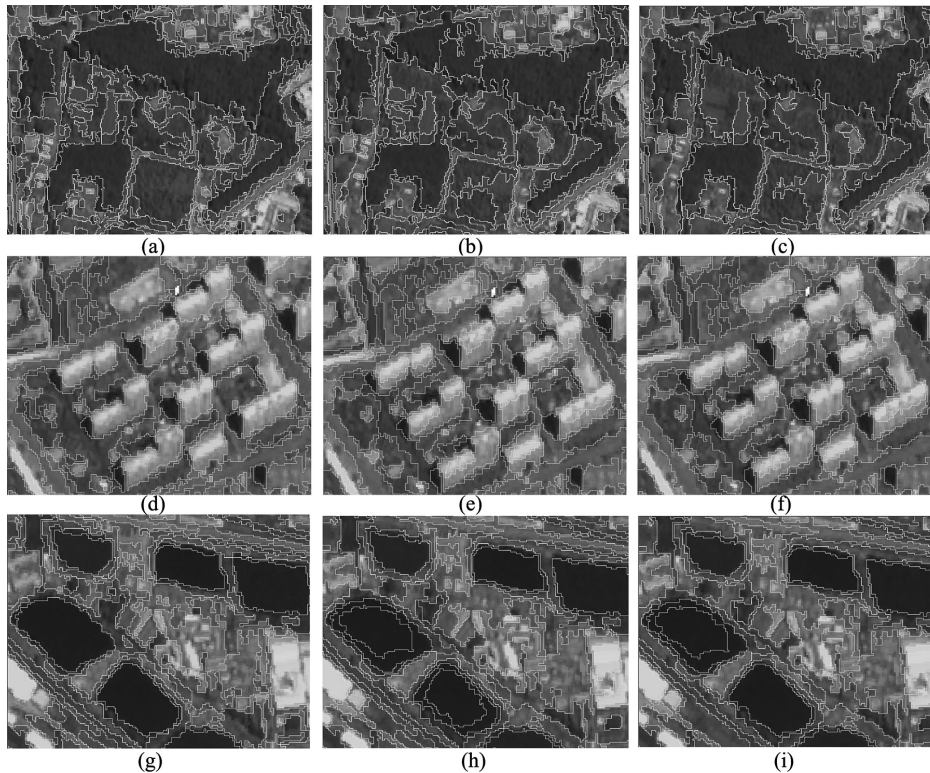


Figure 7. Comparison of segmentation results in study site II. From top to bottom: forest, residence, and water. (a), (d), (g): local optimal segmentation method; (b), (e), (h): JX method (Johnson and Xie 2011); (c), (f), (i): estimation of scale parameter method.

Table 2. Segmentation error comparison in study site I.

Class	Evaluation Metric						
	OS	US	PSE	NSR	SER	ED1	ED2
<u>LOS method</u>							
Forest	0.3903	0.2237	0.0956	1.3158	0.5103	0.3181	0.9329
Shrub	0.1532	0.1521	0.2010	1.0000	0.2786	0.1526	0.7212
Cropland	0.4973	0.1859	0.1032	1.7059	0.5477	0.3754	1.2084
Residence	0.2806	0.4649	1.9886	1.2143	0.6155	0.3840	1.6476
Water	0.2714	0.0665	0.0262	1.2308	0.3072	0.1976	0.8705
Fallow land	0.5053	0.1298	0.0562	1.7778	0.5421	0.3689	1.2577
Total	0.4078	0.2008	0.1321	1.4471	0.5083	0.3214	1.0275
<u>JX method (Johnson and Xie 2011)</u>							
Forest	0.2525	0.7884	5.9695	0.9474	0.8203	0.5854	4.2739
Shrub	0.4379	0.0532	0.0297	1.5000	0.4513	0.3120	1.0609
Cropland	0.1600	0.5194	2.0203	1.0000	0.5549	0.3843	1.5940
Residence	0.1056	0.8222	6.7355	1.0000	0.8203	0.5862	4.8149
Water	0.1902	0.3048	0.4900	1.0769	0.3971	0.2540	0.8366
Fallow land	0.1108	0.4642	1.1589	1.0000	0.4961	0.3375	1.0824
Total	0.1858	0.5572	1.7412	1.0235	0.6172	0.4153	1.4282
<u>ESP method</u>							
Forest	0.0903	0.7267	3.9667	0.0526	0.7632	0.5357	2.8051
Shrub	0.3279	0.0398	0.3649	0.2000	0.3496	0.2350	0.2942
Cropland	0.1018	0.3444	1.1948	0.0000	0.3955	0.2715	0.8449
Residence	0.0895	0.8065	5.6994	0.0000	0.8173	0.5823	4.0301
Water	0.0798	0.1622	0.1329	0.0000	0.2308	0.1513	0.0940
Fallow land	0.0740	0.3733	0.7367	0.0000	0.4155	0.2851	0.5210
Total	0.1013	0.4649	1.0512	0.0000	0.5220	0.3630	0.7433

ED1 = composition of OS and US; ED2 = composition of PSE and NSR; ESP = estimation of scale parameter; LOS = local optimal segmentation; NSR = number of segments ratio; OS = oversegmentation index; PSE = potential segmentation error; SER = segmentation error rate; US = undersegmentation index.

Table 3. Segmentation error comparison in study site II.

Class	Evaluation Metric						
	OS	US	PSE	NSR	SER	ED1	ED2
<u>LOS method</u>							
Forest	0.6947	0.0213	0.7278	2.0000	0.6961	0.4937	1.5049
Grassland	0.7276	0.0000	0.8124	2.6000	0.7276	0.5145	1.9261
Cropland	0.4071	0.0000	0.4605	0.5000	0.4071	0.2879	0.4806
Residence	0.2254	0.0326	0.0327	0.2667	0.2570	0.1812	0.1900
Water	0.0264	0.0186	0.0521	0.0000	0.0450	0.0317	0.0369
Sandy land	0.0493	0.3762	0.8309	0.1667	0.4256	0.3009	0.5992
Total	0.4385	0.0473	0.6480	0.6829	0.4812	0.3404	0.6657
<u>JX method (Johnson and Xie 2011)</u>							
Forest	0.6921	0.0022	0.6732	2.0000	0.6934	0.4894	1.4922
Grassland	0.7516	0.0000	0.8592	3.0000	0.7516	0.5314	2.2066
Cropland	0.7529	0.0080	0.8864	2.7143	0.7532	0.5327	2.0190
Residence	0.3750	0.0301	0.3353	0.5714	0.4050	0.2864	0.4685
Water	0.3051	0.0140	0.4722	0.3333	0.3191	0.2255	0.4087
Sandy land	0.2160	0.1739	0.3255	0.2000	0.3898	0.2756	0.2701
Total	0.6174	0.0172	0.8187	1.5000	0.6328	0.4473	1.2084
<u>ESP method</u>							
Forest	0.6285	0.0138	0.6655	1.6667	0.6413	0.4525	1.2690
Grassland	0.6884	0.0000	0.8412	2.2000	0.6884	0.4868	1.6655
Cropland	0.6729	0.0055	0.8443	1.8571	0.6732	0.4760	1.4425
Residence	0.3000	0.0462	0.2217	0.4286	0.3462	0.2448	0.3412
Water	0.3675	0.0124	0.5066	0.5000	0.3799	0.2686	0.5033
Sandy land	0.0592	0.2518	0.0247	0.0000	0.3110	0.2198	0.0174
Total	0.5406	0.0257	0.7810	1.1250	0.5652	0.3995	0.9684

ED1 = composition of OS and US; ED2 = composition of PSE and NSR; ESP = estimation of scale parameter; LOS = local optimal segmentation; NSR = number of segments ratio; OS = oversegmentation index; PSE = potential segmentation error; SER = segmentation error rate; US = undersegmentation index.

respective values of 18%, 23%, and 28% less than the JX method and 3%, 13%, and 38% less than the ESP method in study site I and 24%, 24%, and 45% less than the JX method and 15%, 15%, and 31% less than the ESP method in study site II.

As indicated by the over- and undersegmentation indices, the LOS approach obtains a lower undersegmentation error but a higher oversegmentation error in study site I, and conversely in study site II; this difference is attributed to the landscape changes over the study sites. A higher oversegmentation index usually means a lower undersegmentation index, and vice versa; therefore, a single metric of over- or undersegmentation index is not robust for evaluating segmentation quality. The lower PSE values indicate that the segment generated by the LOS approach has a size similar to that of the reference polygon. Meanwhile, the NSR metric shows that the LOS approach performs well in study site II but poorly in study site I; this metric is not more effective than NSR in assessing segmentation quality. The variations in land cover influenced the segmentation error: water, given its intrasegment homogeneity, demonstrated better behavior than the other land cover types, accurate measurement, and good fit to the reference polygons. Meanwhile, forest resulted in higher error, given its complex structure and high intrasegment heterogeneity.

Conclusions

Optimizing the segmentation-scale parameter can facilitate geo-object identification and classification. However, assessing the image segmentation quality remains a challenge because of complex landscapes and the absence of standard evaluation methods. This study proposes a local multi-scale measure method that uses the heterogeneous features between and within segments to identify each optimal segment across segmentation scales and evaluate the effects of land cover types on these parameters. The results show that the LOS approach outperforms and exhibits less error than the GOS approach. Land cover types with variable intrasegment homogeneity influence geo-object matching on the segment-scale range, which leads to optimal segments on many scales. Using the GOS approach with a single segmentation-scale measure fails to solve these problems. The LOS approach is sensitive to land cover discrepancies and delivers a cross-scale approach to measure optimal segments over scales and overcome the limitations of a single-scale method. Furthermore, the homogeneity of geo-objects influences the segmentation quality: segments with high intrasegment homogeneity (e.g., water) are better matched to the reference polygon and have less error than segments with low intrasegment homogeneity. However, the algorithm fails to accurately segment obscure boundaries of vegetation landscape, and it also does not know the user purpose in segmentation (e.g., rooftop may indicate a house or a group of houses); therefore, sample training is expected to control segmentation in further studies.

Acknowledgments

This research was funded by the National Key Research and Development Project (2016YFC0500806, 2017YFC0405802) and the Strategic Pilot Science and Technology Program, Chinese Academy of Sciences (XDA19090124).

References

- Anders, N. S., A. C. Seijmonsbergen and W. Bouten. 2011. Segmentation optimization and stratified object-based analysis for semi-automated geomorphological mapping. *Remote Sensing of Environment* 115(12):2976–2985.
- Baatz, M. and A. Schäpe. 2000. Multiresolution segmentation—An optimization approach for high quality multi-scale image segmentation. Pages 12–23 in *Angewandte geographische Informationsverarbeitung XII: Beiträge zum AGIT-Symposium Salzburg 2000*, held in Salzburg, Austria, DD–DD Month 2000. Edited by J. Strobl. City, ST/Country: Publisher.
- Benz, U. C., P. Hofmann, G. Willhauck, I. Lingenfelder and M. Heynen. 2004. Multi-resolution, object-oriented fuzzy analysis of remote sensing data for GIS-ready information. *ISPRS Journal of Photogrammetry and Remote Sensing* 58(3–4):239–258.
- Cleve, C., M. Kelly, F. R. Kearns and M. Mortiz. 2008. Classification of the wildland–urban interface: A comparison of pixel- and object-based classifications using high resolution aerial photography. *Computers, Environment and Urban Systems* 32(4):317–326.
- Clinton, N., A. Holt, J. Scarborough, L. Yan and P. Gong. 2010. Accuracy assessment measures for object-based image segmentation goodness. *Photogrammetric Engineering and Remote Sensing* 76(3):289–299.
- Drăguț, L., O. Csillik, C. Eisank and D. Tiede. 2014. Automated parameterisation for multi-scale image segmentation on multiple layers. *ISPRS Journal of Photogrammetry and Remote Sensing* 88:119–127.
- Drăguț, L., D. Tiede and S. R. Levick. 2010. ESP: A tool to estimate scale parameter for multiresolution image segmentation of remotely sensed data. *International Journal of Geographical Information Science* 24(6):859–871.
- Duro, D. C., S. E. Franklin and M. G. Dubé. 2012. Multi-scale object-based image analysis and feature selection of multi-sensor earth observation imagery using random forests. *International Journal of Remote Sensing* 33(14):4502–4526.
- Espindola, G. M., G. Camara, I. A. Reis, L. S. Bins and A. M. Monteiro. 2006. Parameter selection for region-growing image segmentation algorithms using spatial autocorrelation. *International Journal of Remote Sensing* 27(14):3035–3040.
- Goodchild, M. F., M. Yuan and T. J. Cova. 2007. Towards a general theory of geographic representation in GIS. *International Journal of Geographical Information Science* 21(3):239–260.
- Hay, G. J. and G. Castilla. 2006. Object-based image analysis: Strengths, weaknesses, opportunities and threats (SWOT). *The International Archives of Photogrammetry, Remote Sensing and Spatial Information Sciences* 36(4):PP–PP.
- Johnson, B. A. 2013. High-resolution urban land-cover classification using a competitive multi-scale object-based approach. *Remote Sensing Letters* 4(2):131–140.
- Johnson, B. A., M. Bragais, I. Endo, D. B. Magcale-Macandog and P.B.M. Macandog. 2015. Image segmentation parameter optimization considering within- and between-segment heterogeneity at multiple scale levels: Test case for mapping residential areas using Landsat imagery. *ISPRS International Journal of Geo-Information* 4(4):2292–2305.
- Johnson, B. and Z. Xie. 2011. Unsupervised image segmentation evaluation and refinement using a multi-scale approach. *ISPRS Journal of Photogrammetry and Remote Sensing* 66(4):473–483.
- Johnson, B. and Z. Xie. 2013. Classifying a high resolution image of an urban area using super-object information. *ISPRS Journal of Photogrammetry and Remote Sensing* 83:40–49.
- Li, D., G. Zhang, Z. Wu and L. Yi. 2010. An edge embedded marker-based watershed algorithm for high spatial resolution remote sensing image segmentation. *IEEE Transactions on Image Processing* 19(10):2781–2787.
- Liu Y., L. Bian, Y. Meng, H. Wang, S. Zhang, Y. Yang, X. Shao and B. Wang. 2012. Discrepancy measures for selecting optimal combination of parameter values in object-based image analysis. *ISPRS Journal of Photogrammetry and Remote Sensing* 68:144–156.

- Ming, D., T. Ci, H. Cai, L. Li, C. Qiao and J. Du. 2012. Semivariogram-based spatial bandwidth selection for remote sensing image segmentation with mean-shift algorithm. *IEEE Geoscience and Remote Sensing Letters* 9(5):813–817.
- Ming, D., J. Li, J. Wang and M. Zhang. 2015. Scale parameter selection by spatial statistics for GeOBIA: Using mean-shift based multi-scale segmentation as an example. *ISPRS Journal of Photogrammetry and Remote Sensing* 106:28–41.
- Myint, S. W., P. Gober, A. Brazel, S. Grossman-Clarke and Q. Weng. 2011. Per-pixel vs. object-based classification of urban land cover extraction using high spatial resolution imagery. *Remote Sensing of Environment* 115(5):1145–1161.
- Powers, R. P., G. J. Hay and G. Chen. 2012. How wetland type and area differ through scale: A GEOBIA case study in Alberta's Boreal Plains. *Remote Sensing of Environment* 117:135–145.
- Shen Y., J. Chen, L. Xiao and D. Pan. 2019. Optimizing multiscale segmentation with local spectral heterogeneity measure for high resolution remote sensing images. *ISPRS Journal of Photogrammetry and Remote Sensing* 157:13–25.
- Su, T. and S. Zhang. 2017. Local and global evaluation for remote sensing image segmentation. *ISPRS Journal of Photogrammetry and Remote Sensing* 130:256–276.
- Xiao, P., X. Zhang, H. Zhang, R. Hu and X. Feng. 2018. Multiscale optimized segmentation of urban green cover in high resolution remote sensing image. *Remote Sensing* 10(11):1813.
- Yang, J., P. Li and Y. He. 2014. A multi-band approach to unsupervised scale parameter selection for multi-scale image segmentation. *ISPRS Journal of Photogrammetry and Remote Sensing* 94:13–24.
- Zhang, L., K. Jia, X. Li, Q. Yuan and X. Zhao. 2014. Multi-scale segmentation approach for object-based land-cover classification using high-resolution imagery. *Remote Sensing Letters* 5(1):73–82.
- Zhang, X., P. Xiao, X. Feng, L. Feng and N. Ye. 2015. Toward evaluating multiscale segmentations of high spatial resolution remote sensing images. *IEEE Transactions on Geoscience and Remote Sensing* 53(7):3694–3706.
- Zhang, X., P. Xiao, X. Song and J. She. 2013. Boundary-constrained multi-scale segmentation method for remote sensing images. *ISPRS Journal of Photogrammetry and Remote Sensing* 78:15–25.

Call for Submissions

Remote Sensing Monitoring for Urban Environment

Photogrammetric Engineering and Remote Sensing (PE&RS) is seeking submissions for a special issue on Remote Sensing Monitoring for Urban Environment.

Urban remote sensing provides images with multiple spatio-temporal-spectral attributes, which can provide qualitative, quantitative, dynamic and comprehensive information and support for urban environmental monitoring and evaluation, and serve urban planning and management, ecological environment protection. In recent decades, global urban areas have been rapidly expanding, especially in developing countries. Rapid urbanization, along with manufacturing industries and large number of vehicles has resulted in serious environmental problems, called “urban diseases”, including increased vulnerability to natural hazards, natural vegetation cover decline and arable land loss, urban heat islands, air pollution, hydrological circle alteration and biotic homogenization. Urban ecosystems are strongly influenced by anthropogenic activities. Considering this, this special issue of PE&RS is aimed at reporting novel studies on exploiting remote sensing big data to monitor and improve urban environment, and showing the potential of remote sensing in developing sustainable cities, including but not limited to:

- Urban thermal-environment remote sensing
- Remote sensing image acquisition and processing for urban environment
- Remote sensing dynamic monitoring of urban expansion
- Remote sensing change detection of urbanization
- Remote sensing retrieval of urban ecological environment
- Remote sensing evaluation of urban human settlements
- Urban sustainability indicators and assessment
- Urban environmental monitoring

Papers must be original contributions, not previously published or submitted to other journals. Submissions based on previous published or submitted conference papers may be considered provided they are considerably improved and extended. Papers must follow the instructions for authors at <http://asprs-pers.edmgr.com/>.

Important Dates (Tentative)

- March 1, 2021—Submission system opening
- September 31, 2021—Submission system closing
- Planned publication date is December 2021
- Submit your manuscript to <http://asprs-pers.edmgr.com/> by September 31, 2021.

Guest Editors

Zhenfeng Shao, Wuhan University, China

Prof. Zhenfeng Shao, Professor at the State Key Laboratory of Information Engineering in Surveying, Mapping and Remote Sensing, Wuhan University, China. His research interests include urban remote sensing. He is now an associate editor of Email: shaozhenfeng@whu.edu.cn.

Orhan Altan, Istanbul Technical University, Turkey

Prof. Orhan ALTAN, Professor at the Department of Geomatics Engineering, Istanbul Technical University, Turkey. He is Past President and Honorary Member of ISPRS, Honorary Member of Science Academy. He has published more than 200 scientific papers in scientific journals and conferences, and editor or co-editor of more than 20 international books. Email: oaltan@itu.edu.tr.

J.L.van Genderen, University of Twente, Netherlands

Professor J.L.van Genderen, Professor at the Department of Earth Observation Science, Faculty of Geo-information Science and Earth Observation(ITC),University of Twente, Netherlands, he is an Associate Editor of the international journal GEO Spatial Information Science. His research interests include urban remote sensing and new technologies for urban management. Email: Genderen@alumni.itc.nl.

Review of Spectral Indices for Urban Remote Sensing

Akib Javed, Qimin Cheng, Hao Peng, Orhan Altan, Yan Li, Iffat Ara, Enamul Huq, Yeamin Ali, and Nayyer Saleem

Abstract

Urban spectral indices have made promising improvements in the last two decades in urban land use land cover studies through mapping, estimation, change detection, time-series analyzing, urban dynamics, monitoring, modeling, and so on. Remote sensing spectral indices are unsupervised, unbiased, rapid, scalable, and quantitative in information extraction. Hence, we aimed to summarize the most relevant urban spectral indices by focusing on multispectral, thermal, and nighttime lights indices. We use the search terms “urban index”, “built-up index”, “normalized difference built-up area (NDBI)”, “impervious surface index”, and “spectral urban index” to collect relevant literature from the “Web of Science Core Collection” database. We found that all urban spectral indices developed since 2003, except NDBI. This review will help understand the applications of urban spectral indices, the selection of indices based on available spectral bands, and their merits and demerits.

Introduction

Background

In urban remote sensing (RS), the last two decades produced numerous promising urban spectral indices for urban land use land cover (LULC) studies. RS applications are now fundamental, from urban planning to urban governance. Old maps and field surveys are outdated and rapidly replaced by RS images for urban studies (Li *et al.* 2018). From the mapping of a single city (Shao *et al.* 2019, Zhang *et al.* 2021), regional (Lyimo *et al.* 2020) to global land use mapping (Duan *et al.* 2015; Liu *et al.* 2018; Zhang and Seto 2011) are now possible with RS technology.

Earlier Remote Sensing Urban Studies

Earlier, RS or urban studies were focused on urban area mapping, urban land use classification, urban-rural fringe study,

Akib Javed, Hao Peng, Enamul Huq, and Nayyer Saleem are with the State Key Laboratory of Information Engineering in Surveying, Mapping and Remote Sensing, Wuhan University, Wuhan, 430079 Hubei, China (akibjaved@whu.edu.cn).

Qimin Cheng is with the School of Electronics Information and Communications, Huazhong University of Science and Technology, Wuhan, Hubei 430074, China.

Orhan Altan is with the Department of Geomatics, Istanbul Technical University, Istanbul, Turkey.

Yan Li is with the Inner Mongolia Electronic Information Vocational Technical College, Hohhot 010070, China.

Iffat Ara is with the Department of Environmental Science and Geography, Islamic University, Kushtia 7003, Bangladesh.

Yeamin Ali is with DanChurchAid, Cox’s Bazar, 4700, Bangladesh.

Contributed by Zhenfeng Shao, October 1, 2020 (sent for review November 16, 2020; reviewed by Bin Hu, Nana Yaw Danquah Twumasi, Neema S S Sumari)

and urban heat islands (UHI) (Li *et al.* 2021, Shao *et al.* 2021). In the earliest quantitative techniques in urban change detection studies using RS images, urban and nonurban areas were delineated using the boundaries of vegetated and non-vegetated areas. This study also introduced the false-color composite by replacing earlier grayscale images (Howarth and Boasson 1983).

In digital image classification techniques, the importance of spectral characteristics (Digirolamo and Davies 1994; Vachon and West 1992) and spectral signature (Dekker *et al.* 1992; Surin and Ladner 1995) were also increased among other RS researchers since then.

In the beginning, band ratios were popular first, followed by normalized urban indices like normalized difference vegetation index (NDVI). Colwell (1974) first used a band ratio of near-infrared (NIR) and red bands for vegetation study from the Landsat multispectral scanner (MSS) sensor. Later, this ratio was popularized as a simple ratio (SR) (Baret *et al.* 1989; Sellers 1987). Afterward, the SR was normalized as vegetation index (VI) (Rouse Jr *et al.* 1974) and popularized later on as NDVI (Huete 1988). Unlike vegetation, urban indices primarily focused on short wave infrared (SWIR) and NIR spectral regions, where built-up areas reflect more in SWIR electromagnetic spectrum regions than the NIR region. Using this spectral information, urban index (UI) is one of the earlier examples of an urban index in urban RS studies (Kawamura *et al.* 1997).

Urban Indexing with Multispectral RS

Multispectral RS data sets have popularity among urban researchers because it has a medium spatial resolution, shorter temporal resolution, spectral resolution with visible NIR, SWIR, and thermal bands, available global coverage, easy accessibility, and so on. Among the major RS data sources, Landsat missions have the most extended stable historical archive of freely available remote sensing instruments (RSI) with global coverage among all the multispectral sensors, attracting researchers for time series analyses. *Sentinel-2A/B* also has a better spatial resolution than Landsat, with some visible bands up to 10 meters. On the other hand, moderate resolution imaging spectroradiometer (MODIS) has extensive coverage for regional studies but a very short temporal gap, attracting many regional studies with low spatial resolution requirements. A visible/infrared intelligent spectrometer (VIRIS) has better spectral resolution but is limited spatiotemporally. In this way, each RS sensor has its merits and demerits. Researchers have to design their research according to their data availability.

Urban Indexing with Cloud Computing

Computing platforms further widens the possibilities of many RS studies, including urban studies. Primarily, Google Earth Engine (GEE), enabling users to study large numbers of RSI (Gorelick *et al.* 2017; Shelestov *et al.* 2017) very quickly.

Photogrammetric Engineering & Remote Sensing
Vol. 87, No. 7, July 2021, pp. 513–524.
0099-1112/21/513–524

© 2021 American Society for Photogrammetry
and Remote Sensing
doi: 10.14358/PERS.87.7.513

Furthermore, it increased computational capacity and sharing capability in many folds among researchers. These events triggered an RS big data study in spatial mapping, change detection, and time series analysis.

Indexing Urban Areas

Spectral Indexing for Urban Studies

Spectral indexing allows quantitative enhancement of RS information. Indexing facilitates urban RS studies by fusing multiple data sets, extracting objective information, automating image processing, avoiding researcher bias, easing scaling-up operation, bring robustness in RSI data analysis, and overall speeding-up of urban study.

Prior, unlike vegetation and water indexing, urban spectral indexing was uncommon. Almost all the indices were developed after 2000. Initially, urban indexing focused on broad urban characteristics where the concept of urban was considered a densely populated place. Subsequent, indices focused only on the infrastructural characteristics of an urban area.

Finally, the built-up area's impervious characteristics were emphasized in indexing as an urban indicator. Both the built-up area and impervious surface area (ISA) have spectral similarity with bare soil. Therefore, most of the indices with built-up areas consider it as a limitation. On the contrary, a bare soil area is pervious and, by definition, opposite of ISA. Therefore, researchers emphasized much in solving classification problems between bare soil area and ISA.

Index-Based Urban Classification

There are many urban area extraction methods in the RS domain. Spectral indices are one of them in pixel-level classifications. It is easy to apply in broad arrays of RS application than a traditional classification algorithm (Pan *et al.* 2010). Spectral indices provide a probability output with continuous value, where classifiers provide discrete values (Xie *et al.* 2008) in image classification. Therefore, in quantitative manipulations, indices are popular among researchers. Even in subpixel level classifications, indices are popular with spectral mixing analysis to derive endmembers (Li 2020).

Supervised image classification required sampling as training data and could not replicate across geographical variations accurately. In contrast, indexing-based classification is an unsupervised method, easy to replicate globally, can deal with big data sources, and has robust characteristics (Datta *et al.* 2008; Olaode *et al.* 2014). Therefore, spectral indices-based image classifications are becoming popular with various spatiotemporal studies due to their nonreliability on training data (Phalke and Özdoğan 2018).

Classification Problems in Urban Indexing

Spectral indices are useful for studying RSI, measuring LULC classes, and detecting changes of LULC over time. Urban land use classes are different from the rest of the land cover types where it is human-made land use, unlike other natural land covers (Meyer and Turner 1994). Secondly, urban areas are highly heterogeneous, fragmented, and mixed with other LULCs. Thirdly, its spectral signature is confusing where bright pixels have similarity with dry bare soil and dark pixels have high similarity with shadow, wet bare land, and shallow waterbodies.

Often urban ISA extraction requires removing nonurban classes (Khan *et al.* 2017). Furthermore, other land cover classes' spectral indexing can also refine urban classification accuracy by removing cloud coverage (Gomez-Chova *et al.* 2017), waterbodies (Deng and Wu 2012), and bare soil. Besides, urban built-up areas and bare soil areas have difficult classification problems in RS studies with existing multi-spectral data sets. We present an overview of spectral indices where few indices dealt with this problem. In addition to LULC studies, numerous environmental studies used urban spectral indices.

Spatial Resolution in Urban Studies

Urban land use is a mixed area with ISA, vegetation, waterbodies, and bare soil. Coarse spatial resolution RS data such as MODIS will have very skewed results. Higher spatial resolution, such as medium resolution RS, can effectively classify RS images into limited numbers of classes (Ridd 2007). Medium RS images with 10–30 meters spatial resolution are sufficient for mapping urban features, but not enough to map urban heterogeneity. Hence, Landsat missions or *Sentinel's 2A/B* missions are sufficient for urban study with limited accuracy.

Along with land cover mapping (Hester *et al.* 2010; Jawak and Luis 2013; Parent *et al.* 2015), high-resolution RS data have also been used for specific urban features studies, such as urban vegetation (Chikr El-Mezouar 2011; Nichol and Lee 2006), urban water stress (Wu *et al.* 2018), urban landscape evapotranspiration (Nouri *et al.* 2014), the building detection method (Qin and Fang 2014), the earthquake affected building collapse (Liu and Li 2019), and so on. Although, in this spatial resolution, there are several accuracy issues because of mixed pixel problems. RS methods, such as spectral unmixing, can further enhance accuracy at the subpixel level.

Simple to Complex Urban Indexing

Generally, complexity in index formulation is positively related to accuracy and negatively related to robustness. Simple indices are robust to use but lack accuracy, whereas complex indices are more accurate but require more RS information. Often, this lack of RS information (i.e., spectral bands) makes complex indices unusable.

For example, vegetation temperature light index (VTLI) (Hao *et al.* 2015) and modified normalized difference impervious surface index (MNDISI_{LIU}) (Liu *et al.* 2013) both provide higher accuracy in comparison with simple normalized difference built-up index (NDBI) (Zha *et al.* 2003) but require multi-spectral, thermal, and nighttime lights (NTL) RS information to be formulated. While studying time series analysis, researchers were trying to use simpler indices so that these indices are calculatable with available RS data (Capolupo *et al.* 2020).

Significance of the Study

Among major LULC classes, vegetation has a couple of reviews articles with spectral indices (Kobayashi *et al.* 2019; Xue and Su 2017). On the contrary, there is a shortage of review works on urban spectral indexing. Besides, there are many urban indices developed and published in the last two decades. This review will try to compile most of the important spectral indices used in urban studies and categorize them. We used the “Web of Science” database and searched for terms “urban index”, “urban spectral index”, “normalized difference built-up index”, “impervious surface area”, and a combination of these terms, which found a total of 1447 articles within the English language (Figure 1).

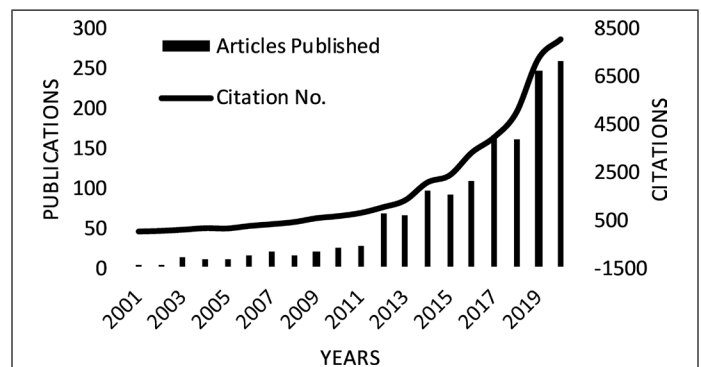


Figure 1. Bar graph shows yearly publications count and the line graph shows citation count for urban-related spectral indices. The search was conducted on 9 January 2021. Only article literature are included.

This review summarizes the most used, popular, and important urban spectral indices from multispectral, thermal, and nighttime lights RSI. We also classify them according to their band usage.

In those segments, we discuss their applicability, merits and demerits, and their band equations. This study will support researchers studying urban indexing, spectral indexing, and urban spectral indices. It will assist in understanding the overall picture of the topic and development phases of urban indices.

Spectral Urban Indexing

Urban indexing began with infrared spectral bands. These earlier indices were inefficient and built-up areas were mixed with bare soil. Therefore, new indices were developed using different bands, such as panchromatic (PAN), coastal, thermal bands, etc. Later on, complex transformations such as tasselled cap transformation (TCT), principal component analysis (PCA), and NTL were introduced to enhance accuracy. However, the focus shifted from built-up areas to the impervious surface area. Moreover, complex and multi-source indices were developed to increase accuracy. Most of the recent indices focus on enhancing the ISA and reducing bare soil and pervious surface areas.

There are numerous active RS sensors available and more currently under development. We divided these sections based on the spectral range of the bands. To simplify the discussion, we used the Landsat mission naming style instead of wavelength values.

Indices with Visible and Near-Infrared Bands

This section includes a few important urban spectral indices that used spectral bands ranging from 400–900 nm (see Table 1). Sensors with 400 to 900 nanometers (nm) of wavelength are the most common among earth imaging RS sensors. Satellite, airborne, and even unmanned aerial vehicles, almost all RS imaging sensors have this range of wavelength.

Usually, urban spectral indexing is popular with SWIR bands and early urban indices used at least one SWIR band. Estoque and Murayama (2015) argued that, besides urban built-up areas, dried vegetation also showed higher reflectance in the SWIR₁ band region. Therefore, they proposed two built-up indices using visible bands only. They are visible red near-infrared built-up index ($V_{rNIR-BI}$) and visible green near-infrared built-up index ($V_{gNIR-BI}$). Among these two, $V_{rNIR-BI}$ works better than the $V_{gNIR-BI}$ index, and these are best in classifying ISA and dry vegetated areas, but not good at classifying ISA from bare soil.

Different versions of NDBI have been used to generate a newer binary built-up index (BBI) proposed using visible bands (Bai *et al.* 2020). Firstly, two binary NDBI indices $NDBI_{Blue-Green}$ and $NDBI_{Red-Green}$ calculated using the equation in Table 1. Secondly, BBI was calculated by adding all the positive binary values of those indices. Binary indices were indicated using the “b” at the subscript of the respective indices. Like NDBI (Zha *et al.* 2003), BBI does not distinguish between ISA and bare soil.

Another multi-indexed combinational biophysical composition index (CBCI) (Zhang *et al.* 2018) used two indices named modified bare soil index (MBSI) (Zhang *et al.* 2018) and optimized soil-adjusted vegetation index (OSAVI) (Moosavi *et al.* 2016; Rondeaux *et al.* 1996). MBSI is a soil index, and OSAVI is a vegetation index formulated as follows. Unlike BBI, CBCI has good separability between ISA and bare soil. In CBCI, “A” is a correctional factor that depends on soil characteristics, and its value is 0.51. “A” introduced

to enhance MBSI over OSAVI. The strength of CBCI is that it can distinguish ISA when mixed with vegetation areas but is not quite good with soil areas.

Bai *et al.* (2020) also argued that removing waterbodies can significantly increase the ISA extraction accuracy. Like biophysical component index (BCI) and automated built-up extraction index, they proposed water extracted NDBI (WE-NDBI), which was formulated using multispectral *GF-1* wide-field view (WFV) sensor data sets. It required some logical functions to apply on $NDBI_{GF1}$ to keep those values only where water values are less than WE-NDVI. The study claimed that WE-NDBI significantly increases the accuracy in comparison to other NDBI indices. However, it does not separate bare soil from ISA.

Feature space is also popular with bare soil sensitive ISA indexing with visible bands and perpendicular indices. Tian *et al.* (2018) used feature spaces of blue and NIR bands to propose a reference line equation named perpendicular impervious surface index (PISI), which separates ISA from bare soil. Though using only two bands, it has higher accuracy in separating the impervious area from the bare soil area up to this point in time. PISI performed significantly better than the BCI and NDBI indices. It applies to most optical sensors due to the usage of blue and NIR bands only. The example of PISI can be replicated in numerous other RS applications. Similar to BBI, PISI increases the separability between ISA and bare soil and between ISA and vegetation areas.

Indices with Visible, NIR, and SWIR Bands

This section includes all the urban spectral indices that used visible, NIR, and SWIR bands. We exclude indices with PAN bands and include them in the following section (see Table 2). The first urban spectral index is named UI, proposed by Kawamura *et al.* (1997). A similar built-up index, which was the most used urban index, is the NDBI developed by Zha *et al.* (2003). Here, the authors attempted to develop a binary index using NDBI, where RSI will be classified as an urban and nonurban area. All positive NDBI values were considered as urban areas.

Despite the importance of distinguishing ISA from bare soil, innovative indices were developed slowly. For example, Jieli *et al.* (2010) worked on a new built-up index (NBI), which amplified built-up and bare land compared to NDBI. NBI is

Table 1. List of urban indices with spectral wavelength range 400–900 nm.

SL	Equation	EQN	Reference
1	$V_{rNIR-BI} = (Red - NIR)/(Red + NIR)$	(1)	Estoque and Murayama 2015
2	$V_{gNIR-BI} = (Green - NIR)/(Green + NIR)$	(2)	
	$BBI = NDBI_{Blue-Green,b} + NDBI_{Red-Green,b}$		
3	where, $NDBI_{Blue-Green} = (Blue - Green)/(Blue + Green)$, $NDBI_{Red-Green} = (Red - Green)/(Red + Green)$	(3)	Bai <i>et al.</i> 2020
	$CBCI = (A + 1) * MBSI - OSAVI + A$		
4	where, $MBSI = ((Red + Green) * 2)/((Red + Green) - 2)$, $OSAVI = (NIR - RED)/(NIR + RED + 0.16)$ and $A = 0.51$	(4)	Zhang <i>et al.</i> 2018
5	$WE-NDBI = \begin{cases} NDBI_{GF1} & (NDBI_{GF1} \leq W) \\ 0 & (NDBI_{GF1} > W) \end{cases}$ where, $NDBI_{GF1} = (Red - Green)/(Red + Green)$	(5)	Bai <i>et al.</i> 2020
6	$PISI = 0.8192 * Blue - 0.5735 * NIR + 0.0750$	(6)	Tian <i>et al.</i> 2018

SL = ; EQN = equation number.

producing an all positive urban index, but not as a normalized form. In NBI, the ordering of values is like bare land > built-up > other land classes from high to low. Using Landsat thematic mapper (TM) sensor data, a threshold value of 45–110 was used to extract the study's built-up area with 90% accuracy.

In pursuit of further development of NDBI, Waqar *et al.* (2012) proposed two new urban indices. They are normalized built-up area index (NBAI) and band ratio for the built-up area (BRBA). Here, NBAI used both of the SWIR regions where BRBA used only one SWIR band. The study claimed to increase built-up extraction accuracy by 10–13% compared to NDBI and NBI. All these indices could not separate the built-up areas from bare land areas.

Bouzekri *et al.* (2015) proposed a new built-up area extraction index based on *Landsat 8* and adding arithmetic constant in the nominator, where $L = 0.3$, is an arithmetic constant. To

further enhance the urban land use classification accuracy, Kaimaris and Patias (2016) proposed a novel built-up index (BUI). Though innovative, BUI suffered from omission error. In BUI accuracy assessment, many built-up areas consider the non-built-up area. BUI also classified built-up and bare soil as one single class. Moreover, earlier urban researchers did not intend to differ between built-up and bare soil. NDBI never claimed to be an index of only urban rather than an indicator of the urban area showing built-up areas and bare lands.

Capolupo *et al.* (2020) used SWIR1 and red bands to introduce the SwiRed index. SWIR bands were the most used band regions in urban indexing practices. It is used to extract the built-up area in an automated land cover information extracting algorithm. Here, a threshold of $0 < \text{value} < 0.22$ is used to classify built-up areas. SwiRed applies to temporal application with all the Landsat missions with SWIR bands.

Table 2. List of urban indices with spectral wavelength range 400–2500 nm excluding panchromatic (PAN) bands.

SL	Equation	EQN	Reference
1	$UI = ((SWIR2 - NIR) / (SWIR2 + NIR) + 1) \times 100$	(7)	Kawamura <i>et al.</i> 1997
2	$NDBI = (SWIR1 - NIR) / (SWIR1 + NIR)$	(8)	Zha <i>et al.</i> 2003
3	$NBI = (Red \times SWIR1) / NIR$	(9)	Jieli <i>et al.</i> 2010
4	$NBAI = (SWIR2 - SWIR1 / Green) / (SWIR2 + SWIR1 / Green)$	(10)	Waqar <i>et al.</i> 2012
5	$BRBA = Red / SWIR1$	(11)	
6	$BAEI = (Red + L) / (Green + SWIR1)$	(12)	Bouzekri <i>et al.</i> 2015
7	$BUI = 2 * \frac{(Red * SWIR2) - (SWIR1 * SWIR2)}{(Red + SWIR1) * (SWIR1 + SWIR2)}$	(13)	Kaimaris and Patias 2016
8	$SwiRed = (SWIR1 - Red) / (SWIR1 + Red)$	(14)	Capolupo <i>et al.</i> 2020
9	$ENDISI = \frac{Blue - \alpha (SWIR1 / SWIR2 + MNDWI^2)}{Blue + \alpha (SWIR1 / SWIR2 + MNDWI^2)}$ where, $\alpha = \frac{2 * Blue_{Mean}}{\left(\frac{SWIR1}{SWIR2}\right)_{Mean} + (MNDWI^2)_{Mean}}$	(15)	Chen <i>et al.</i> 2019
10	$BU_b = NDBI_b - NDVI_b$	(16)	Zha <i>et al.</i> 2003
11	$INDBI = NDBI - NDVI$, INDBI, also known as BUC	(17)	He <i>et al.</i> 2010
12	$IBI = \frac{[NDBI - (SAVI + MNDWI) / 2]}{[NDBI + (SAVI + MNDWI) / 2]}$	(18)	Xu 2008
13	$VIBI = NDVI / (NDVI - NDBI)$	(19)	Stathakis <i>et al.</i> 2012
14	$BCI = \frac{(H + L) / 2 - V}{(H + L) / 2 + V}$ where, H, V, and L are a normalized form of TC1, TC2, and TC3 bands	(20)	Deng and Wu 2012
15	$RNDSI = NNDSI / NTC1$, where, NNDSI is the normalized NDSI, and NTC1 is the normalized TC1	(21)	Deng <i>et al.</i> 2015
16	$CBI = \frac{(PC1 + NDWI) / 2 - SAVI}{(PC1 + NDWI) / 2 + SAVI}$ where, PC1 is the first band of PCA	(22)	Sun <i>et al.</i> 2016
17	$BLFEI = \frac{((Green + Red + SWIR2) / 3) - SWIR1}{((Green + Red + SWIR2) / 3) + SWIR1}$	(23)	Bouhennache <i>et al.</i> 2018

SL = ; EQN = equation number.

Chen *et al.* (2019) developed enhanced normalized difference impervious surface index (ENDISI) where preprocessing such as removing waterbodies is not required. Besides, it is efficient in separating bare soil from ISA. It used a generalized Gaussian model, and an automated threshold selection model for rapid IS extraction. ENDISI has one of the highest classification accuracies and can minimize background information, such as, bare soil, bare rock, and arid land significantly.

The urban area is inversely related to the vegetated area. Therefore, removing vegetated areas may enhance urban indexing accuracy. Following the principle, Zha *et al.* (2003) proposed a binary urban index (BU_b) where both NDBI and NDVI were transformed into a binary image based on whether they have positive value or not. Following that, He *et al.* (2010) modified it to another binary urban (BU_c) index where NDVI is subtracted from NDBI in its raw form. Later on, from the subtraction result, all positive value was transformed into one and negative values into zero. This BU_c is calculated from continuous value. Therefore, subscript c is used. BU_c is also named as an improved normalized difference built-up index (INDBI). INDBI performs 20% better than NDBI.

Similarly, another three indices-based index has been formulated and named as the index-based built-up index (IBI) (Xu 2008). Unlike NDBI, IBI tried to distinguish bare land from ISA. IBI used the green, red, NIR, and SWIR1 band region of Landsat TM/enhanced thematic mapper plus (ETM+). It used the combination of NDBI (Zha *et al.* 2003), soil adjusted vegetation index (SAVI) (Huete 1988), and the modified normalized difference water index (MNDWI) (Xu 2007) indices and output value ranging from -1 to +1. It slightly enhanced the ISA while suppressing other LULC classes (Langner *et al.* 2018). In the IBI-based LULC classification process, enhanced ISA has positive values and all other classes have a negative value. A similar zero threshold index was developed by Stathakis *et al.* (2012). However, the vegetation index built-up index (VIBI) has similarities with IBI and replicate the naming style of NDVI of Crippen (1990). This index used NDVI and NDBI as an element. It has a threshold of zero or very close to zero. It also made some improvement in separating ISA from bare soil. Authors claimed that VIBI has higher accuracy than other unsupervised classification though it suffers from the false-negative problem.

The spectral similarity of ISA and soil is a crucial problem that Deng and Wu (2012) first successfully addressed. The BCI is essential because of its ability to separate bare soil class from ISA. The authors proposed BCI based on the vegetation-impervious surface-soil (V-I-S) model (Ridd 2007) and using tasselled cap (TC) transformation (Kauth and Thomas 1976). BCI used the first three TC transformation to calculate the index. All the TC bands used in the equation were normalized beforehand. The benefit of using TC bands is that already various RS sensors have their TC coefficient developed. Therefore, BCI can be calculated from all these sensors besides Landsat. The removal of water bodies at the preprocessing stage allows the index to become more sensitive to bare soil and ISA difference. It can minimize bare soil because of its dry state.

Ratio normalized difference soil index (RNDSI) (Deng *et al.* 2015) suppressed every other feature class but bare soil. It used the first component of TC transformation (TC1) and normalized difference soil index (NDSI) (Rogers and Kearney 2010) to formulate RNDSI. RNDSI performed better than BCI and had high accuracy in separating ISA from bare soil. Similar indexing techniques were used by Sun *et al.* (2016) using PCA instead of TC to propose a combinational built-up index (CBI). It did not require the removal of water bodies. Instead of TC2 and TC3, it used vegetation index SAVI and NDWI. It is an improvement over BCI regarding dealing with water bodies. In BCI, waterbodies were required to remove prior calculation where CBI did not require the preprocessing steps.

On the contrary, Bouhennache *et al.* (2018) argued that the separability of built-up from bare soil could be achieved using SWIR1 and SWIR2 band spectral regions. They developed a built-up land features extraction index (BLFEI) using green, red, SWIR1, and SWIR2 operational land imager (OLI) bands. In BLFEI, water had the highest value and vegetation had the lowest. The values of impervious surface areas were lower than water and higher than bare soil areas. This index also had a higher spectral discrimination index than other similar urban indices.

Indices with PAN Band

All the urban indices with PAN bands are sensitive to the soil. Especially, ISA related indices are needed more to purify from pervious bare soil area. PAN band has a wide spectral range and usually is captured in higher spatial resolution.

Piyooosh and Ghosh (2017) modified the NDSI using a PAN band and named it "modified NDSI" (MNDSI). Where PAN is for panchromatic, MNDSI works better with bare bright soil. MNDSI also increases the spectral resolution slightly and provides better results than other soil indices. Piyooosh and Ghosh (2017) used BCI and MNDSI further and proposed a ratio of the urban index (RUI) (see Table 3). RUI increased the separability of bare soil and ISA.

Table 3. List of urban indices with panchromatic (PAN) bands.

SL	Equation	EQN	Reference
1	$MNDSI = (SWIR2 - PAN)/(SWIR2 + PAN)$	(24)	Piyooosh and Ghosh 2017
2	$RUI = BCI / MNDSI$	(25)	
3	$NRUI = (RUI - MNDSI)/(RUI + MNDSI)$	(26)	

SL = ; EQN = equation number.

On the other hand, the normalized ratio of the urban index (NRUI) enhanced the separability even further. NRUI can distinguish soil and urban area better than RUI and BCI. Here, the author's method's novelty is to use the PAN band to calculate MNDSI, which increased the separability of ISA and bare soil area. Another advantage of the PAN band is pan-sharpening, which also increases LULC classification accuracy.

Indices with Thermal Bands

Urban artificial landscape often stores and emits more heat than surrounding nonurban areas, called the UHI phenomenon. Therefore, there is a spatial difference in temperature between urban and nonurban areas. Therefore, thermal RS data were used to developed newer spectral indices and increase classification accuracy. Normalized difference impervious surface index (NDSI), developed by Xu (2010), was the first automated index to deal with ISA which did not require removing water bodies and soil areas as preprocessing. It is also applicable to moderate resolution RS without the help of higher resolution images for manual assistance, where VIS_1 can be one of the visible bands. However, this index has some problems with water noise and is often mixed with ISA. To solve this problem, the authors suggested using a water index instead of visible bands.

Addressing that, various combinations of bands had been used in urban indexing. For example, As-syakur *et al.* (2012) included thermal, NIR, and SWIR1 bands for the new urban index development. Enhanced built-up and bareness index increase the separability among built-up and bare land and increase classification accuracy claimed in the study.

Furthermore, bare land areas also vary and not all of them are detectable using thermal band induced index, because in

urban areas, small-sized bare lands do not show any significant thermal variation (see Table 4).

A normalized difference water index (NDWI) or MNDWI can also be used as a water index in this equation. NDISI significantly increases the ISA signature, with a similar intention to enhance the ISA feature class and minimize the previous surface. Sun *et al.* (2017) proposed a modified NDISI (MNDISI_{Sun}) differently. Instead of the thermal infrared (TIR) band, the authors used the land surface temperature (LST) value. In this modification LST, or T_s, needs to be resampled to 30 m from TIR bands.

MNDISI_{Sun} can be used for Landsat mission TM, ETM+, and OLI thermal infrared sensors (TIRS), but images from summer-time will provide better results. With overall accuracy, 87% and an overall Kappa coefficient of 74%, MNDISI_{Sun} is suitable for time series analysis with multiple Landsat missions. Another thermal data-based urban index, NDBI of Bhatti and Tripathi (2014), which is developed from the Landsat OLI data set and therefore renamed as NDBI_{OLI}, used PCA for formulation. In that study, the threshold value was selected through a double-window flexible pace search, increasing accuracy rather than traditional NDBI. NDBI_{OLI} later helped develop another urban index named built-up area extraction method (BAEM) by Bhatti and Tripathi (2014).

Another example of multiple index-based urban indexes is BAEM. It is developed by Bhatti and Tripathi (2014) in an attempt to increase urban mapping accuracy. It is important to notice NDBI_{OLI} (Bhatti and Tripathi 2014) is modified and calculated differently than what Zha *et al.* (2003) proposed. BAEM significantly improves the classification accuracy by reducing omission and commission errors.

The first NDBI-like ISA index was a normalized difference impervious index (NDII) developed using Landsat TM visual and thermal bands (Wang *et al.* 2015). In NDII, Vis stands for visible bands, and TIR stands for thermal bands. A combination of red band with a thermal band has found higher accuracy when tested with high-resolution images. NDII is a simple index and can be used for rapid ISA extraction using any multispectral data sets with thermal and visible bands. Urban ISA features have high correlations with thermal data and, conversely, vegetation has inverse correlations with urban ISA. In the next section, we discuss those urban indices those are using vegetation indices to formulate.

A thermal data set can be used to enhance classification accuracy. For example, Rasul *et al.* (2018) proposed a dry built-up index (DBI) using blue and thermal bands from Landsat OLI. DBI assumes that built-up areas have less vegetation and, therefore, low in NDVI values. Thus, subtracting NDVI can further enhance the built-up features. The study suggested using a threshold

value of 0.72. Applicable in a dry climate, DBI has an overall classification accuracy of 93%. An urban area with high vegetation is not suitable to use DBI. Thermal data has some limitations to be considered before use. The spectral difference of thermal bands is mild and often shows phenological and daytime variation between urban and nonurban areas.

Indices with NTL RS

NTL RS is a night light sensor representing the human activity at night from space. The urban landscape is different in using light in contrast to nonurban areas. Therefore, using NTL spectral RS data with daytime, multispectral sensors have newer insights into urban studies (see Table 5).

In 2008, a multi-sourced human settlement index (HIS) fused Terra MODIS NDVI with an NTL data set, Defense Meteorological Satellite Program—Operational Linescan System (DMPS-OLS) (Lu *et al.* 2008). Both data sources have a coarse spatial resolution, but it serves well for large scale settlement mapping. NDVI_m is the maximum NDVI derived from Terra MODIS, and NTL_N has a normalized DMSP-OLS data set into 0 to 1. Landsat ETM+ data set is used only as a reference in this index. With a larger pixel size, human settlement index (HSI) is a rapid and cost-effective indexing method, but it has a saturation problem.

Table 4. List of urban indices with thermal bands.

SL	Equation	EQN	Reference
1	$\text{NDISI} = \frac{\text{TIR} - (\text{VIS}_1 + \text{NIR} + \text{SWIR1}) / 3}{\text{TIR} + (\text{VIS}_1 + \text{NIR} + \text{SWIR1}) / 3}$	(27)	Xu 2010
2	$\text{NDISI} = \frac{\text{TIR} - (\text{WI} + \text{NIR} + \text{SWIR1}) / 3}{\text{TIR} + (\text{WI} + \text{NIR} + \text{SWIR1}) / 3}$	(28)	
3	$\text{EBBI} = \frac{\text{SWIR1} + \text{NIR}}{10\sqrt{\text{SWIR1} + \text{TIR}}}$	(29)	As-syakur <i>et al.</i> 2012
4	$\text{MNDISI}_{\text{Sun}} = \frac{T_s - (\text{MNDWI} + \text{NIR} + \text{SWIR1}) / 3}{T_s + (\text{MNDWI} + \text{NIR} + \text{SWIR1}) / 3}$ <p>where, $T_s = \frac{\text{TIR}}{1 + \left(\frac{\lambda * \text{TIR}}{\rho}\right) \ln \epsilon}$</p> $\rho = 1.438 \times 10^{-2}$ $\epsilon = \begin{cases} 0.979 - 0.035\text{Red} & \text{NDVI} < \text{NDVI}_{\min} \\ 0.986 + 0.004P_v & \text{NDVI}_{\min} < \text{NDVI} < \text{NDVI}_{\max} \\ 0.99 & \text{NDVI} > \text{NDVI}_{\max} \end{cases}$ $P_v = \left(\frac{\text{NDVI} - \text{NDVI}_{\min}}{\text{NDVI}_{\max} - \text{NDVI}_{\min}}\right)^2$	(30)	Sun <i>et al.</i> 2017
5	$\text{NDBI}_{\text{OLI}} = \frac{(\text{PCA of SWIR1, SWIR2} + \text{PCA of TIR1, TIR2}) - \text{NIR}}{(\text{PCA of SWIR1, SWIR2} + \text{PCA of TIR1, TIR2}) - \text{NIR}}$	(31)	Bhatti and Tripathi 2014
6	$\text{BAEM} = \text{NDBI}_{\text{OLI}} - \text{NDVI} - \text{MNDWI}$	(32)	Bhatti and Tripathi 2014
7	$\text{NDII} = (\text{Vis} - \text{TIR}) / (\text{Vis} + \text{TIR})$	(33)	Wang <i>et al.</i> 2015
8	$\text{DBI} = \frac{\text{Blue} - \text{TIR1}}{\text{Blue} + \text{TIR1}} - \text{NDVI}$	(34)	Rasul <i>et al.</i> 2018

SL = ; EQN = equation number.

Zhang *et al.* (2013) proposed the vegetation adjusted NTL urban index (VANUI) to solve the saturation problem. VANUI increases the NTL signal's contrast and better represents urban characteristics than previous NTL derived urban indices. It is useful for advanced urban studies, such as energy usage, carbon emissions, urban structures, etc. A similar approach with MODIS NDVI and the day/night band of visible infrared imaging radiometer suite's (VIIRS-DNB) adopts fractional ISA mapping. Guo *et al.* (2015) proposed a large-scale impervious surface index (LISI) that performs better than VANUI. Whereas $NDVI_{max}$ is the maximum annual MODIS NDVI and NTL_{nor} is the normalized NTL data of VIIRS-DNB. LISI has an overall accuracy of 0.13 and suitable for urban and rural area ISA mapping of a large area. At the same time, Zhang *et al.* (2015) similarly proposed a normalized difference urban index (NDUI). NDUI used Defense Meteorological Program Operational Line-Scan System (DMSP-OLS) and Landsat RSI. In this equation, NTL is the normalized DMSP-OLS image. Here, it is assumed that water has an NDVI value of less than 0 and the goal of the $NDVI \geq 0$ part is dedicated to removing water pixels. With output value between 0 to 1, NDUI can separate mixed urban areas from bare lands and farmlands.

Another multi-sensor urban index used MODIS enhanced vegetation index (EVI), Landsat ETM+, and DMSP-OLS NTL data named normalized urban areas composite index (NUACI) contributed by increasing classification accuracy (Liu *et al.* 2015). It is calculated using three independent data sets: MODIS derived EVI, Landsat derived NDWI, and normalized DMSP-OLS image. This index also has a positive output value from 0 to 1. It eliminates the blooming effect and reduces saturation problems of coarse NTL data sets. Instead of coarse MODIS-based EVI (Huete *et al.* 1997), medium resolution Landsat-based SAVI (Qi *et al.* 1994) has been used in the formation of nighttime light adjusted impervious surface index (NAISI). Developed by Chen, Jia, and Pickering (2019) and followed by the baseline subtraction approach, NAISI used NTL, the first component of the principal component analysis (PC1), the third component of tasseled cap transformation (TC3), and SAVI. Here all the primary RS information is normalized before use. With the finer spatial resolution of NTL, this index can improve ISA extraction accuracy significantly.

In summary, the HSI used the MODIS NDVI and DMSP-OLS NTL data set (Lu *et al.* 2008). Later, using Landsat and NTL data, MNDISI (MNDISILiu) modification was developed, which used thermal, NTL, and Landsat data sets (Liu *et al.* 2013). Afterward, MODIS EVI, Landsat ETM+, and DMSP-OLS were used to develop normalized urban areas composite index (NUACI) (Liu *et al.* 2015) with higher accuracy. On the other hand, VANUI correlates urban characteristics with vegetation absence and NTL presence (Zhang *et al.* 2013). A similar approach, normalized urban indexing, was later developed with NDUI (Zhang *et al.* 2015). All these indices discussed above use both NTL and daytime RSI. This combination can study many other global phenomena, especially with cloud computing platforms, such as GEE (Patel *et al.* 2015, Zhang *et al.* 2015). In the next section, we discuss urban indices with optical, NTL, and thermal data sets.

Complex Indices with Optical, NTL and Thermal Indices

Recently, few complex indices combined day and night RS data by using optical, thermal, and NTL data sets (see Table 6). Thermal RS data has been widely used in the UHI study. It has applications within urban spectral indexing too. In the previous section, optical and NTL data fusion has been shown at the pixel level. The added thermal data to formulate urban indices with higher accuracy were listed and discussed here.

Liu *et al.* (2013) modified NDISI (Xu 2010) and developed MNDISI, which address issues of spectral difference within IS and spectral similarity with other land cover classes, especially with bare soil. Here, T_{LST} is the daytime LST, L_{LIT} is the luminosity derived from nighttime light imagery, SAVI is the vegetation index, and SWIR1 is the band 5 in Landsat TM/ETM+ (Liu *et al.* 2013). MNDISILiu is a multi-sourced index that used the three Rs data sets; ISS nighttime photograph, LST, and multi-spectral bands. Instead of ISS nighttime photograph, it can be calculated using the DMSP-OLS or VIIRS data set too. MNDISILiu is useful for various scaled urban dynamics study with robust ISA extraction capacity. Another index named MNDISISun developed by Sun *et al.* (2017) is discussed in the previous section.

Similarly, Hao *et al.* (2015) also developed an index by combining optical, NTL, and thermal data. They used the NTL data set from DMSP-OLS, MODIS-based NDVI, and MODIS-based LST data while proposing VTLI. Here, $NDVI_{max}$ represents maximum annual NDVI, Tem_{max} represents the maximum annual night temperature, and NTL_{nor} represents normalized DMSP-OLS light data. All the data sets are normalized within 0 to 1.

Table 5. List of urban indices with nighttime lights (NTL) remote sensing (RS).

SL	Equation	EQN	Reference
1	$HSI = \frac{(1 - NDVI_m) - NTL_N}{(1 - NTL_N) + NDVI_m + (NDVI_m * NTL_N)}$	(35)	Lu <i>et al.</i> 2008
2	$VANUI = (1 - NDVI_{nor}) * NTL_{nor}$	(36)	Zhang <i>et al.</i> 2013
3	$LISI = (1 - NDVI_{max}) * \sqrt{NTL_{nor}}$	(37)	Guo <i>et al.</i> 2015
4	$NDUI = \frac{NTL - NDVI}{NTL + NDVI}, (NDVI \geq 0)$	(38)	Zhang <i>et al.</i> 2015
5	$NUACI = \begin{cases} 0.d > r, d = \sqrt{(NDWI - a)^2 + (EVI_{max} - b)^2} \\ \left(1 - \frac{d}{r}\right) * NTL_{Norm}, d \leq r \end{cases}$	(39)	Liu <i>et al.</i> 2015
where, d , r , and NTL_{norm} stands for the mean of NDWI, mean of EVI_{max} , and normalized form of DMSP-OLS image			
6	$NAISI = \left(\frac{NTL - PC1_{nor} + TC3_{nor}}{2} \right) - SAVI_{nor}$	(40)	Chen <i>et al.</i> 2019

SL = ; EQN = equation number.

Table 6. List of complex urban indices.

SL	Equation	EQN	Reference
1	$MNDISILiu = \frac{T_{LST} + L_{LIT} - (SAVI + SWIR1)}{T_{LST} + L_{LIT} + (SAVI + SWIR1)}$	(41)	Liu <i>et al.</i> 2013
2	$VTLI = (1 - NDVI_{max}) * Tem_{max} * NTL_{nor}$	(42)	Hao <i>et al.</i> 2015
3	$TVANUI = \frac{\arctan(LST / NDVI)}{\pi / 2} * NTL$	(43)	Zhang <i>et al.</i> 2018

SL = ; EQN = equation number.

VTLI successfully enhanced DMSP-OLS data set by minimizing blooming and saturation effects. The study found that urban centers concentrated on 30% to 100% of high VTLI values. It is worth mentioning that VTLI uses a monthly composition data set from MODIS instead of daily data. It has both better accuracy and robustness than VANUI.

Furthermore, though it used a coarse MODIS data set, it achieved accuracy close to Landsat derived classification. Zhang and Li (2018) proposed temperature vegetation adjusted NTL urban index (TVANUI) using VI, NTL, and LST, which reduced the blooming and saturation effects of NTL. It was applied in both China and the U.S. and performed better than all earlier urban spectral indices. Inside TVANUI, all used indices are normalized. Negative values of NDVI consider 0 because, in negative NDVI, there is no ISA.

Discussion

In remote sensing, spectral indices are used for mapping, feature extraction, LULC, and similar studies. Multi-temporal scene-based studies can also deal with additional change detection studies (Chen *et al.* 2003; Gholinejad and Fatemi 2019). Furthermore, trend analysis and time series analysis is also popular with spectral indexing. All of the above mention studies have been applied in urban studies. Urban mapping (Thomas *et al.* 2003), urban change detection (Gupta and Munshi 2007), and urban time series analysis (Fu and Weng 2016) are more frequent.

Indexing Urban to ISA

In the beginning, urban researchers tried to index urbanism as a whole. Later urban characteristics, such as built-up areas, were emphasized in indices; for example, NDBI, NBAI, NBI, BUI are developed around the built-up nature of urban. Built-up areas are followed by imperviousness to being used in urban indexing. NDISI, NDII, ENDISI, MNDISI, LISI are all urban indices which index imperviousness in various ways.

Unlike the built-up area, ISA is a better indicator for the urban area. ISA used in urban characteristics, environmental issues, UHI, economic development, urban hydrology, urban flooding, etc. as an indicator. The problem with ISA is, by definition, it is the opposite of pervious bare soil. However, separating bare soil and ISA through spectral signature is very difficult. Therefore, separating these two classes are very crucial for recent urban indexing attempts.

Resolution Dependent Application

This section will discuss spatial, spectral, and temporal resolutions with their relation to indexing. We are omitting discussion of radiometric resolution because 8 bit resolution is enough for urban study and recent 14 bit sensors have no significant impact on urban studies.

Spatial Resolution

Urban areas tend to acquire smaller land use than other primary land covers. Midrange spatial resolutions, 10–30 meters, are enough to study urban mapping. A higher spatial resolution will provide better classification accuracy in solving the urban heterogeneity problem. On the contrary, airborne RS sensors have very high ground resolution and are applicable for detailed and more accurate LULC classification. The airborne platform can provide submeter spatial resolution along with detailing urban mapping capability.

Spectral Resolution

Multispectral RS has visible, NIR, SWIR, and TIR bands. All these bands are used in urban indexing. Among them, SWIR is most used and followed by NIR for urban indexing.

Multispectral RS has spectral limitations and many of them can be solved by adopting hyperspectral RSI. NTL has a coarser

spectral range, ranging from 400–1000 nm in DMSP-OLS and 500–900 nm in *Suomi-NPP*. Hyperspectral RS is unique for its equal spaced spectral ranges. Spectral ranges and the number of bands vary per sensor. The study of spectral signature is a by-product of hyperspectral RS and help detail LULC classification.

Temporal Resolution

Single cloud-free RSI is enough for urban mapping, but cloud coverage is a common problem in optical RS and often requires extracting cloud-free pixels from multiple RSI. In this case, higher temporal resolution plays a good role. Change detection studies required fair temporal resolution based on the duration of the study. Time series analysis, on the contrary, needs flexible temporal data availability to conduct. Recently, monthly image-based time-series studies are getting popular, which requires very high temporal resolution. Furthermore, RSI composites are getting trendy in mapping to time series analysis.

Sensor Dependent Application

Sensor types also have an impact on urban indexing. Optical, thermal, and NTL sensors all have pixel format in data storage, therefore useable together. Furthermore, most of the urban spectral indices are developed from optical multispectral RS have NIR and SWIR bands, which are the primary bands used for urban spectral indexing. Urban ISA has high reflectance in the SWIR spectral region and medium reflectance in the NIR spectral region. Earlier urban indices were developed using these two spectral regions.

Urban ISA is hotter than the surrounding environment due to UHI phenomena. Many urban studies also used thermal characteristics to develop better urban spectral indices. Based on that, NDBI_{OLI} (Bhatti and Tripathi 2014), NDII (Wang *et al.* 2015), NDISI (Xu 2010), MNDISI_{Sum} (Sun *et al.* 2017), DBI (Rasul *et al.* 2018), and TVANUI (Zhang and Li 2018) are some of the examples of the thermal band used in urban spectral indexing. Thermal bands are usually coarser than optical bands and it is a limitation of NTL sensors. Furthermore, seasonality and time of the day affect the thermal bands' separability.

NTL is very popular among RS researchers and unbiasedly presents human activity from space through light. Every type of NTL data does not represent urban lights; only temporally stable NTL's do. Therefore, normalized stable NTL data is often used for urban indexing purposes. Regional mapping is preferable with NTL because of its coarse spatial resolution where either it overlooks or overestimates smaller settlements in single city studies with NTL. Last of all, data limitations, saturation, and blooming effects are some of the limitations which are minimized in newer NTL's.

Spectral Confusion Between ISA and Bare Soil

Urban ISA and bare soil are the two most confusing LULC classes in the optical RS domain. Spectral similarity, chemical composition, and even visible color are so similar that the earliest urban indices consider them as one class. To this end, the problem of spectral similarity can be solved using hyperspectral RS, tasseled cap transformation, panchromatic band, and so on. Deng and Wu (2012) used tasseled cap transformations to develop BCI, which has good separability of ISA and bare soil with mild contrast. Piyoosh and Ghosh (2017) developed MNDISI using PAN bands.

Nevertheless, not all sensors have PAN bands. Therefore, Bouhennache *et al.* (2018) developed BLFEI without using PAN bands. All these indices are capable of distinguishing ISA and bare soil. Another approach to estimating ISA is to subtract bare soil from it. For instance, Rasul *et al.* (2018) developed the dry bare-soil index and the urban index DBI.

Moreover, thermal bands and NTL information is also useful to separate urban ISA from bare soil. Finally, thermal data's potential limitation is the difference between these two data,

which is mild and varies seasonally. In the case of NTL, it has a very coarse spatial resolution.

Threshold

Image segmentation with indexing requires thresholds. Usually, researchers use their experience and trial and error techniques to define a more accurate threshold for a particular study, which works fine with their selected study time, place, and data sets. However, the threshold often varies spatiotemporally. Following that, automatic thresholding can speed up the segmentation process. With urban ISA extraction, the accurate threshold is crucial (Firozjaei *et al.* 2019), such as the OTSU method, but it works better on well distinguishable two classes. Hence, it is not recommended with multiclass classification.

Limitations

Our work has several limitations. Firstly, we list urban indices and discuss their merits and demerits, but did not perform any comparative analysis. However, we cite some previous comparative work. Secondly, we enlisted urban spectral indices but did not suggest any ranking for them. However, we discussed the performance between the two indices in some instances. Thirdly, we have not discussed the development process of those indices. Besides, choosing one or more urban indices depends on the study's circumstances.

Fourthly, we did not include any index with hyperspectral, LiDAR, and synthetic aperture radar (SAR) RS data. Hyperspectral RS data has enormous potentials in urban studies with indices, especially in classifying ISA from bare soil class and addressing urban heterogeneity (Zhu *et al.* 2019). Besides hyperspectral, SAR and LiDAR data sets are also helpful in the vertical study of urban spaces. Detecting urban vertical expansion is difficult to measure with optical RS but LiDAR and SAR can be useful for these purposes and can be fused at the decision level to get better classification results.

Finally, we mention only the OTSU method in the threshold subsection, but many other thresholding techniques are not discussed here. Moreover, the selection of thresholding techniques might also vary per index. Further studies may work on thresholding and spectral indices in the future.

Knowledge Gaps

In the last two decades, spectral urban studies experienced many developments, but many questions remain unanswered. We are yet to know the common spectral urban characteristics that function globally. Although NTL data has some potential in this case further study is required. We do not know yet how to define an urban area from RSI, irrespective of geographical difference. Besides, there is an absence of common global characteristics of the urban area since urban areas are highly heterogeneous. Not only spatially but also temporally, phenology affects LULC classification (Wang and Li 2019). For the time being, the most common problem is the spectral similarity of bare soil and ISA. Above all, these are the few questions that need to be answered to advance the future urban RS domain.

The term urban is vague and differs administratively in parallel with infrastructural importance, population size, economic value, and political status. All these factors influence defining the term urban. However, in RS studies, there is no perfect spectral index to define urban areas. Thereupon, it can function only as an indicator.

Future Direction

The fusion of multiple RS source types is trending now. Sooner or later, more multi-source spectral indices will be developed. Spectrally, hyperspectral RS data have substantial potential solving LULC classification problems. Besides, NTL is also a very popular nighttime RS that can easily depict night scenes

from space, even though coarse spatial resolution is limiting its application in urban studies. Newer and improved NTL sensors also have high potentials in advanced urban indexing.

Active RS sensors, such as SAR and LiDAR have advantages in urban studies. These sensors can function both day and night, penetrate clouds, and fog and mist are measured by vertical changes. Though these sensors are different from spectral sensors, innovative fusing techniques can still be used in urban studies. Already, fusing Landsat and SAR data sets were used to estimate ISA and separate ISA from bare soil (Yang *et al.* 2009). Besides, LiDAR has the potential for measuring vertical urban changes.

Zhu *et al.* (2019) reviewed four strategic directions for urban RS studies. These directions are based on higher temporal resolution, hyperspectral remote imagery (HRI), fusing multiple RS data sets, and combining RS data with structural and nonstructural data. Among these four directions, HRI and multiple RS source fusion are directly linked with spectral indexing.

The first urban index was related to population density. Besides population density, GIS data such as population, temperature, rainfall, gross domestic product, traffic, transport details, energy usage, etc., also have potentials in newer urban indexing.

The use of cloud platforms like GEE and free RS data sources will increase indices' use. Apart from that, GEE has global mapping and time-series visualization features. It also has data available from the mid-'90s or even before. Henceforth, future developments may adopt spectral index-based LULC measurements along with it.

In addition, along with the study of urban physical characteristics, soon many abstract issues will be studied assisted with RS spectral indices. Abstract urban concepts, such as seasonality, sustainability, biodiversity, livability, green city, walkability, happiness, richness, urbanism, and so on can be studied using RS spectral indices.

Conclusions

Here, we summarize all the important spectral urban indices with their equations, advantages, and disadvantages and classify them based on their band requirements.

We found that instead of inefficiency, the earlier developed urban spectral indices were simple, single-sourced, and robust to use. Conversely, recent indices are complex, multi-sourced, sophisticated, use rare spectral bands, and are more accurate. Actually, urban indexing began with mapping urban area as a whole and later became more specific in mapping urban characteristics. However, newer RS data sources are becoming available every year with improved capacity and features. The demand for better measurement is now forcing RS researchers to search for improved indices. Cloud computing platforms like GEE and enhanced computing capacity allowed researchers to build complex indices. In addition, overcoming spatiotemporal barriers requires more robust indices. To conclude, the future of urban indexing will determine how efficiently we can answer those questions.

Acknowledgments

The authors are sincerely grateful to the editors and anonymous reviewers for their valuable suggestions and comments that significantly improved this paper. This work is supported by the National Key Research and Development Program of China (2018YFB0505401), the Research Project from the Ministry of Natural Resources of China under Grant 4201-240100123, the National Natural Science Foundation of China under Grants 41771452, 41771454, 41890820, and 41901340,

the Natural Science Fund of Hubei Province in China under Grant 2018CFA007, the Natural Science Foundation of Inner Mongolia Autonomous Region (2019MS04017), and the Scientific research project of colleges and universities in Inner Mongolia Autonomous Region (NJZY20277).

References

- As-syakur, A. R., I.W.S. Adnyana, I. W. Arthana and I. W. Nuarsa. 2012. Enhanced built-up and bareness index (EBBI) for mapping built-up and bare land in an urban area. *Remote Sensing* 4(10):2957–2970.
- Bai, Y., G. He, G. Wang and G. Yang. 2020. WE-NDBI—A new index for mapping urban built-up areas from GF-1 WFV images. *Remote Sensing Letters* 11(5):407–415.
- Baret, F., G. Guyot and D. Major. 1989. TSAVI: A vegetation index which minimizes soil brightness effects on LAI and APAR estimation. Pages 1355–1358 in *Proceedings of the 12th IEEE Canadian Symposium on Remote Sensing Geoscience and Remote Sensing Symposium*, held in Vancouver, Canada.
- Bhatti, S. S. and N. K. Tripathi. 2014. Built-up area extraction using Landsat 8 OLI imagery. *GIScience Remote Sensing* 51(4):445–467.
- Bouhennache, R., T. Bouden, A. Taleb-Ahmed and A. Cheddad. 2018. A new spectral index for the extraction of built-up land features from Landsat 8 satellite imagery. *Geocarto International* 34(14):1531–1551.
- Bouzekri, S., A. A. Lasbet and A. Lachehab. 2015. A new spectral index for extraction of built-up area using Landsat-8 data. *Journal of the Indian Society of Remote Sensing* 43(4):867–873.
- Capolupo, A., C. Monterisi and E. Tarantino. 2020. Landsat images classification algorithm (LICA) to automatically extract land cover information in Google earth engine environment. *Remote Sensing* 12(7):28.
- Chen, J., P. Gong, C. He, R. Pu and P. Shi. 2003. Land-use/land-cover change detection using improved change-vector analysis. *Photogrammetric Engineering & Remote Sensing* 69(4):369–379.
- Chen, J., K. Yang, S. Chen, C. Yang, S. Zhang and L. He. 2019. Enhanced normalized difference index for impervious surface area estimation at the plateau basin scale. *Journal of Applied Remote Sensing* 13(01):19.
- Chen, X., X. Jia and M. Pickering. 2019. A nighttime lights adjusted impervious surface index (NAISI) with integration of Landsat imagery and nighttime lights data from international space station. *International Journal of Applied Earth Observation and Geoinformation*:83.
- Chikr El-Mezouar, M. 2011. Vegetation extraction from IKONOS imagery using high spatial resolution index. *Journal of Applied Remote Sensing* 5(1):14.
- Colwell, J. E. 1974. Vegetation canopy reflectance. *Remote Sensing of Environment* 3(3):175–183.
- Crippen, R. E. 1990. Calculating the vegetation index faster. *Remote Sensing of Environment* 34 (1):71–73.
- Datta, R., D. Joshi, J. Li and J. Wang. 2008. Image retrieval: Ideas, influences, and trends of the new age. *ACM Computing Surveys* 40(2):1–60.
- Dekker, A. G., T. J. Malthus, M. M. Wijnen and E. Seyhan. 1992. The effect of spectral bandwidth and positioning on the spectral signature analysis of inland waters. *Remote Sensing of Environment* 41(2–3):211–225.
- Deng, C. and C. Wu. 2012. BCI: A biophysical composition index for remote sensing of urban environments. *Remote Sensing of Environment* 127:247–259.
- Deng, Y., C. Wu, M. Li and R. Chen. 2015. RNDISI: A ratio normalized difference soil index for remote sensing of urban/suburban environments. *International Journal of Applied Earth Observation and Geoinformation* 39:40–48.
- Digirolamo, L. and R. Davies. 1994. A band-differenced angular signature technique for cirrus cloud detection. *IEEE Transactions on Geoscience and Remote Sensing* 32(4):890–896.
- Duan, Y., X. Shao, Y. Shi, H. Miyazaki, K. Iwao and R. Shibasaki. 2015. Unsupervised global urban area mapping via automatic labeling from ASTER and PALSAR satellite images. *Remote Sensing* 7(2):2171–2192.
- Estoque, R. C. and Y. Murayama. 2015. Classification and change detection of built-up lands from Landsat-7 ETM+ and Landsat-8 OLI/TIRS imageries: A comparative assessment of various spectral indices. *Ecological Indicators* 56:205–217.
- Firozjaei, M., A. Sedighi, M. Kiavarz, S. Qureshi, D. Haase and S. Alavipanah. 2019. Automated built-up extraction index: A new technique for mapping surface built-up areas using LANDSAT 8 OLI imagery. *Remote Sensing* 11(17):20.
- Fu, P. and Q. H. Weng. 2016. A time series analysis of urbanization induced land use and land cover change and its impact on land surface temperature with Landsat imagery. *Remote Sensing of Environment* 175:205–214.
- Gholinejad, S. and S. B. Fatemi. 2019. Optimum indices for vegetation cover change detection in the Zayandeh-rud river basin: A fusion approach. *International Journal of Image and Data Fusion* 10(3):199–216.
- Gomez-Chova, L., J. Amoros-Lopez, G. Mateo-Garcia, J. Munoz-Mari and G. Camps-Valls. 2017. Cloud masking and removal in remote sensing image time series. *Journal of Applied Remote Sensing*:11.
- Gorelick, N., M. Hancher, M. Dixon, S. Ilyushchenko, D. Thau and R. Moore. 2017. Google Earth engine: Planetary-scale geospatial analysis for everyone. *Remote Sensing of Environment* 202:18–27.
- Guo, W., D. Lu, Y. Wu and J. Zhang. 2015. Mapping impervious surface distribution with integration of SNNP VIIRS-DNB and MODIS NDVI data. *Remote Sensing* 7(9):12459–12477.
- Gupta, D. M. and M. K. Munshi. 2007. Urban change detection and land-use mapping of Delhi. *International Journal of Remote Sensing* 6(3-4):529–534.
- Hao, R., D. Yu, Y. Sun, Q. Cao, Y. Liu and Y. Liu. 2015. Integrating multiple source data to enhance variation and weaken the blooming effect of DMSP-OLS light. *Remote Sensing* 7(2):1422–1440.
- He, C., P. Shi, D. Xie and Y. Zhao. 2010. Improving the normalized difference built-up index to map urban built-up areas using a semiautomatic segmentation approach. *Remote Sensing Letters* 1(4):213–221.
- Hester, D. B., S.A.C. Nelson, H. I. Cakir, S. Khorram and H. Cheshire. 2010. High-resolution land cover change detection based on fuzzy uncertainty analysis and change reasoning. *International Journal of Remote Sensing* 31(2):455–475.
- Howarth, P. J. and E. Boasson. 1983. Landsat digital enhancements for change detection in urban environments. *Remote Sensing of Environment* 13(2):149–160.
- Huete, A., H. Liu, K. Batchily and W. Van Leeuwen. 1997. A comparison of vegetation indices over a global set of TM images for EOS-MODIS. *Remote Sensing of Environment* 59(3):440–451.
- Huete, A. R. 1988. A soil-adjusted vegetation index (SAVI). *Remote Sensing of Environment* 25(3):295–309.
- Jawak, S. D. and A. J. Luis. 2013. Improved land cover mapping using high resolution multiangle 8-band WorldView-2 satellite remote sensing data. *Journal of Applied Remote Sensing* 7(1):21.
- Jieli, C., L. Manchun, L. Yongxue, S. Chenglei and H. Wei. 2010. Extract residential areas automatically by new built-up index. Pages 1–5 in *Proceedings of the 2010 18th IEEE International Conference on Geoinformatics*, held in Beijing, China.
- Kaimaris, D. and P. Patias. 2016. Identification and area measurement of the built-up area with the built-up index (BUI). *International Journal of Advanced Remote Sensing and GIS* 5(1):1844–1858.
- Kauth, R. J. and G. S. Thomas. 1976. The tasseled cap—A graphic description of the spectral-temporal development of agricultural crops as seen by LANDSAT. In *IEEE Symposium on Machine Processing of Remotely Sensed Data*, West Lafayette, Indiana: Purdue University.
- Kawamura, M., S. Jayamanna and Y. Tsujiko. 1997. Quantitative evaluation of urbanization in developing countries using satellite data. *Doboku Gakkai Ronbunshu* 1997(580):45–54.

- Khan, A., S. Chatterjee, H. Akbari, S. Bhatti, A. Dinda, C. Mitra, H. Hong and Q.-V. Doan. 2017. Step-wise land-class elimination approach for extracting mixed-type built-up areas of Kolkata megacity. *Geocarto International*:1–47.
- Kobayashi, N., H. Tani, X. Wang and R. Sonobe. 2019. Crop classification using spectral indices derived from Sentinel-2A imagery. *Journal of Information and Telecommunication* 4(1):67–90.
- Langner, A., J. Miettinen, M. Kukkonen, C. Vancutsem, D. Simonetti, G. Vieilledent, A. Verhegghen, J. Gallego and H.-J. Stibig. 2018. Towards operational monitoring of forest canopy disturbance in evergreen rain forests: A test case in continental southeast Asia. *Remote Sensing* 10(4).
- Li, C., Shao, Z., Zhang, L., Huang, X. and Zhang, M., 2021. A Comparative Analysis of Index-Based Methods for Impervious Surface Mapping Using Multiseasonal Sentinel-2 Satellite Data, *IEEE Journal of Selected Topics in Applied Earth Observations and Remote Sensing*, 14:3682-3694.
- Li, D., Ma, J., Cheng, T., van Genderen, J.L. and Shao, Z., 2018. Challenges and opportunities for the development of megacities, *International Journal of Digital Earth*.
- Li, W. 2020. Mapping urban impervious surfaces by using spectral mixture analysis and spectral indices. *Journal of Remote Sensing* 12(1):94.
- Liu, C., Z. Shao, M. Chen and H. Luo. 2013. MNDISI: A multi-source composition index for impervious surface area estimation at the individual city scale. *Remote Sensing Letters* 4(8):803–812.
- Liu, J. and P. Li. 2019. Extraction of earthquake-induced collapsed buildings from bi-temporal VHR images using object-level homogeneity index and histogram. *IEEE Journal of Selected Topics in Applied Earth Observations and Remote Sensing* 12(8):2755–2770.
- Liu, X., G. Hu, B. Ai, X. Li and Q. Shi. 2015. A normalized urban areas composite index (NUACI) based on combination of DMSP-OLS and MODIS for mapping impervious surface area. *Remote Sensing* 7(12):17168–17189.
- Liu, X., G. Hu, Y. Chen, X. Li, X. Xu, S. Li, F. Pei and S. Wang. 2018. High-resolution multi-temporal mapping of global urban land using Landsat images based on the Google Earth engine platform. *Remote Sensing of Environment* 209:227–239.
- Lu, D., H. Tian, G. Zhou and H. Ge. 2008. Regional mapping of human settlements in southeastern China with multisensor remotely sensed data. *Remote Sensing of Environment* 112(9):3668–3679.
- Meyer, W. B. and B. L. Turner II, eds. 1994. *Changes in Land Use and Land Cover: A Global Perspective*. Cambridge, United Kingdom: Cambridge University Press.
- Lyimo, N.N., Shao, Z., Ally, A.M., Twumasi, N.Y.D., Altan, O. and Sanga, C.A., 2020. A Fuzzy Logic-Based Approach for Modelling Uncertainty in Open Geospatial Data on Landfill Suitability Analysis, *ISPRS International Journal of Geo-Information*, 9(12):737.
- Moosavi, V., A. Talebi, M. H. Mokhtari and M. R. Hadian. 2016. Estimation of spatially enhanced soil moisture combining remote sensing and artificial intelligence approaches. *International Journal of Remote Sensing* 37(23):5605–5631.
- Nichol, J. and C. M. Lee. 2006. Urban vegetation monitoring in Hong Kong using high resolution multispectral images. *International Journal of Remote Sensing* 26(5):903–918.
- Nouri, H., S. Beecham, S. Anderson and P. Nagler. 2014. High spatial resolution WorldView-2 imagery for mapping NDVI and its relationship to temporal urban landscape evapotranspiration factors. *Remote Sensing* 6(1):580–602.
- Olaode, A., G. Naghdy and C. Todd. 2014. Unsupervised classification of images: A review. *International Journal of Image Processing* 8(5):325–342.
- Pan, X.-Z., S. Uchida, Y. Liang, A. Hirano and B. Sun. 2010. Discriminating different landuse types by using multitemporal NDXI in a rice planting area. *International Journal of Remote Sensing* 31(3):585–596.
- Parent, J. R., J. C. Volin and D. L. Civco. 2015. A fully-automated approach to land cover mapping with airborne LiDAR and high resolution multispectral imagery in a forested suburban landscape. *ISPRS Journal of Photogrammetry and Remote Sensing* 104:18–29.
- Patel, N. N., E. Angiuli, P. Gamba, A. Gaughan, G. Lisini, F. R. Stevens, A. J. Tatem and G. Trianni. 2015. Multitemporal settlement and population mapping from Landsat using Google Earth engine. *International Journal of Applied Earth Observation and Geoinformation* 35:199–208.
- Phalke, A. R. and M. Özdoğan. 2018. Large area cropland extent mapping with Landsat data and a generalized classifier. *Remote Sensing of Environment* 219:180–195.
- Piyooosh, A. K. and S. K. Ghosh. 2017. Development of a modified bare soil and urban index for Landsat 8 satellite data. *Geocarto International* 33(4):423–442.
- Qi, J., A. Chehbouni, A. R. Huete, Y. H. Kerr and S. Sorooshian. 1994. A modified soil adjusted vegetation index. *Remote Sensing of Environment* 48(2):119–126.
- Qin, R. and W. Fang. 2014. A hierarchical building detection method for very high resolution remotely sensed images combined with DSM using graph cut optimization. *Photogrammetric Engineering & Remote Sensing* 80(9):873–883.
- Rasul, A., H. Balzter, G. Ibrahim, H. Hameed, J. Wheeler, B. Adamu, S.a. Ibrahim and P. Najmaddin. 2018. Applying built-up and bare-soil indices from Landsat 8 to cities in dry climates. *Land* 7(3).
- Ridd, M. K. 2007. Exploring a V-I-S (vegetation-impervious surface-soil) model for urban ecosystem analysis through remote sensing: Comparative anatomy for cities. *International Journal of Remote Sensing* 16(12):2165–2185.
- Rogers, A. S. and M. S. Kearney. 2010. Reducing signature variability in unmixed coastal marsh Thematic Mapper scenes using spectral indices. *International Journal of Remote Sensing* 25(12):2317–2335.
- Rondeaux, G., M. Steven and F. Baret. 1996. Optimization of soil-adjusted vegetation indices. *Remote Sensing of Environment* 55(2):95–107.
- Rouse Jr, J. W., R. Haas, J. Schell and D. Deering. 1974. Monitoring vegetation systems in the Great Plains with ERTS. Pages 301–317 in *Proceedings of the Third Earth Resources Technology Satellite-1 Symposium*, Volume I: Technical Presentations. NASA SP-351. Edited by S. C. Freden, E. P. Mercanti, and M. A. Becker. Wash., D.C.: NASA.
- Sellers, P. 1987. Canopy reflectance, photosynthesis, and transpiration, II. The role of biophysics in the linearity of their interdependence. *Remote Sensing of Environment* 21(2):143–183.
- Shao, Z., Wu, W. and Li, D., 2021. Spatio-temporal-spectral observation model for urban remote sensing, *Geo-Spatial Information Science*:1-15.
- Shao, Z.F., Fu, H.Y., Li, D.R., Altan, O. and Cheng, T., 2019. Remote sensing monitoring of multi-scale watersheds impermeability for urban hydrological evaluation, *Remote Sensing of Environment*, 232:11.
- Shelestov, A., M. Lavreniuk, N. Kussul, A. Novikov and S. Skakun. 2017. Exploring Google Earth engine platform for big data processing: classification of multi-temporal satellite imagery for crop mapping. *Frontiers in Earth Science* 5:1–10.
- Stathakis, D., K. Perakis and I. Savin. 2012. Efficient segmentation of urban areas by the VIBI. *International Journal of Remote Sensing* 33(20):6361–6377.
- Sun, G., X. Chen, X. Jia, Y. Yao and Z. Wang. 2016. Combinational build-up index (CBI) for effective impervious surface mapping in urban areas. *IEEE Journal of Selected Topics in Applied Earth Observations and Remote Sensing* 9(5):2081–2092.
- Sun, Z., C. Wang, H. Guo and R. Shang. 2017. A modified normalized difference impervious surface index (MNDISI) for automatic urban mapping from landsat imagery. *Remote Sensing* 9(9):18.
- Surin, V. G. and G. A. Ladner. 1995. Spectral signatures of vegetation in the 8-to-14 mu-m thermal infrared region. *Earth Observation and Remote Sensing* 12(3):341–352.

- Thomas, N., C. Hendrix and R. G. Congalton. 2003. A comparison of urban mapping methods using high-resolution digital imagery. *Photogrammetric Engineering and Remote Sensing* 69(9):963–972.
- Tian, Y., H. Chen, Q. Song and K. Zheng. 2018. A novel index for impervious surface area mapping: development and validation. *Remote Sensing* 10(10):23.
- Vachon, P. W. and J. C. West. 1992. Spectral estimation techniques for multilook SAR images of ocean waves. *IEEE Transactions on Geoscience and Remote Sensing* 30(3):568–577.
- Wang, Y. and M. Li. 2019. Urban impervious surface detection from remote sensing images: A review of the methods and challenges. *IEEE Geoscience and Remote Sensing Magazine* 7(3):64–93.
- Wang, Z., C. Gang, X. Li, Y. Chen and J. Li. 2015. Application of a normalized difference impervious index (NDII) to extract urban impervious surface features based on Landsat TM images. *International Journal of Remote Sensing* 36(4):1055–1069.
- Waqar, M. M., J. F. Mirza, R. Mumtaz and E. Hussain. 2012. Development of new indices for extraction of built-up area & bare soil from Landsat data. *Open Access Scientific Reports* 1(1):4.
- Wu, W., Q. Li, Y. Zhang, X. Du and H. Wang. 2018. Two-step urban water index (TSUWI): A new technique for high-resolution mapping of urban surface water. *Remote Sensing* 10(11):21.
- Xie, Y., Z. Sha and M. Yu. 2008. Remote sensing imagery in vegetation mapping: A review. *Journal of Plant Ecology* 1(1):9–23.
- Xu, H. 2007. Modification of normalised difference water index (NDWI) to enhance open water features in remotely sensed imagery. *International Journal of Remote Sensing* 27(14):3025–3033.
- Xu, H. 2008. A new index for delineating built-up land features in satellite imagery. *International Journal of Remote Sensing* 29(14):4269–4276.
- Xu, H. 2010. Analysis of impervious surface and its impact on urban heat environment using the normalized difference impervious surface index (NDISI). *Photogrammetric Engineering & Remote Sensing* 76(5):557–565.
- Xue, J. and B. Su. 2017. Significant remote sensing vegetation indices: A review of developments and applications. *Journal of Sensors* 2017:1–17.
- Yang, L., L. Jiang, H. Lin and M. Liao. 2009. Quantifying sub-pixel urban impervious surface through fusion of optical and in SAR imagery. *GIScience & Remote Sensing* 46(2):161–171.
- Zha, Y., J. Gao and S. Ni. 2003. Use of normalized difference built-up index in automatically mapping urban areas from TM imagery. *International Journal of Remote Sensing* 24(3):583–594.
- Zhang, Q., C. Schaaf and K. C. Seto. 2013. The vegetation adjusted NTL urban index: A new approach to reduce saturation and increase variation in nighttime luminosity. *Remote Sensing of Environment* 129:32–41.
- Zhang, Q. and K. C. Seto. 2011. Mapping urbanization dynamics at regional and global scales using multi-temporal DMSP/OLS nighttime light data. *Remote Sensing of Environment* 115(9):2320–2329.
- Zhang, Q., B. Li, D. Thau and R. Moore. 2015. Building a better urban picture: Combining day and night remote sensing imagery. *Remote Sensing* 7(9):11887–11913.
- Zhang, S., K. Yang, M. Li, Y. Ma and M. Sun. 2018. Combinational biophysical composition index (CBCI) for effective mapping biophysical composition in urban areas. *IEEE Access* 6:41224–41237.
- Zhang, X. and P. Li. 2018. A temperature and vegetation adjusted NTL urban index for urban area mapping and analysis. *ISPRS Journal of Photogrammetry and Remote Sensing* 135:93–111.
- Zhang, Y. and Shao, Z., 2021. Assessing of Urban Vegetation Biomass in Combination with LiDAR and High-resolution Remote Sensing Images, *International Journal of Remote Sensing*, 42(3):964-985.
- Zhu, Z., Y. Zhou, K. C. Seto, E. C. Stokes, C. Deng, S. T. Pickett and H. Taubenböck. 2019. Understanding an urbanizing planet: Strategic directions for remote sensing. *Remote Sensing of Environment* 228:164–182.

SUSTAINING MEMBERS

Aerial Services, Inc.

Cedar Falls, Iowa
www.AerialServicesInc.com
Member Since: 5/2001

Ayres Associates

Madison, Wisconsin
www.AyresAssociates.com
Member Since: 1/1953

Dewberry

Fairfax, Virginia
www.dewberry.com
Member Since: 1/1985

Environmental Research Incorporated

Linden, Virginia
www.eri.us.com
Member Since: 8/2008

Esri

Redlands, California
www.esri.com
Member Since: 1/1987

F.R. Aleman & Associates, Inc.

Miami, Florida
https://fr-aleman.com
Member Since: 7/2020

GeoCue Group

Madison, Alabama
http://www.geocue.com
Member Since: 10/2003

Geographic Imperatives LLC

Centennial, Colorado
http://geographicimperativesllc.com
Member Since: 9/2021

GeoWing Mapping, Inc.

Richmond, California
www.geowingmapping.com
Member Since: 12/2016

GPI Geospatial Inc.

formerly Aerial Cartographics of America, Inc. (ACA)

Orlando, Florida
www.aca-net.com
Member Since: 10/1994

Green Grid Inc.

San Ramon, California
www.greengridinc.com
Member Since: 1/2020

Halff Associates, Inc.

Richardson, Texas
www.halff.com
Member Since: 8/2021

Keystone Aerial Surveys, Inc.

Philadelphia, Pennsylvania
www.kasurveys.com
Member Since: 1/1985

Kucera International

Willoughby, Ohio
www.kucerainternational.com
Member Since: 1/1992

L3Harris Corporation

Broomfield, Colorado
www.harris.com
Member Since: 6/2008

NV5 Geospatial

Sheboygan Falls, Wisconsin
www.quantumspatial.com
Member Since: 1/1974

Pickett and Associates, Inc.

Bartow, Florida
www.pickettusa.com
Member Since: 4/2007

Robinson Aerial Surveys, Inc.(RAS)

Hackettstown, New Jersey
www.robinsonaerial.com
Member Since: 1/1954

Sanborn Map Company

Colorado Springs, Colorado
www.sanborn.com
Member Since: 10/1984

Surdex Corporation

Chesterfield, Missouri
www.surdex.com
Member Since: 12/2011

Surveying And Mapping, LLC (SAM)

Austin, Texas
www.sam.biz
Member Since: 12/2005

T3 Global Strategies, Inc.

Bridgeville, Pennsylvania
https://t3gs.com/
Member Since: 6/2020

Terra Remote Sensing (USA) Inc.

Bellevue, Washington
www.terrareMOTE.com
Member Since: 11/2016

Towill, Inc.

San Francisco, California
www.towill.com
Member Since: 1/1952

Wingtra

Zurich, Switzerland
https://wingtra.com/
Member Since: 6/2020

Woolpert LLP

Dayton, Ohio
www.woolpert.com
Member Since: 1/1985

SUSTAINING MEMBER BENEFITS

Membership

- ✓ Provides a means for dissemination of new information
- ✓ Encourages an exchange of ideas and communication
- ✓ Offers prime exposure for companies

Benefits of an ASPRS Membership

- Complimentary and discounted Employee Membership*
- E-mail blast to full ASPRS membership*
- Professional Certification Application fee discount for any employee
- Member price for ASPRS publications
- Discount on group registration to ASPRS virtual conferences
- Sustaining Member company listing in ASPRS directory/website
- Hot link to company website from Sustaining Member company listing page on ASPRS website
- Press Release Priority Listing in PE&RS Industry News
- Priority publishing of Highlight Articles in PE&RS plus, 20% discount off cover fee
- Discount on PE&RS advertising
- Exhibit discounts at ASPRS sponsored conferences (exception ASPRS/ILMF)
- Free training webinar registrations per year*
- Discount on additional training webinar registrations for employees
- Discount for each new SMC member brought on board (Discount for first year only)

*quantity depends on membership level

WHO'S WHO IN ASPRS

BOARD OF DIRECTORS

BOARD OFFICERS

President

Jason M. Stoker, Ph.D,
U.S. Geological Survey

President-Elect

Christopher Parrish, Ph.D
Oregon State University

Vice President

Lorraine B. Amenda, PLS, CP
Towill, Inc.

Past President

Jeff Lovin
Woolpert

Treasurer

Stewart Walker, Ph.D.
photogrammetry4u

Secretary

Harold Rempel
ESP Associates, Inc.

BOARD MEMBERS

Sustaining Members Council

Chair: Joe Cantz
<https://www.asprs.org/sustaining-members-council.html>

Committee Chairs Council

Chair: Mike Zoltek

Technical Division Directors Council

Chair: Bandana Kar, Ph.D
Vice Chair: Denise G. Theunissen

Early-Career Professionals Council

Chair: Melissa Martin

Region Officers Council

Chair: Demetrio Zourarakis

Student Advisory Council

Chair: Evan Vega
Vice Chair: Lauren McKinney
<http://www.asprs.org/Students/Student-Advisory-Council.html>

TECHNICAL DIVISION OFFICERS

Geographic Information Systems Division

Director: Denise Theunissen
Assistant Director: Briana Williams
www.asprs.org/Divisions/GIS-Division.html

Lidar Division

Director: Josh Nimetz, CMS
Assistant Director: Ajit Sampath
www.asprs.org/Divisions/Lidar-Division.html

Photogrammetric Applications Division

Director: Kurt Rogers
Assistant Director: Benjamin Wilkinson
www.asprs.org/Divisions/Photogrammetric-Applications-Division.html

Primary Data Acquisition Division

Director: Greg Stensaas
Assistant Director: Srin Dharmapuri
www.asprs.org/Divisions/Primary-Data-Aquisition-Division.html

Professional Practice Division

Director: Bill Swope
Assistant Director: Hope Morgan
www.asprs.org/Divisions/Professional-Practice-Division.html

Remote Sensing Applications Division

Director: Amr Abd-Ehrahman
Assistant Director: Tao Liu
www.asprs.org/Divisions/Remote-Sensing-Applications-Division.html

Unmanned Autonomous Systems (UAS)

Director: Dan Hubert
Assistant Director: Jacob Lopez
<https://www.asprs.org/divisions-committees/uas-division>

REGION PRESIDENTS

Alaska Region

Cascadia Region

Robert Hariston-Porter

Eastern Great Lakes Region

Michael Joos, CP, GISP
<http://egl.asprs.org>

Florida Region

Xan Fredericks
<http://florida.asprs.org>

Heartland Region

Whit Lynn
<http://heartland.asprs.org/>

Intermountain Region

Robert T. Pack
<https://asprsintermountain.weebly.com>

Mid-South Region

David Hughes
<https://www.asprs.org/all-regions/mid-south.html>

Northeast Region

North Atlantic Region

<http://natlantic.asprs.org>

Pacific Southwest Region

John Erickson, PLS, CP
<https://pswasprs.org>

Potomac Region

Dave Lasko
<http://www.asprspotomac.org>

Rocky Mountain Region

<http://www.asprs-rmr.org/>

Western Great Lakes Region

Adam Smith
<http://wgl.asprs.org/>

PE&RS Media Kit 2021

Special Advertising Opportunities

FRONT COVER SPONSORSHIP

A *PE&RS* cover sponsorship is a unique opportunity to capture the undivided attention of your target market through three premium points of contact.

1— *PE&RS* FRONT COVER

(Only twelve available, first-come, first-served)

PE&RS is world-renowned for the outstanding imagery displayed monthly on its front cover—and readers have told us they eagerly anticipate every issue. This is a premium opportunity for any company, government agency, university or non-profit organization to provide a strong image that demonstrates their expertise in the geospatial information industry.

2— FREE ACCOMPANYING “HIGHLIGHT” ARTICLE

A detailed article to enhance your cover image is welcome but not a condition of placing an image. Many readers have asked for more information about the covers and your article is a highly visible way to tell your story in more depth for an audience keenly interested in your products and services. No article is guaranteed publication, as it must pass ASPRS editorial review. For more information, contact Rae Kelley at rkelley@asprs.org.

3— FREE TABLE OF CONTENTS COVER DESCRIPTION

Use this highly visible position to showcase your organization by featuring highlights of the technology used in capturing the front cover imagery. Limit 200-word description.

Terms: Fifty percent nonrefundable deposit with space reservation and payment of balance on or before materials closing deadline.

Cover Specifications:

Bleed size: 8 5/8" × 11 1/4" Trim: 8 3/8" × 10 7/8"

Offprints of the cover, Table of Contents page, and highlight article are available at the time of publication. These must be ordered and paid for in advance.

For front cover offprints or other quantities, contact Rae Kelley, ASPRS Assistant Director – Publications 505-819-3599 e-mail rkelley@asprs.org.

PRICING

	Corporate Member Exhibiting at a 2021 ASPRS Conference	Corporate Member	Exhibitor	Non Member
Cover 1	\$1,850	\$2,000	\$2,350	\$2,500

Belly Bands, Inserts, Outserts & More!

Make your material the first impression readers have when they get their copy of *PE&RS*. Contact Bill Spilman at bill@innovativemediasolutions.com

VENDOR SEMINARS

ASPRS Sustaining Members now have the opportunity to hold a 1-hour informational session as a Virtual Vendor Seminar that will be free to all ASPRS Members wishing to attend. There will be one opportunity per month to reach out to all ASPRS Members with a demonstration of a new product, service, or other information. ASPRS will promote the Seminar through a blast email to all members, a notice on the ASPRS web site home page, and ads in the print and digital editions of *PE&RS*.

The Virtual Seminar will be hosted by ASPRS through its Zoom capability and has the capacity to accommodate 500 attendees.

Vendor Seminars	
Fee	\$2,500 (no discounts)

EMPLOYMENT PROMOTION

When you need to fill a position right away, use this direct, right-to-desktop approach to announce your employment opportunity. The employment opportunity will be sent once to all ASPRS members in our regular Wednesday email newsletter to members, and will be posted on the ASPRS Web site for one month. This type of advertising gets results when you provide a web link with your text.

Employment Opportunity	Net Rate
30-Day Web + 1 email	\$500/opportunity
Web-only (no email)	\$300/opportunity

Do you have multiple vacancies that need to be filled? Contact us for pricing details for multiple listings.

NEWSLETTER DISPLAY ADVERTISING

Your vertical ad will show up in the right hand column of our weekly newsletter, which is sent to more than 3,000 people, including our membership and interested parties. **Open Rate: 32.9%**

Newsletter vertical banner ad	Net Rate
180 pixels x 240 pixels max	\$500/opportunity

PE&RS Digital Edition

Digital Edition E-mail Blast: 5,800+

PE&RS is available online in both a public version that is available to anyone but does not include the peer-reviewed articles, and a full version that is available to ASPRS members only upon login.

The enhanced version of *PE&RS* contains hot links for all ASPRS Sustaining Member Companies, as well as hot links on advertisements, ASPRS Who's Who, and internet references.

Become a sponsor today!

The e-mail blast sponsorship opportunity includes a **180 x 240 pixel ad** in the email announcement that goes out to our membership announcing the availability of the electronic issue.

Digital Edition Opportunities	Net Rate
E-mail Blast Sponsorship*	\$1,000

For more information, contact Bill Spilman at bill@innovativemediasolutions.com | (877) 878-3260 toll-free | (309) 483-6467 direct | (309) 483-2371 fax

PE&RS Media Kit 2021

PE&RS 2021 Advertising Rates & Specs

THE MORE YOU ADVERTISE THE MORE YOU SAVE! PE&RS offers frequency discounts. Invest in a three-times per year advertising package and receive a 5% discount, six-times per year and receive a 10% discount, 12-times per year and receive a 15% discount off the cost of the package.

	Corporate Member Exhibiting at a 2021 ASPRS Conference	Corporate Member	Exhibitor	Non Member
<i>All rates below are for four-color advertisements</i>				
Cover 1	\$1,850	\$2,000	\$2,350	\$2,500
<i>In addition to the cover image, the cover sponsor receives a half-page area to include a description of the cover (maximum 500 words). The cover sponsor also has the opportunity to write a highlight article for the journal. Highlight articles are scientific articles designed to appeal to a broad audience and are subject to editorial review before publishing. The cover sponsor fee includes 50 copies of the journal for distribution to their clients. More copies can be ordered at cost.</i>				
Cover 2	\$1,500	\$1,850	\$2,000	\$2,350
Cover 3	\$1,500	\$1,850	\$2,000	\$2,350
Cover 4	\$1,850	\$2,000	\$2,350	\$2,500
Advertorial	1 Complimentary Per Year	1 Complimentary Per Year	\$2,150	\$2,500
Full Page	\$1,000	\$1,175	\$2,000	\$2,350
2 page spread	\$1,500	\$1,800	\$3,200	\$3,600
2/3 Page	\$1,100	\$1,160	\$1,450	\$1,450
1/2 Page	\$900	\$960	\$1,200	\$1,200
1/3 Page	\$800	\$800	\$1,000	\$1,000
1/4 Page	\$600	\$600	\$750	\$750
1/6 Page	\$400	\$400	\$500	\$500
1/8 Page	\$200	\$200	\$250	\$250
Other Advertising Opportunities				
Wednesday Member Newsletter Email Blast	1 Complimentary Per Year	1 Complimentary Per Year	\$600	\$600

A 15% commission is allowed to recognized advertising agencies

Ad Size	Width	Height
Cover (bleed only)	8.625"	11.25"
Full Page (bleed)	8.625"	11.25"
Full Page (trim)	8.375"	10.875"
2/3 Page Horizontal	7.125"	6.25"
2/3 Page Vertical	4.58"	9.625"
1/2 Page Horizontal	7.125"	4.6875"
1/2 Page Vertical	3.4375"	9.625"
1/3 Page Horizontal	7.125"	3.125"
1/3 Page Vertical	2.29"	9.625"
1/4 Page Horizontal	7.125"	2.34"
1/4 Page Vertical	3.4375"	4.6875"
1/8 Page Horizontal	7.125"	1.17"
1/8 Page Vertical	1.71875"	4.6875"

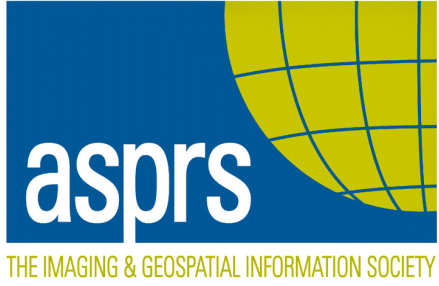
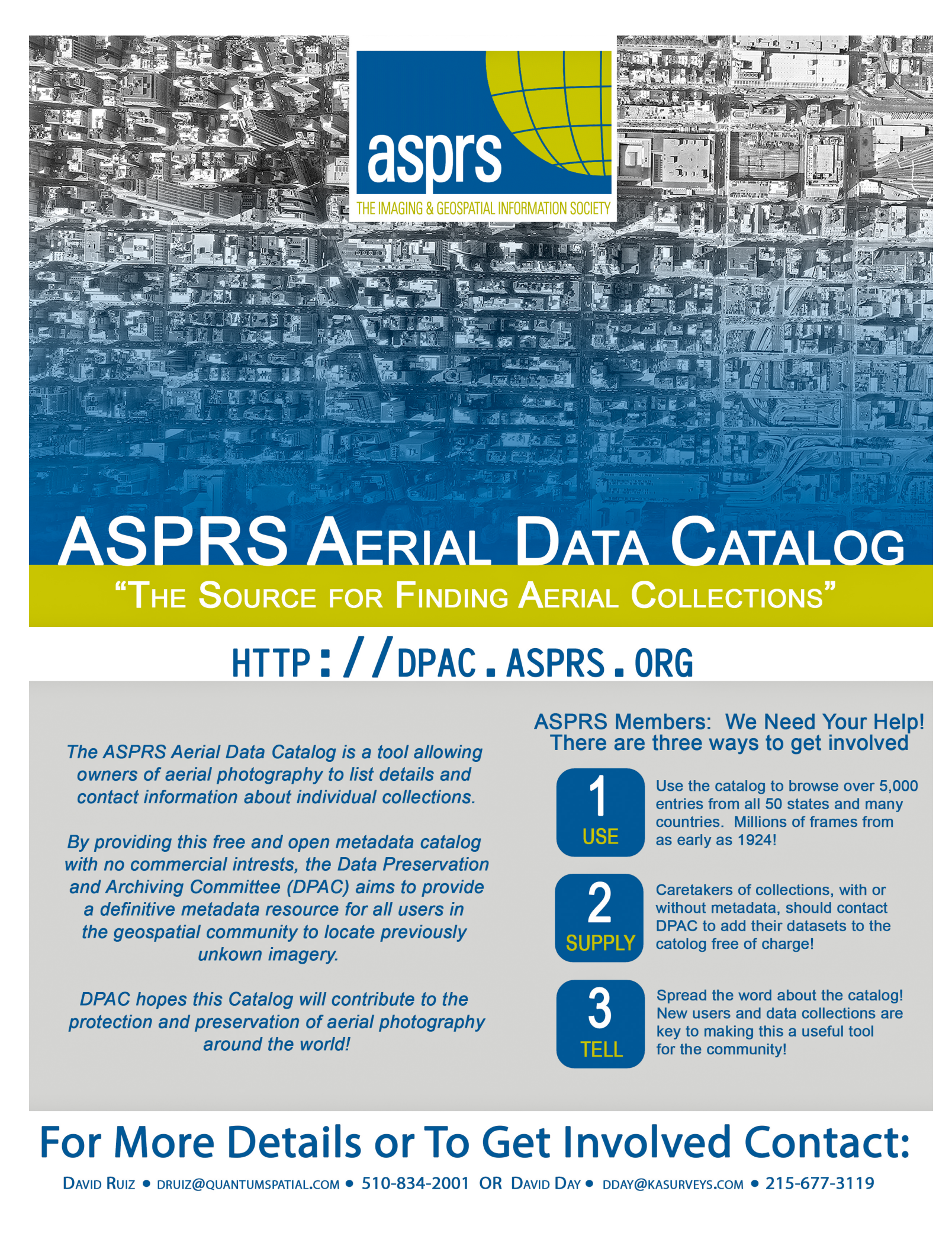
- Publication Size: 8.375" × 10.875" (W x H)
- Live area: 1/2" from gutter and 3/8" from all other edges
- No partial page bleeds.
- Publication Style: Perfect bound
- Printing Method: Web offset press
- Software Used: PC InDesign CS6
- Supported formats: TIFF, EPS, BMP, JPEG, PDF, PC InDesign, Illustrator, and Photoshop

Source: PE&RS Readership Survey, Summer 2017

For more information, contact Bill Spilman at bill@innovativemediasolutions.com | (877) 878-3260 toll-free | (309) 483-6467 direct | (309) 483-2371 fax

Send ad materials to:
 ASPRS/PE&RS Production
 425 Barlow Place, Suite 210
 Bethesda, Maryland 20814
 505-819-3599
 rkelly@asprs.org

Ship inserts to:
 Alicia Coard
 Walsworth
 2180 Maiden Lane
 St. Joseph, MI 49085
 888-563-3220 (toll free)
 269-428-1021 (direct)
 269-428-1095 (fax)
 alicia.coard@walsworth.com



asprs

THE IMAGING & GEOSPATIAL INFORMATION SOCIETY

ASPRS AERIAL DATA CATALOG

“THE SOURCE FOR FINDING AERIAL COLLECTIONS”

[HTTP://DPAC.ASPRS.ORG](http://dpac.asprs.org)

The ASPRS Aerial Data Catalog is a tool allowing owners of aerial photography to list details and contact information about individual collections.

By providing this free and open metadata catalog with no commercial interests, the Data Preservation and Archiving Committee (DPAC) aims to provide a definitive metadata resource for all users in the geospatial community to locate previously unknown imagery.

DPAC hopes this Catalog will contribute to the protection and preservation of aerial photography around the world!

ASPRS Members: We Need Your Help!
There are three ways to get involved

1

USE

Use the catalog to browse over 5,000 entries from all 50 states and many countries. Millions of frames from as early as 1924!

2

SUPPLY

Caretakers of collections, with or without metadata, should contact DPAC to add their datasets to the catalog free of charge!

3

TELL

Spread the word about the catalog! New users and data collections are key to making this a useful tool for the community!

For More Details or To Get Involved Contact:

DAVID RUIZ • DRUIZ@QUANTUMSPATIAL.COM • 510-834-2001 OR DAVID DAY • DDAY@KASURVEYS.COM • 215-677-3119

LEARN
DO
GIVE
BELONG

ASPRS Offers

- » Cutting-edge conference programs
- » Professional development workshops
- » Accredited professional certifications
- » Scholarships and awards
- » Career advancing mentoring programs
- » *PE&RS*, the scientific journal of ASPRS

asprs.org

ASPRS